UNIVERSITÀ DELLA CALABRIA

UNIVERSITÀ DELLA CALABRIA

DIPARTIMENTO DI INGEGNERIA MECCANICA, ENERGETICA E GESTIONALE

SCUOLA DI DOTTORATO PITAGORA

XXVIII CICLO

Finite Element models for the dynamic analysis of composite and sandwich structures

Settore Scientifico Disciplinare ING-IND/13 Meccanica Applicata alle Macchine

Direttore: Ch.mo Prof. Leonardo Pagnotta

Supervisori: Ch.mo Prof. Domenico Mundo

Ing. Michel Tournour, PhD

Dottoranda: Dott.sa Alessandra Treviso

Università della Calabria

Dipartimento di Ingegneria Meccanica, Energetica e Gestionale

Scuola di Dottorato Pitagora

Finite Element models for the dynamic analysis of composite and sandwich structures

PhD Candidate:
Alessandra Treviso

Supervisors:
Prof. Domenico Mundo
Dr. Michel Tournour

A thesis submitted in partial fulfilment of the requirements
for the degree of Doctor in Mechanical Engineering

November 2015

Andrà lontano? Farà fortuna?
Raddrizzerà tutte le cose storte di questo mondo?
Noi non lo sappiamo, perché egli sta ancora marciando
con il coraggio e la determinazione del primo giorno.
Possiamo solo augurargli, di tutto cuore:-Buon viaggio!

Gianni Rodari

Abstract

The use of lightweight multi-layered materials is dramatically changing the design process and criteria in many engineering fields. The transportation industry, for example, is facing major challenges in order to replace traditional materials while keeping at least the same level of passengers' comfort and safety. In particular, the *Noise, Vibration and Harshness* (NVH) performances are affected by the novel combination of high stiffness and low density. If the aeronautic industry still heavily relies on testing to assess designs' validity, such an approach cannot be applied to the automotive industry for the development costs would be too high. It is therefore necessary to identify CAE tools capable of giving realistic, reliable and cost-effective predictions of multi-layered structures' behaviour under dynamic loadings. An often overlooked problem is that of damping which is generally higher in composite and sandwich structure but rarely it is also efficiently exploited, so that in most cases the classic approach of applying NVH treatments is followed. However, this procedure has a detrimental effect on the attained weight saving and on the global dynamic performance of lightweight structures, therefore leading to unsatisfactory results. Moreover, the variability of mechanical properties due to the low repeatability of some manufacturing processes can also have an impact on the global behaviour of the as-manufactured component. An early integration of damping prediction and an estimate of possible stiffness variations due to the manufacturing can actually lead to better designs in less time.

In this thesis these challenges are tackled from the *Computer Aided Engineering* (CAE) point of view, thanks to the introduction of a novel finite element for the prediction of the damped response of generic multi-layered structures and the proposition of a CAM-CAE approach to introduce manufacturing simulations at an early stage in the design and analysis process.

In the first chapters, different analytical and numerical approaches for the modelling of multi-layered structures are presented and used for the development of a 1D finite element. The results of the mono-dimensional analysis show that *zigzag theories* are a cost-effective and accurate alternative to solid finite element models, motivating the development of a 2D element for the analysis of plates and shells. With respect to previous investigations on zigzag theories, the current study focus on their use for modal parameters prediction, i.e. eigenfrequencies, mode shapes and damping. It will be shown

that compared to classic models, the zigzag elements are able to predict the dynamic response, damped and undamped, of beam, plates and shells with the same accuracy of 3D models but at a much lower computational cost.

In the last chapter, the available homogenisation methods for the analysis of long fibres composites are reviewed and compared to more refined models based on manufacturing simulation algorithms. Results show that changes in manufacturing parameters lead to substantially different results. The goal is to show that CAM/FE coupling is possible already at an early design stage and that manufacturing simulations can be used as a mean to further optimise the performance of composite structures. As a final stage, an example of coupling between zigzag theories and manufacturing simulations is presented.

Despite some limitations, the proposed methods increase the accuracy of the analysis and gives a better understanding of lightweight multi-layered structures. Further research could focus on the use of the developed zigzag elements for fatigue analysis and delamination modelling as well as detailed modelling of drop-off regions in the framework of CAM tools improvements.

Sommario

L'utilizzo di materiali compositi sta cambiando in maniera significativa i criteri e i processi di progettazione in molti campi dell'ingegneria. Nel settore dei trasporti, ad esempio, non poche sono le problematiche connesse alla sostituzione dei materiali tradizionali, prima fra tutte la necessità di garantire almeno lo stesso livello di *comfort* e di sicurezza per i passeggeri. La combinazione di bassa densità ed elevata rigidezza modificano in particolare il comportamento dinamico delle strutture con un impatto diretto sulle prestazioni di *Noise, Vibration and Harshness* (NVH). Se da una parte l'industria aeronautica può ancora contare sulla verifica sperimentale di materiali e componenti, questo stesso approccio non può essere adottato dall'industria automobilistica, dove il contenimento dei costi e dei tempi di sviluppo è una priorità. È pertanto necessario identificare degli strumenti di simulazione in grado di predire il comportamento dinamico di strutture composite in maniera affidabile, realistica e limitando l'impiego di risorse. Un aspetto che spesso viene sottovalutato è quello dello smorzamento; nei materiali compositi, incluse le strutture sandwich, esso è generalmente piu' elevato che nei materiali tradizionali ma, allo stesso tempo, tale proprietà non viene sfruttata cosicché spesso si ricorre all' applicazione di trattamenti smorzanti tradizionali. Tuttavia, questo metodo non è privo di limitazioni: la riduzione di peso ottenuta impiegando i materiali compositi viene in parte annullata dall'aggiunta di trattamenti fono-assorbenti che, con le loro caratteristiche di massa e rigidezza, modificano il comportamento dinamico della struttura. In aggiunta, la scarsa ripetibilità di alcuni processi di produzione per i materiali compositi può influire sul comportamento della struttura reale. Integrare nella fasi iniziali della progettazione le proprietà di smorzamento, così come stimare le possibili variazioni di rigidezza dovute ai processi di produzione, si configura come una strategia progettuale in grado di incrementare la qualità dei prodotti e ridurne i costi e i tempi di sviluppo.

Le suddette problematiche costituiscono l'argomento di questa tesi in cui vengono affrontate nell'ambito del *Computer Aided Engineering* (CAE), grazie all'introduzione di un nuovo elemento finito per l'analisi della risposta smorzata di generiche strutture composite e la messa a punto di un approccio integrato CAM-CAE che si propone di introdurre le simulazioni di produzione nelle fasi iniziali della progettazione e dell'analisi.

Nei primi capitoli, i modelli analitici e numerici attualmente a disposizione vengono presentati e utilizzati per lo sviluppo di un elemento finito monodimensionale. I risultati dell'analisi 1D dimostrano che le *teorie zigzag* rappresentano una valida alternativa alla modellazione 3D, sia dal punto di vista dell'accuratezza che da quello del costo computazionale, motivando altresì lo sviluppo di un elemento bidimensionale per l'analisi di piastre e *shell*. Rispetto agli studi già presenti inletteratura, il seguente si concentra sulla capacità delle teorie zigzag di predire con accuratezza i parametri modali, ovvero le frequenze naturali, i modi di vibrare e lo smorzamento. Verrà infatti mostrato come gli elementi zigzag sono in grado di predire la risposta dinamica, libera e smorzata, di travi, piastre e shell, con un livello di accuratezza pari a quello di un modello 3D ma con una riduzione significativa dei tempi di calcolo.

Nell'ultimo capitolo, i modelli di omogenizzazione utilizzati per l'analisi di materiali compositi a fibre lunghe vengono presentati e confrontati con modelli basati sulle simulazioni dei processi di produzione. I risultati mostrano che modifiche ai processi di produzione possono modificare in maniera sostanziale le proprietà del componente. L'obiettivo è mostrare che CAM e CAE possono essere integrati nelle fasi iniziali della progettazione e che le simulazioni dei processi di produzione possono essere utilizzate per ottimizzare ulteriormente le prestazioni dei componenti in materiale composito. Infine, viene mostrata la combinazione tra l'elemento zigzag e le simulazioni di draping.

Nonostante alcune limitazioni, i metodi proposti aumentano l'accuratezza delle analisi e forniscono una migliore comprensione del comportamento delle strutture leggere, quali laminati in composito e sandwich. Ulteriori ricerche potrebbero in futuro concentrarsi sull'utilizzo dell'elemento zigzag qui proposto per le analisi a fatica, la modellazione delle delaminazioni oppure la modellazione delle regioni di transizione nell'ambito di un miglioramento degli strumenti CAM.

Acknowledgements

This PhD has been a journey, through Europe, across knowledge and through the self. Through Europe because I physically relocated from the far, peripheral Calabria to the heart of my old, beloved Continent and from there explored it, always learning a lot.
As for every PhD, the journey across knowledge has been the most exciting, sometimes frustrating experience. I started with a general idea of my goals and step by step I built what you are now reading.
Finally, it was a journey of self-discovery and improvement and I can say that all that I have read and seen, every person that I have met contributed to some extent to the success of this project. Some of them, however, require a special recognition:
- the European Commission and the GRESIMO Initial Training Network which made all of this possible in the very first place;
- Dr. Bert Van Genechten, who supported my first step into research;
- My two supervisors, Prof. Domenico Mundo and Dr. Michel Tournour, who accepted the challenge of doing something new;
- the development team in Liège for their support in developing the theories and the finite elements;
- the Virtual.Lab and Samcef customer support.

A special thought goes to my office mates, Jonathan, Karim and Simone. Working on a PhD project can be quite lonesome but we shared all the failures and the success and, beside that, we had some fun. I wish you the same fulfilling journey I had.

I believe that acknowledgements should be kept professional but I will make an exception for Donatella, Marco G., Salvatore, Stefano and Ciro, my Italian support(ers) net, scattered around but always close.

Infine, ma non per questo meno importante, un pensiero va alla mia famiglia, tutta, cui questo lavoro è dedicato. Nessuno meglio di loro conosce le grandi difficoltà e le grandi soddisfazioni sperimentate negli ultimi tre anni e può quindi comprendere cosa significhi il raggiungimento di questo traguardo: *l'inizio è là dove si arriva.*

Contents

List of Figures

List of Tables

Introduction

Structural engineering is the art of moulding materials we do not really understand into shapes we cannot really analyse, so as to withstand forces we cannot really assess, in such a way that the public does not really suspect.

E.H. Brown

The rise and challenges of multilayer structures

In the last decades, composite materials and more generally multilayer structures have massively entered the market. Applications vary from aircrafts' structural parts, to car components, from wind turbines to sport equipment (Fig. i). The reason behind this is the uncommon combination of mechanical properties that multilayer materials offer compared to traditional engineering materials.

The use of composite materials in an engineering sense started after the Second World War with the increase in polymer production. Polymers only, however, do not have the necessary mechanical properties to withstand service loads in primary structural applications, from which the necessity to reinforce them with high strength, high modulus elements arises. This can be done by introducing fibres, particles or fabrics in a polymer matrix or by including a polymer within two stiff face-sheet. We will generally refer to multilayer materials when talking about long fibres and woven fabrics composites and sandwiches. It is generally well-known that fibre reinforced polymers combine high strength and stiffness and low density; sandwich structures on the other hand give high flexural stiffness at a considerably lower weight. Weight reduction itself has become a major concern in the automotive, aerospace and energy industries. The first sectors aim at weight reduction to meet increasingly stringent regulations on pollutant emissions and lower operational costs by reducing fuel consumption; in the renewable energy industry, the design of wind turbines can reach a higher energy efficiency if lighter blades are employed.

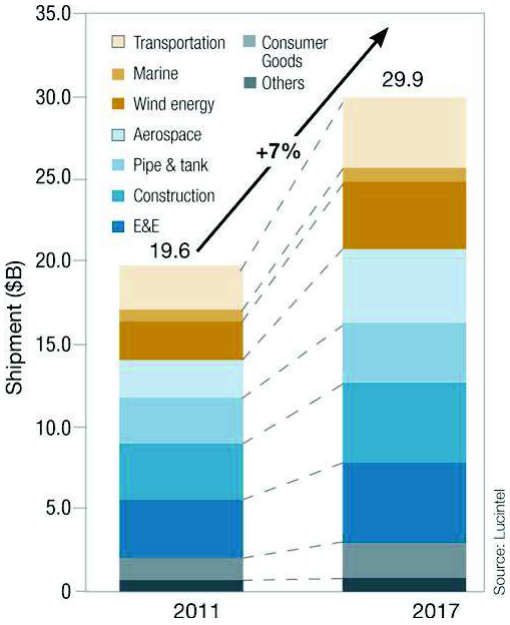

Fig. i. Composite growth forecast (Source: www.compositeworld.com)

In the first years of the new composite era, most research efforts were devoted to the understanding of basic mechanical properties of multilayer materials, development of suitable theories to predict them and proper testing methods. However, the approach was still biased by the familiarity with homogeneous materials, for the majority isotropic, for which well established relations and experimental procedures were already existing. It was soon clear that multilayer structures require a different mental and technical attitude.

First of all, the high level of tailoring that they allow just by playing with constitutive parameters, such as the type of reinforcement or orientation, makes it difficult to define simple and yet general material laws. Moreover, traditional experimental techniques proved inadequate to deal with an all new set of geometrical and mechanical properties such as the low single ply thickness and fragility in composites, the risk of inducing cracks and delaminations at sample-grips interface in both composites and sandwich or the appearance of stress-strain couplings as soon as symmetry conditions in geometry, boundary conditions and layers distribution are not met.

Many material models, strength criteria and design guidelines are now available for multilayer structures, also thanks to the extensive testing and validation work done by the aerospace and aeronautics industries, which eventually led to a set of international standards. An example of this approach is given in Fig. ii, which describes the process from coupon to full scale testing.

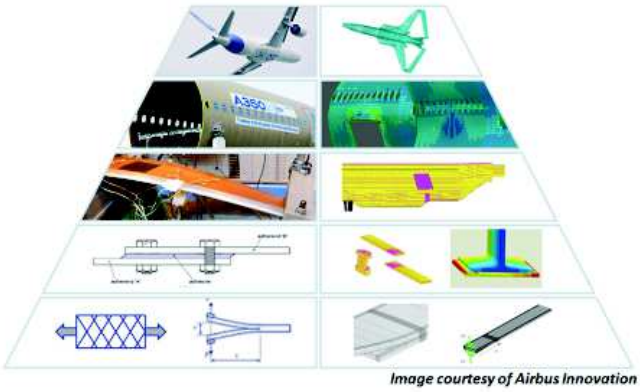

Fig. ii. Building block approach: from coupon to full scale experimental and virtual testing

The confidence gained in mechanical properties prediction allowed engineers to shift the focus to other composite-related issues in order to make their application wide-spread and therefore more cost-effective.

One of the most controversial topics about the use of composites is the so-called *black metal* approach, by which metals are just replaced by composites, generally with quasi-isotropic properties. Even though it leads to weight reduction, it is not optimal as it does not fully exploit composites' capabilities. In some applications, for example, a single type of loading acts on the structures and the use of quasi-isotropic properties is not needed, so that extra weight savings could be achieved by tailoring the anisotropy for the given application. As a matter of fact, most structures are subject to complex loading conditions and norms and design standards requirements have to be met. At the same time, such requirements are often based on metal design and safety criteria. The black metal approach also prevents from fully exploiting the forming flexibility of multi-layer structures compared to metals. The inherent characteristics of the manufacturing processes make it possible to create complex geometries with low risks of process failure; it is therefore possible to create multifunctional structures which incorporate multiple, previously metallic, components in just one, resulting in joints elimination or reduction with further weight savings and strength increase. Such major design and properties optimisation are the objectives of the *morphological optimisation*, which is a currently active research field and often goes in parallel with *bio-inspired* composites design.

On the dynamic side, the interest is arising around two main topics: fatigue and *Noise, Vibration and Harshness* (NVH). The assessment of fatigue behaviour, together with crack propagation phenomena, is crucial to ensure structures' integrity in operational conditions, to guarantee the proper functioning of machines and humans' safety, to schedule maintenance intervention in a cost-effective way.

NVH has only lately become a major concern, in particular for the automotive industry. When replacing metals with multilayer materials, not only do the engineers have to guarantee at least the same structural behaviour, but also an at least equivalent comfort level. The use of low density materials generally affects the dynamics in the sense of an increase in natural frequencies. From the point of view of noise transmission, light structures usually present worse insulation properties which would negatively impact on the acoustic comfort inside a car or a plane passengers' compartment. As for metallic structures, the easiest countermeasure is to apply on the structures layers of polymeric materials, with viscoelastic characteristics or a foamy structure that damp the vibrations that cause undesirable noise. The flaw in this procedure is that, unlike metallic parts, the weight of the treatment and the weight of the base structures are comparable; on the one hand the transmissibility is improved, but on the other the increase in mass lowers the natural frequencies. Moreover, the global stiffness of the part is degraded due to the addition of a low stiffness layer, so that the detrimental effect is twofold. Most of the outlined process is performed at a late stage in the design, when modifications and refinements imply higher costs. In order to avoid them an early integration of NVH treatments is advisable but this can only be achieved if proper modelling tools are made available to design and analysis engineers.

Other factors should also be considered when dealing with multilayer materials. For example, polymer-based composites show generally higher damping than metals, thanks to the inherent viscoelasticity of the matrix; as for stiffness and strength, stacking sequence and fibre orientation can be chosen to maximise damping. Sandwiches can be specifically built to damp vibrations by interleaving a soft viscoelastic core. In both cases, to correctly predict and optimise damping it is necessary to know not only the global but also the local behaviour in each layer. This is extensively described in the first chapters of this thesis and it constitutes the basis for the proposition of a new finite element model particularly designed for dynamic analyses.

Once designed, components need to be manufactured. The manufacturing of composites structures is a broad field and varies considerably according to the type of reinforcement, the geometry and the final application. It is during the manufacturing that the mechanical properties are eventually defined. Most of the processes for the production of particles and short fibres reinforced polymers are derived from those for neat polymers, such as the injection moulding. The introduction of a second solid phase, however, modifies the polymer flow in the mould with respect to the unreinforced counterpart and such phenomena must be accounted for to properly select process parameters such as pressure or temperature. The manufacturing of long fibres components generally requires extensive manual work, especially when big geometries are involved, which introduces a certain variability in the process. All these factors contribute to create a mismatch between the theoretical properties defined during the design stage and the actual properties of

the as-manufactured part. Recently, some *Computer Aided Manufacturing* (CAM) tools have become available to help engineers design the manufacturing processes too. Part of this work will focus on an integrated approach, which couples the manufacturing simulations to the finite element analysis to optimise both the part and the process.

Examples of multilayer structures

Composites and sandwiches can take several forms, as Fig. iii shows.

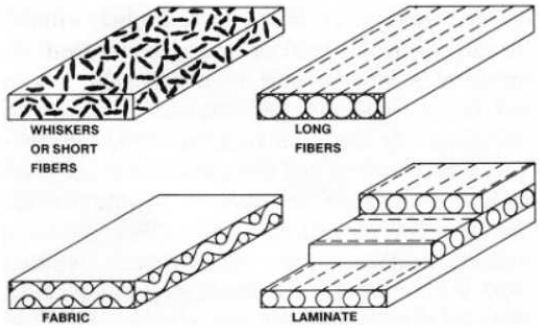

(a) *Source: http://navier.engr.colostate.edu/*

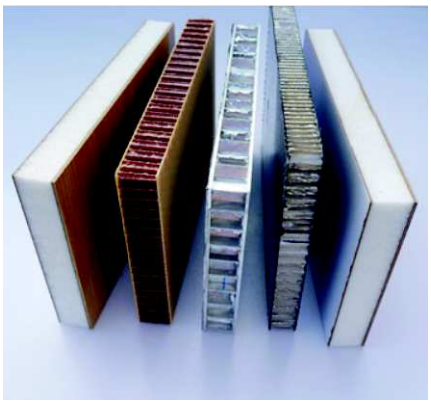

(b) From left to right: polymer foam core, three honeycomb of different materials, polymer foam core
Source: http://www.technolineconcept.fr/

Fig. iii. Different types of (A) composites and (B) sandwiches

Composite materials are the combination of two or more solid phases, the matrix and the reinforcements, that remain separate at the macroscopic level. In most applications the matrix is a polymer, a thermoset or a thermoplastic, in which particles, short fibres, long fibres or fabrics are embedded. In highly demanding applications the reinforcements are usually made of carbon or graphite, glass or Kevlar. In low tech applications, natural fibres can replace the so-called technical ones. The role of the matrix is to protect the reinforcement from external agents, transfer loads and give the general shape to the final structure. The reinforcement is on the other hand the load-carrying member. The reinforcement and the matrix are generally provided in the form of thin sheets, *laminae* or *plies*, which are then stacked up and glued together with different orientation to create the *laminate*. Short fibres deserves an extra explanation: they can be found in laminae as randomly arranged *mat* embedded in the matrix, or they can be combined with the matrix to create injection moulded parts.

Sandwiches constitute a special group of composite materials. Unlike laminate, the layers usually present significantly different properties. Their preferred application is in components undergoing bending loads. The outer layers are made up of stiff materials, either metals or laminates, which will withstand the maximum bending stresses arising in the part; the core is made of a light material, such as a polymeric foam or a honeycomb and is usually thick compared to the face sheets as to maximise the flexural stiffness with a minimum weight.
A particular class of sandwiches is that meant for vibration damping: the core is replaced by a layer of viscoelastic material which, deforming in shear, will dissipate energy under cyclic loading.

Mechanical properties of multilayer structures

Composite materials and sandwiches are heterogeneous materials and therefore their properties depend on the properties of their constituent and on the way they are combined. In Table i some matrix and reinforcement properties are shown; Table ii compares the properties of resulting composites to steel and aluminium [3]. The difference between the phases has to be kept in mind when designing a composite or a sandwich because the properties mismatch can actually lead to a decrease in strength under certain conditions.

Material	**Density** ρ **[Mg/m^3]**	**Modulus** E **[GPa]**	**Strength** σ_f **[MPa]**
Fibres			
Carbon, Type 1	1.95	390	2200
Carbon, Type 2	1.75	250	2700
Cellulose fibres	1.61	60	1200
Glass (E-glass)	2.56	76	1400-2500
Kevlar	1.45	125	2760
Matrices			
Epoxies	1.2-1.4	2.1-5.5	40-85
Polyesters	1.1-1.4	1.3-4.5	45-85

Table i. Properties of commonly used matrices and fibres

Theoretically, it is possible to create a composite out of any combination of a matrix and a reinforcement. Indeed, it is now possible to find metal and ceramic matrix composites for niche applications such as aerospace or high-temperature ones. Polymers, however,

Material	**Density** ρ **[Mg/m^3]**	**Modulus** $\boldsymbol{E}$ **[GPa]**	**Strength** σ_y **[MPa]**	$\mathbf{E}/\rho$	σ_y/ρ
Composites					
58% UD Carbon in Epoxy	1.5	189	1050	126	700
50% UD glass in Polyester	2.0	48	1240	24	620
60% UD Kevlar in Epoxy	1.4	76	1240	54	886
Metals					
High-strength Steel	7.8	207	1000	27	128
Aluminium alloy	2.8	71	500	25	179

Table ii. Properties and specific properties of common technical composites vs. metals

are still the preferred choice because of their low density, good insulation properties, easiness of manufacturing. Sandwiches alike give great flexibility in design even though their application is slightly narrower in scope. The most common configuration is that of metal outer layers with polymers or paper honeycombs but metal cores are possible as well.

Strenght and stiffness of composite materials

The constitutive parameters affecting the stiffness and strength of composites are many. The effect of their constituents mechanical properties is primarily a function of their relative volumetric fraction in the lamina. Intuitively, the higher the amount of fibres, the higher the stiffness and strength. Theoretical limits are fixed by the fibre packing scheme, which can be either square or triangular (Fig. iv) leading to a maximum value of volume fraction of 0.785 and 0.907 respectively. In practice, the volume fraction of fibres is between 0.5 and 0.8 for long fibres and lower for short fibres because of practical manufacturing limitations [4].

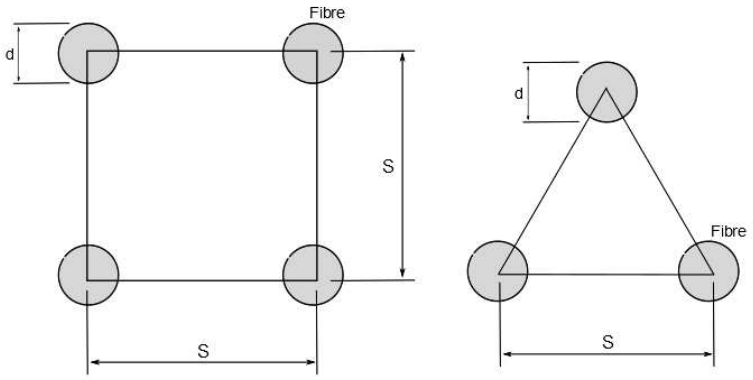

Fig. iv. Square fibre-packing (left) and triangular fibre-packing (right)

Beside the previously mentioned functionalities, the matrix also compensates for the lack of lateral resistance of long fibres. Most of the *micromechanics*, extensively surveyed in [5–8], is based on volume fractions. This information can be used to calculate the moduli of the basic lamina according to the *rule of mixtures* [9], which predicts that the moduli are the sum of the matrix and fibres moduli weighted by their volume fractions. As an example, the variation of the longitudinal modulus with respect to the fibres volume fraction is given in Fig. v.

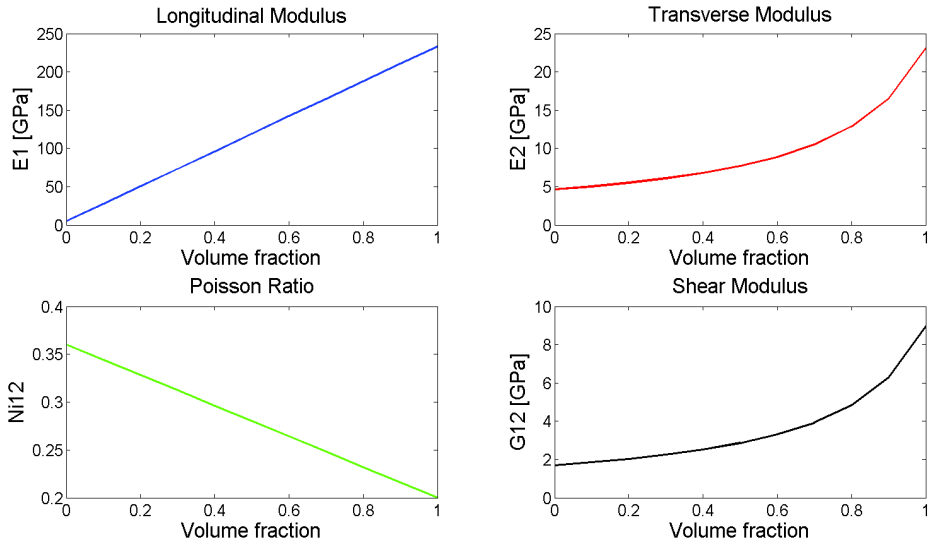

Fig. v. Variation of the in-plane stiffness coefficients with fibres volume fraction

While the rule of mixtures gives quite accurate results for design purposes for the longitudinal modulus and the Poisson's ratio, comparison with experimental results showed discrepancies for the transverse and the shear modulus, for which improved models have been proposed [10–12]. These models introduce geometric factors, which are believed responsible for the theoretical-experimental mismatch.

Analysis at lamina and laminate level is often referred to as *macromechanics*. At this scale the most important parameter is the orientation of fibres and its sequence in the stack up, for it will determine the plies reaction to applied loads and the laminate elastic behaviour. When short fibres are randomly dispersed in the matrix the resulting properties will be quasi-isotropic, since there will be fibres oriented at every angle, thus providing strength in every direction. However, a closer look at short fibres injection moulded parts reveals a stratification of preferred orientations, which is induced by the phenomenon of fountain flow [13].

In long fibres composites, the strength is predominantly tensile and along the fibres direction. Depending on the nature of the matrix and of the reinforcement, the lamina can behave as isotropic (random fibres or particles), orthotropic - general, special or transverse orthotropy- or anisotropic (unidirectional fibres and fabrics). The single lamina

properties are defined in the material coordinate system $(1, 2, 3)$, 1 being the direction defined by the fibres, 2 the direction perpendicular to the fibres in the lamina plane and 3 obtained by the right-hand rule. The angle between direction 1 and the global x axis is the lamination angle (θ), counter-clockwise positive (Fig. vi).

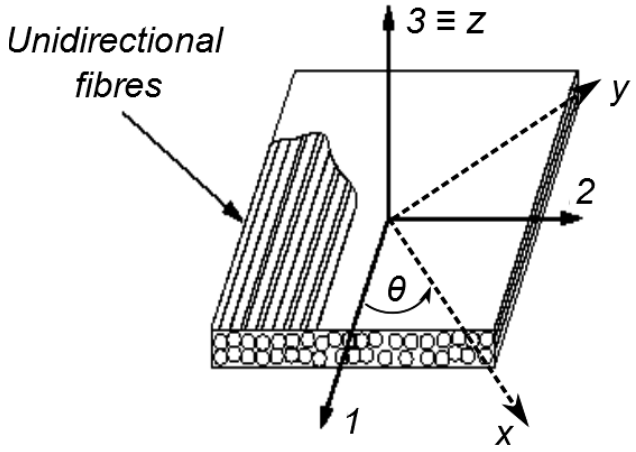

Fig. vi. Lamina and global axis systems

When θ varies a corresponding variation takes place in the lamina moduli evaluated in the global coordinate system. Fig. vii gives an example of such dependency.

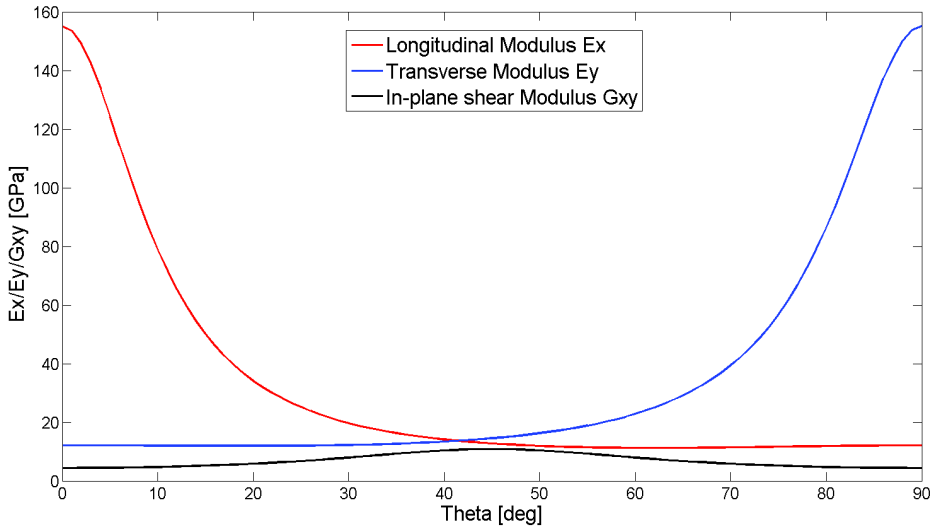

Fig. vii. Variation of in-plane coefficients at varying lamination angle

Unless a specific level of anisotropy is required by the application, plies oriented at different angles are normally present in a laminate to provide stiffness and strength in all the global directions. Due to manufacturing limitations, the most common angles are 0, 30, 45 and 90 degrees. Depending on the sequence chosen for the laminate, the global mechanical behaviour will be different, making the lamination sequence a decisive

factor in the design. The most common approach would be to set stiffness and strength requirements and then generate through an optimisation algorithm [14] a set of possible layups, the resistance of which will be tested against one of the failure criteria. The isotropic, orthotropic or anisotropic behaviour of the laminate is also determined by the sequence of lamination angles. A thorough discussion on the stiffness matrix of laminates will be carried out in Chapter 1; for now we will limit our considerations to practical observations. As mentioned in the beginning, symmetry conditions play an important role in composite structures' behaviour, independently of the laminae nature. The first symmetry to consider is that of the lamination sequence (Fig. viii), which will avoid the occurrence of coupling phenomena like bending-twisting and bending-stretching coupling.

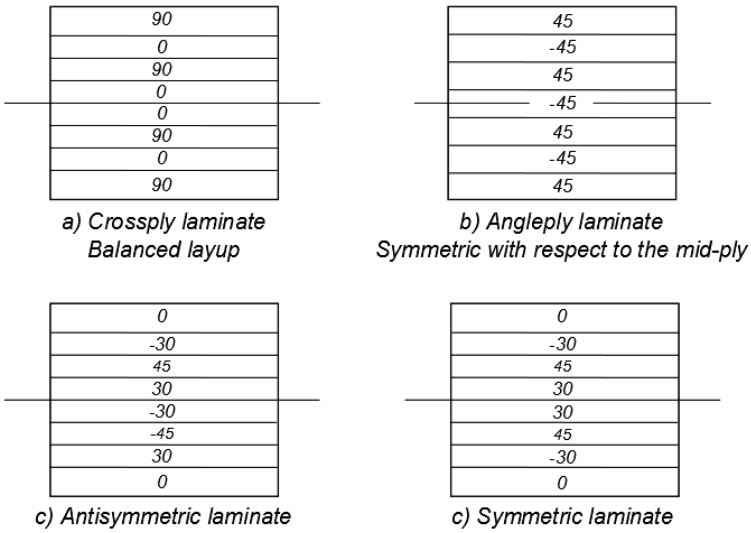

Fig. viii. Examples of laminates

Quasi-isotropic behaviour can be obtained when the relative angle between adjacent layers is kept constant. Angle-ply laminates have all the plies oriented at $\pm\theta$, while a cross-ply will have only 0 and 90 degrees laminae. When symmetry of layup is observed, the laminate will in general behave as orthotropic. A special case is that of the balanced laminate in which there is an equal number of 0 and 90 degrees plies.

Strength and stiffness of sandwich structures

The facesheets of sandwiches are made of stiff materials such as metals or composite laminates. Cores on the other hand can be of several materials, depending on the application. Foams and honeycombs are widely used alternatives. Table iii and Fig. ix

highlight properties and structures of some sample core materials.

Honeycombs	ρ **[g/cm^3]**	G_L **[MPa]**	G_W **[MPa]**	S_L **[MPa]**	S_W **[MPa]**
Paper	0.056	141	38	1.3	0.48
Aluminium	0.070	460	200	2.2	1.50
Nomex	0.080	69	44	2.2	1.00
Nomex	0.129	112	64	3.2	1.70
Foams	ρ **[g/cm^3]**		G **[MPa]**		S **[MPa]**
Polyurethane	0.04		4		0.25
PVC H100	0.10		40		1.40
PVC HD130	0.13		40		1.50
PMI 110IG	0.11		50		2.40

ρ= density; G= shear modulus; S= strength; L= longitudinal direction; W= width direction.

Table iii. Properties of Honyecombs and Foams [2]

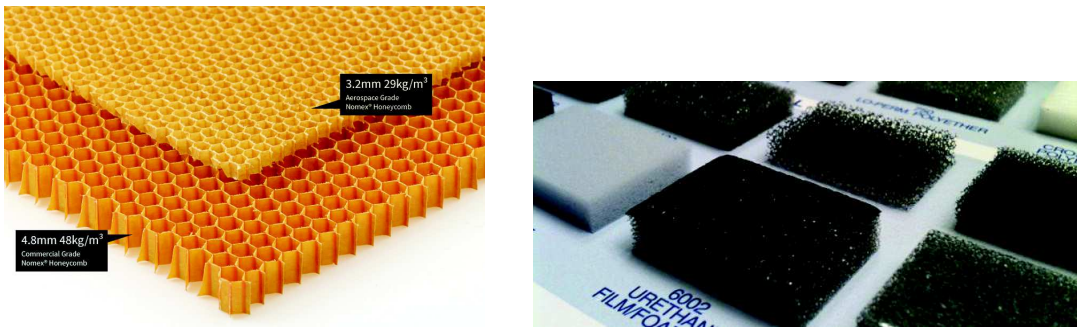

(a) Nomex™Honeycomb
Source: http://www.easycomposites.co.uk/

(b) Polymer Foams
Source:http://www.americanflexible.com/

Fig. ix. Sample cores

Polymers can be foamed easily by blowing compressed gas in the molten polymer or by chemical reactions. The advantage of foams over the solid material is their lower mass density. The *relative density*, that is the ratio between the density of the foam and the density of the bulk polymer, plays the same role of fibres volume fractions in composites [3] and is used to calculate all the mechanical properties. Being polymeric, they generally have a low modulus, but thanks to the cellular structure they can undergo large deformation before the collapse of the cells' walls, thus absorbing a lot of energy. One of the drawbacks is the low repeatability in the structure and therefore in material properties [15], introducing uncertainties on the properties of the entire sandwich.
Honeycombs, as the name itself suggests, are characterised by a periodic hexagonal structure similar to that of a beehive. Honeycomb can be metallic [16] but the most

employed material is Nomex™, which is a paper reinforced by aramid fibres [17]; glass and carbon fibres reinforced papers are available as well. Especially when using paper honeycomb, the bending stiffness and strength of the sandwich can be increased by tuning the thickness of the core at almost no significant mass addition [18]. As foams, thanks to the cellular structure honeycombs are able to absorb a lot of energy before collapsing.

Viscoelastic polymers are mainly added for vibration damping purposes. The investigation will be limited to this type of sandwich even though the proposed model can be adjusted to account for other type of core properties. Viscoelastic materials show properties that depend on both time and temperature [19]. When subject to external loads, a viscoelastic material will exhibit a twofold response: elastic deformation, that is instantaneous and fully recoverable; viscous flow, that takes place over time and is irreversible. Such a property makes them appealing for energy dissipation applications. The phase ϕ between load and response is a measure of the dissipative capabilities of the material (Fig. x). A more detailed description of the dissipative behaviour of viscoelastic materials will be given later on in this thesis.

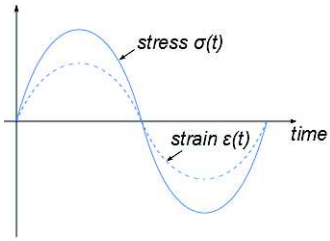

(a) Elastic behaviour, ϕ=0

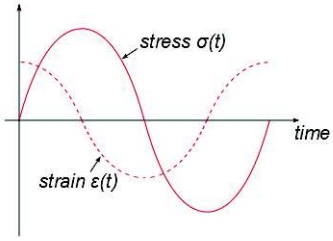

(b) Viscous behaviour, ϕ=$\pi/2$

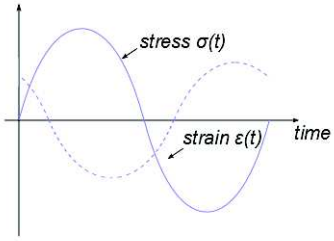

(c) Viscous behaviour, $0 < \phi < \pi/2$

Fig. x. Contributions to the viscoelastic material response

Thesis outline and objectives

This thesis is divided in five chapters. The first four chapters investigate the currently available strategies for the modelling of multi-layered structures. When thick structures

are modelled using traditional theories, the level of inaccuracy of the results can actually make them unacceptable for design analysis and validation. At the same time, simulations are acquiring more and more importance in the industrial practice because of the time and money savings that they can bring compared to prototype testing. For composite and sandwiches this is especially true due to the multiple material configurations that are available to the designers. Therefore, in the first chapter the traditional models are first reviewed to identify their limitations with respect to the problem of vibration in lightweight structures. Among the refined theories proposed, the *Zigzag Theories* are further investigated and used for the development of a 1D finite element, since they represent a more economic yet accurate way as compared to other theories or 3D models. Two Zigzag Theories are initially selected and compared under static loads. The *Refined Zigzag Theory* proved to perform better and its application is extended to the dynamic domain. Being the NVH performance of light structures the main concern of this investigation, damping modelling is also addressed and then integrated in the developed finite element models. The 1D case is further extended to the bi-dimensional case to evaluate to capabilities of the Zigzag Theories in predicting the vibration of plates and shells.

The last chapter of the thesis deals with the manufacturing simulations long fibres composites. Standard FEM codes use basic homogenisation method to convert heterogeneous, anisotropic materials to equivalent isotropic ones. This procedure may not give accurate results when complex geometries are involved, since the manufacturing process will introduce some modifications to the ideal distribution of the reinforcement with an impact on the mechanical properties. As a matter of fact, the manufacturing simulations can be used to predict the properties of the as-manufactured part but also as an optimisation tool to tailor the properties. An integrated CAM/CAE process is thus proposed and used to show how a difference in the chosen homogenisation method can lead to substantially different results. In particular, the prediction of natural frequencies and mode shapes is taken into account. Finally, the same method is combined to the newly proposed 2D element.

Chapter 1

Analytical formulations for multilayer structures

1.1 Lamina Constitutive Equations

Before presenting the models used to analyse composite and sandwich structures, it is worth to review the constitutive equations of the lamina which constitutes the laminate basic building block. Two assumptions are made to derive the constitutive equations of a lamina [4, 20, 21]

1. the lamina is a continuum;
2. the lamina behaviour is linear elastic.

The first hypothesis implies that the macromechanical behaviour only is considered. The second hypothesis ensures the validity of the Hooke's law, which in contracted form reads:

$$\sigma_i = C_{ij}\epsilon_j \tag{1.1}$$

where

$$C_{ij} = \begin{bmatrix} C_{11} & C_{12} & C_{13} & C_{14} & C_{15} & C_{16} \\ & C_{22} & C_{23} & C_{24} & C_{25} & C_{26} \\ & & C_{33} & C_{34} & C_{35} & C_{36} \\ & Sym. & & C_{44} & C_{45} & C_{46} \\ & & & & C_{55} & C_{56} \\ & & & & & C_{66} \end{bmatrix} \tag{1.2}$$

From the mechanics of materials it is known that the elastic tensor C_{ij} is symmetric.

In the most general case (anisotropic material), the tensor will contain 21 independent elastic constants; more often materials present planes of symmetry, which reduce the number of independent elastic coefficients to determine:

Monoclinic material

A material with one plane of symmetry is monoclinic and it only requires 13 independent constants.

$$C_{ij}^{M} = \begin{bmatrix} C_{11} & C_{12} & C_{13} & 0 & 0 & C_{16} \\ & C_{22} & C_{23} & 0 & 0 & C_{26} \\ & & C_{33} & 0 & 0 & C_{36} \\ & Sym. & & C_{44} & C_{45} & 0 \\ & & & & C_{55} & 0 \\ & & & & & C_{66} \end{bmatrix} \tag{1.3}$$

Orthotropic material

Most laminae are orthotropic, that is they have three planes of material symmetry that are mutually perpendicular. In such a case the number of independent constants is 9.

$$C_{ij}^{O} = \begin{bmatrix} C_{11} & C_{12} & C_{13} & 0 & 0 & 0 \\ & C_{22} & C_{23} & 0 & 0 & 0 \\ & & C_{33} & 0 & 0 & 0 \\ & Sym. & & C_{44} & 0 & 0 \\ & & & & C_{55} & 0 \\ & & & & & C_{66} \end{bmatrix} \tag{1.4}$$

A particular case it that of the *Specially orthotropic* lamina, which exhibits isotropy in the plane transverse to the fibres direction. This is due to the statistically random arrangement of the fibres within the lamina. In this case the number of elastic constants is further reduced from 9 to 5.

$$C_{ij}^{SO} = \begin{bmatrix} C_{11} & C_{12} & C_{12} & 0 & 0 & 0 \\ & C_{22} & C_{23} & 0 & 0 & 0 \\ & & C_{22} & 0 & 0 & 0 \\ & Sym. & & (C_{22}-C_{23})/2 & 0 & 0 \\ & & & & C_{66} & 0 \\ & & & & & C_{66} \end{bmatrix} \tag{1.5}$$

For sandwiches, in the majority of cases, isotropic properties are involved even though they differ from layer to layer. Elastic constants can be expressed in terms of the engineering constants as these can be easily retrieved from material testing. The orthotropic

strain-stress relationship then reads:

$$\begin{Bmatrix} \varepsilon_1 \\ \varepsilon_2 \\ \varepsilon_3 \\ \gamma_{23} \\ \gamma_{31} \\ \gamma_{12} \end{Bmatrix} = \begin{bmatrix} 1/E_1 & -\nu_{21}/E_2 & -\nu_{31}/E_3 & 0 & 0 & 0 \\ & 1/E_2 & -\nu_{32}/E_3 & 0 & 0 & 0 \\ & & 1/E_3 & 0 & 0 & 0 \\ & Sym. & & 1/G_{23} & 0 & 0 \\ & & & & 1/G_{31} & 0 \\ & & & & & 1/G_{12} \end{bmatrix} \begin{Bmatrix} \sigma_1 \\ \sigma_2 \\ \sigma_3 \\ \tau_{23} \\ \tau_{31} \\ \tau_{12} \end{Bmatrix} \tag{1.6}$$

The above stiffness matrices are valid in the local lamina frame $\{1, 2, 3\}$ (l). When laminates are built, laminae are oriented at different angles and stress-strain relationship are sought in the global laminate frame $\{x, y, z\}$ (g). It is therefore necessary to operate a coordinate transformation by means of proper transformation matrices $[T]$. It is sufficient to write the static equilibrium for a differential lamina element, wedge shaped, to obtain the following relation, where c= $\cos\theta$ and s= $\sin\theta$:

$$\begin{Bmatrix} \sigma_x \\ \sigma_y \\ \sigma_z \\ \sigma_{yz} \\ \sigma_{xz} \\ \sigma_{xy} \end{Bmatrix} = \begin{bmatrix} c^2 & s^2 & 0 & 0 & 0 & -2sc \\ s^2 & c^2 & 0 & 0 & 0 & 2sc \\ 0 & 0 & 1 & 0 & 0 & 0 \\ 0 & 0 & 0 & c & -s & 0 \\ 0 & 0 & 0 & s & c & 0 \\ sc & -sc & 0 & 0 & 0 & c^2 - s^2 \end{bmatrix} \begin{Bmatrix} \sigma_1 \\ \sigma_2 \\ \sigma_3 \\ \tau_{23} \\ \tau_{13} \\ \tau_{12} \end{Bmatrix} \tag{1.7}$$

Equally, strains can be transformed from the local to the global axis according to:

$$\begin{Bmatrix} \varepsilon_x \\ \varepsilon_y \\ \varepsilon_z \\ \gamma_{yz} \\ \gamma_{xz} \\ \gamma_{xy} \end{Bmatrix} = \begin{bmatrix} c^2 & s^2 & 0 & 0 & 0 & -sc \\ s^2 & c^2 & 0 & 0 & 0 & sc \\ 0 & 0 & 1 & 0 & 0 & 0 \\ 0 & 0 & 0 & c & s & 0 \\ 0 & 0 & 0 & -s & c & 0 \\ 2sc & -2sc & 0 & 0 & 0 & c^2 - s^2 \end{bmatrix} \begin{Bmatrix} \varepsilon_1 \\ \varepsilon_2 \\ \varepsilon_3 \\ \gamma_{23} \\ \gamma_{13} \\ \gamma_{12} \end{Bmatrix} \tag{1.8}$$

Finally, the transformation matrix for the elastic tensor can be derived by mere application of the Hooke's law, as Eq. 1.9 shows.

$$\{\sigma\}_g = [T]\{\sigma\}_l = [T][C]_l\{\varepsilon\}_l = [T][C]_l[T]^T\{\varepsilon\}_g = [C]_g\{\varepsilon\}_g \tag{1.9}$$

The transformed stiffness matrix $[C]_g = [T][C]_l[T]^T$ is fundamental to build the laminate stiffness matrix, which will be discussed in the next section.

1.2 Equivalent Single Layer Theories

Laminate and sandwiches are made up of several layers of materials which show different mechanical properties. The most challenging aspect of composite modelling is handling the heterogeneity of properties, not only within the single lamina, but also at macroscopic laminate level, that is the variation of properties through the thickness. Speaking from the finite element modelling point of view, several strategies are available but a trade-off between accuracy and computational efficiency has to be found. Three-dimensional modelling, despite being the most accurate way of representing a multilayer structure, is usually expensive and therefore avoided. However, it is still sometimes used for sandwiches to accurately catch the behaviour of the core. In all other cases, other simplified approaches are used. It is possible to distinguish between *Equivalent Single Layer Theories* (ESLT) and three-dimensional elasticity theories, which include the *Layer-wise Theories* (LWT) and 3D elasticity formulations.
ESLT approximate the behaviour of a multilayer heterogeneous material to that of an equivalent single layer homogeneous material. To do so, it is common practice to start from a kinematic model describing the displacement field in the laminate or sandwich and then build the so-called *pseudo-constituive laminate equation* [4], which relates stresses and strains through the equivalent stiffness matrix of the laminate.

1.2.1 Classical Lamination Theory

The *Classical Lamination Theory* (CLT) is historically the first proposed approach, as works from the 1950s and 1960s witness [22,23]. The CLT stems from the Euler-Bernoulli theory for beams and from the *Classical Plate Theory* (CPT) for plates [24]. In order to use the same deformation hypothesis, the following assumptions are made on the behaviour of the laminate:

1. laminae are perfectly bonded together, so that they behave as unitary;
2. no interfacial slip occurs;
3. interfacial bonds do not deform in shear.

Fig. 1.1 shows the axis system used to derive the relevant equations.

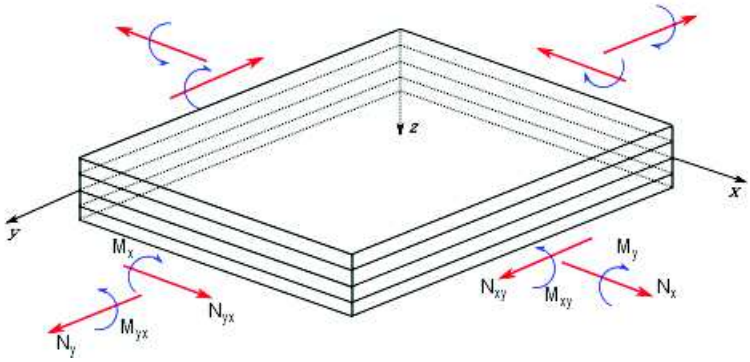

Fig. 1.1. Axis system and stress resultants acting on a laminated plate

The following theoretical assumptions are made:

1. the laminate is made of linear elastic orthotropic laminae, perfectly bonded together, whose principal material axes are oriented at arbitrary angles with respect to the x, y axes;
2. the thickness t of the plate is much smaller than the in-plane dimensions, a and b;
3. small displacement hypothesis is assumed;
4. in-plane strains $\{\varepsilon_x, \varepsilon_y, \gamma_{xy}\}$ are smaller than 1;
5. transverse strains $\{\varepsilon_z, \gamma_{xz}, \gamma_{yz}\}$ can be neglected (plane-stress hypothesis);
6. the in-plane displacements, u, v, are linear functions of the thickness coordinate z;
7. transverse shear stresses vanish at the outer free surfaces.

Hypotheses 5 and 6 together correspond to Kirchhoff hypothesis that lines normal to the mid-surface remain straight and normal after the deformation. The displacement field can finally be expressed as:

$$\begin{aligned} u(x,y,z) &= u_0(x,y) + z\frac{\partial w}{\partial x} \\ v(x,y,z) &= v_0(x,y) + z\frac{\partial w}{\partial y} \\ w(x,y,z) &= w_0(x,y) \end{aligned} \tag{1.10}$$

In Eq. 1.10 u_0 and v_0 are the displacements on the mid-plane of the laminate along x and y respectively; the transverse displacement w is constant over the thickness as inextensibility of normals holds thanks to Kirchhoff hypothesis. The consistent strains

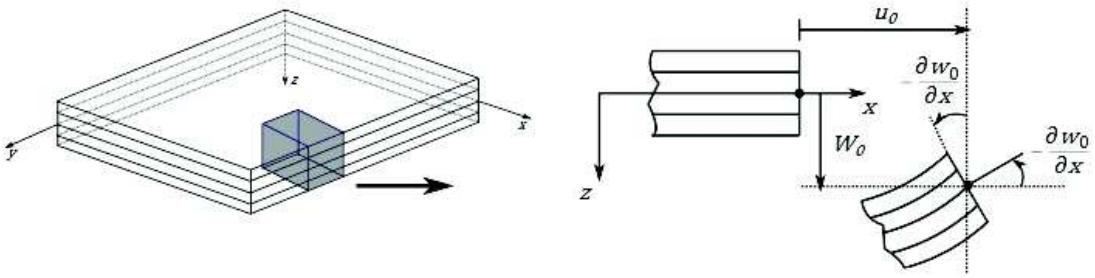

Fig. 1.2. Deformation of the plate according to the CLT

are given by Eq. 1.11 :

$$\begin{aligned}\varepsilon_x &= \frac{\partial u}{\partial x} = \varepsilon_x^0 + z\kappa_x \\ \varepsilon_y &= \frac{\partial v}{\partial y} = \varepsilon_y^0 + z\kappa_y \\ \gamma_{xy} &= \frac{\partial u}{\partial y} + \frac{\partial v}{\partial x} = \gamma_{xy}^0 + z\kappa_{xy}\end{aligned} \tag{1.11}$$

where

$$\varepsilon_x^0 = \frac{\partial u^0}{\partial x} \qquad \varepsilon_y^0 = \frac{\partial v^0}{\partial y} \qquad \gamma_{xy}^0 = \frac{\partial u^0}{\partial y} + \frac{\partial v^0}{\partial x} \tag{1.12}$$

are the strains on the mid-plane and

$$\kappa_x = -\frac{\partial^2 w}{\partial x^2} \qquad \kappa_y = -\frac{\partial^2 w}{\partial y^2} \qquad \kappa_{xy} = -2\frac{\partial^2 w}{\partial x \partial y} \tag{1.13}$$

are the curvature of the mid-surface. The stress-strain equation for the $k-th$ lamina takes the form:

$$\begin{Bmatrix}\sigma_x \\ \sigma_y \\ \tau_{xy}\end{Bmatrix}_k = [\bar{C}]_k \begin{Bmatrix}\varepsilon_x^0 + z\kappa_x \\ \varepsilon_y^0 + z\kappa_y \\ \gamma_{xy}^0 + z\kappa_{xy}\end{Bmatrix} \tag{1.14}$$

The laminate constitutive equation can finally be obtained by substitution of Eq. 1.14 in the stress resultants expressions:

$$\begin{aligned}N_x &= \sum_{k=1}^{N} \int_{z_{k-1}}^{z_k} \{(\bar{C_{11}})_k \varepsilon_x + (\bar{C_{12}})_k \varepsilon_y + (\bar{C_{16}})_k \gamma_{xy}\} \\ M_x &= \sum_{k=1}^{N} \int_{z_{k-1}}^{z_k} \{(\bar{C_{11}})_k \varepsilon_x + (\bar{C_{12}})_k \varepsilon_y + (\bar{C_{16}})_k \gamma_{xy}\} z dz\end{aligned} \tag{1.15}$$

We can finally define the laminate extensional, bending and coupling stiffnesses as:

$$\textit{Extensional Stiffness: } A_{ij} = \int_{-t/2}^{t/2} (\bar{C_{ij}})_k dz \quad = \sum_{k=1}^{N} (\bar{C_{ij}})_k (z_k - z_{k-1}) \tag{1.16}$$

$$\textit{Coupling Stiffness:} \qquad B_{ij} = \int_{-t/2}^{t/2} (\bar{C_{ij}})_k z dz \ = \frac{1}{2}\sum_{k=1}^{N} (\bar{C_{ij}})_k (z_k^2 - z_{k-1}^2) \tag{1.17}$$

$$\textit{Bending Stiffness:} \qquad D_{ij} = \int_{-t/2}^{t/2} (\bar{C_{ij}})_k z^2 dz = \frac{1}{3}\sum_{k=1}^{N} (\bar{C_{ij}})_k (z_k^3 - z_{k-1}^3) \tag{1.18}$$

It is interesting to notice that integration over the laminate thickness becomes a discrete summation over the number of layers N. The $[B]$ matrix will in general be zero for those lamination schemes that avoid couplings. This procedure allows one to derive the laminate stiffness matrices independently from the starting displacement field. In the remainder of this thesis only the kinematic models will be shown and the stiffness matrices explicitly written only if relevant to the ongoing discussion.
The CLT is still the reference model when dealing with laminates. However, its accuracy starts to decrease rapidly as the thickness of the structures increases, since the transverse shearing can no longer be neglected. In addition to that, the main limitation of the CLT is the linear variation of in-plane displacements in the through-the-thickness direction which leads to a constant distribution of transverse shear strains and constant transverse shear stresses. The latter are discontinuous at layers' interface (Fig. 1.3).

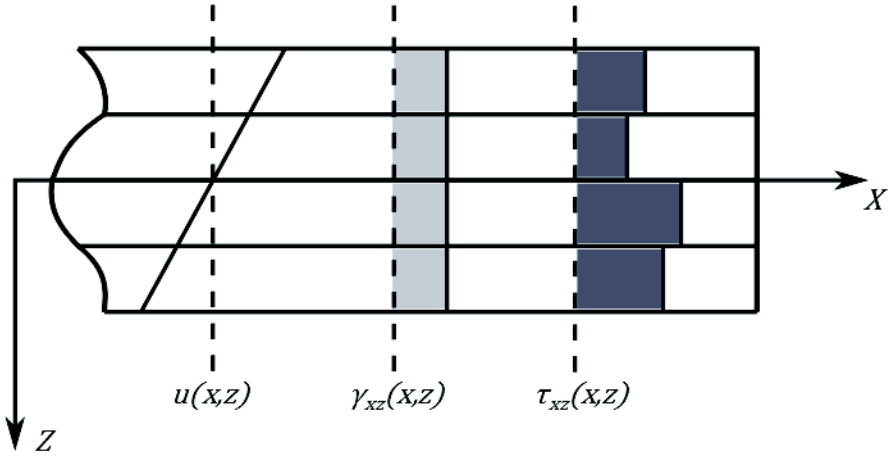

Fig. 1.3. Distribution of transverse shear strains and stresses according to the CLT

To overcome the outlined shortcomings, several refinements to the CLT have been proposed over the years, mainly to better capture the physics of the problem. Most of these refinements consist in expanding the axial displacement in power series of the thickness coordinate and additional unknowns [25].

1.2.2 First Order Shear Deformation Theory

The *First Order Shear Deformation Theory* (FSDT) is based on the Timoshenko theory [26] for beams and on the Mindlin theory for plates [27], which drop the assumption that lines normal to the mid-plane before the deformation remain straight and normal to the mid-plane after the deformation; this in turns means that the cross-section is allowed to rotate independently of the transverse deflection. From the physical point of view, this hypothesis relaxation allows us to take into account the transverse shear strains in beams and plates. Shearing can significantly contribute to the deformation in homogeneous thick structures; in composites and sandwiches transverse shear stresses and strains are always present because of the stiffness mismatch that occurs at interfaces. From the mathematical point view the corresponding kinematic model reads:

$$\begin{aligned} u(x,y,z) &= u_0(x,y) + z\theta_x(x,y) \\ v(x,y,z) &= v_0(x,y) + z\theta_y(x,y) \\ w(x,y,z) &= w_0(x,y) \end{aligned} \tag{1.19}$$

where θ_x and θ_y are the cross section rotations around the y and x axis respectively. The rotation θ in this case consists of two contributions (Fig. 1.4): the rotation due to the mere deflection of the plate and the additional contribution of shearing so that

$$\theta_x = \gamma_{xz} + \frac{\partial w_0}{\partial x} \qquad \theta_y = \gamma_{yz} + \frac{\partial w_0}{\partial y}. \tag{1.20}$$

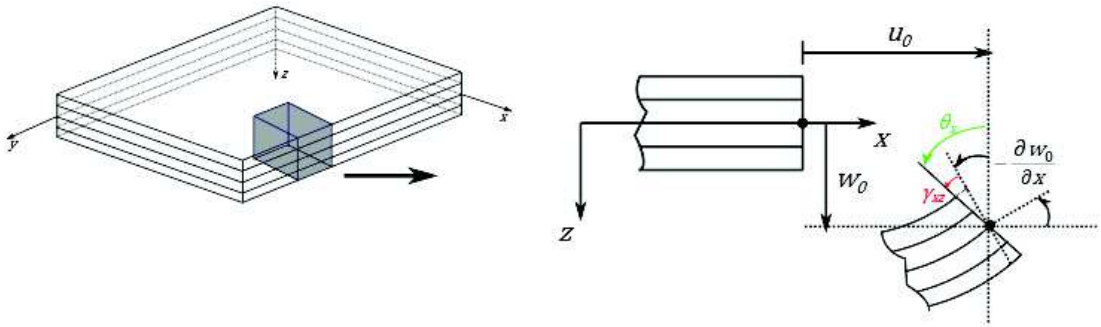

Fig. 1.4. Deformation of the plate according to the FSDT

The procedure followed in the preceding paragraph to derive the stiffness matrices can be followed in this case too. Despite the added flexibility to the beam or plate model, the strain and stress distribution resulting from the FSDT is the same as that shown in Fig. 1.3. As a matter of fact, the elasticity theory predicts a parabolic distribution of the transverse shear stresses over the cross-section for homogeneous structures [28]; for composites and sandwiches the distribution is parabolic at least over the layer's thickness (Fig. 1.5). Timoshenko proposed the introduction of a *shear correction factor* (SCF).

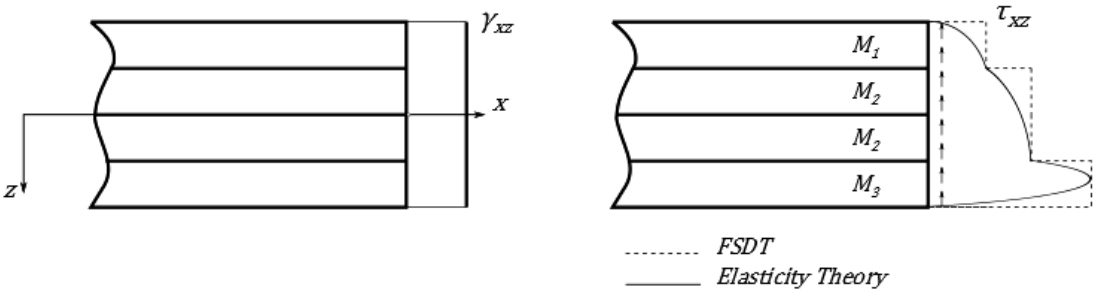

Fig. 1.5. Distribution of transverse shear stresses over a laminate section

The SCF is such that the FSDT transverse shear distribution is energetically equivalent to that predicted by the elasticity theory.

1.2.3 Higher Order Shear Deformation Theory

Higher Orde Shear Deformation Theories (HSDT) further relax the Kirchhoff hypotheses so that the cross-section does not need to remain plane and normal to the mid-plane but can warp under the effects of the external loadings (Fig. 1.6).

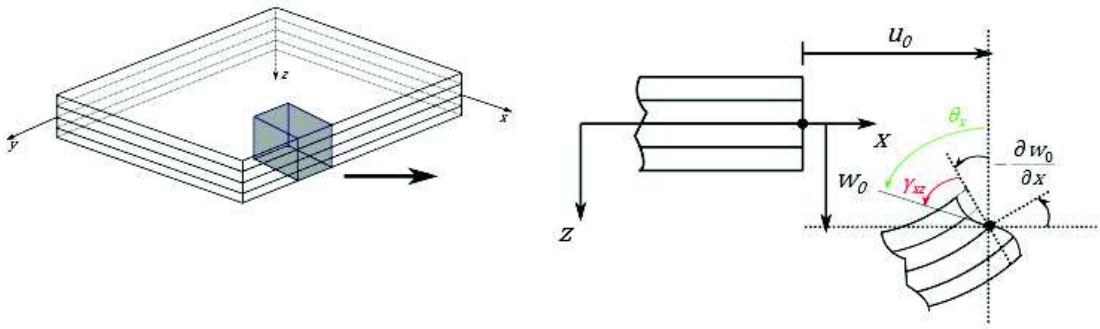

Fig. 1.6. Deformation according to the HSDT

The expansion of the displacements in terms of the thickness coordinate can be of any order and type [29–34]. A general mathematical formulation for the HSDT is given below:

$$\begin{aligned} u(x,y,z) &= u_0(x,y) + z\theta_x + z^2 f_1^x(x,y) + z^3 f_2^x(x,y) + ... + z^n f_{n-1}^x(x,y) \\ v(x,y,z) &= v_0(x,y) + z\theta_y + z^2 f_1^y(x,y) + z^3 f_2^y(x,y) + ... + z^n f_{n-1}^y(x,y) \\ w(x,y,z) &= w_0(x,y) \end{aligned} \tag{1.21}$$

where f_i^x and f_i^y with $i = 1, ..., n-1$ are the model unknowns associated with the higher order thickness coordinate terms. However, because of practical limitations, such as the

high number of unknowns, the implementation difficulties which lead to a marginal gain only, most authors limited the expansion to order 3 [35–41]. Among the third-order theories (TSDT), the one proposed by Reddy [42] is probably the most famous one and the one that underwent many finite element implementations both for beams and plates. The Reddy third-order theory has the form shown in Eq.1.22

$$\begin{aligned} u(x,y,z) &= u_0(x,y) + z\theta_x(x,y) + z^3\left(-\frac{4}{3h^2}\right)\left(\theta_x(x,y) + \frac{\partial w}{\partial x}\right) \\ v(x,y,z) &= v_0(x,y) + z\theta_y(x,y) + z^3\left(-\frac{4}{3h^2}\right)\left(\theta_y(x,y) + \frac{\partial w}{\partial y}\right) \\ w(x,y,z) &= w_0(x,y) \end{aligned} \tag{1.22}$$

The stiffness matrices can be derived repeating the procedure shown for the CLT . In this case, and for all the higher order theories, the higher order terms will give birth to *higher order stiffness matrices*, like the ones below [20]:

$$\begin{aligned} &\textit{Third Order Stiffness}: \quad E_{ij} = \int_{-t/2}^{t/2} (\bar{C_{ij}})_k z^3 dz = \frac{1}{4}\sum_{k=1}^{N} (\bar{C_{ij}})_k (z_k^4 - z_{k-1}^4) \\ &\textit{Fourth Order Stiffness}: \quad F_{ij} = \int_{-t/2}^{t/2} (\bar{C_{ij}})_k z^4 dz = \frac{1}{5}\sum_{k=1}^{N} (\bar{C_{ij}})_k (z_k^5 - z_{k-1}^5) \\ &\textit{Sixth Order Stiffness}: \quad H_{ij} = \int_{-t/2}^{t/2} (\bar{C_{ij}})_k z^6 dz = \frac{1}{7}\sum_{k=1}^{N} (\bar{C_{ij}})_k (z_k^7 - z_{k-1}^7) \end{aligned} \tag{1.23}$$

A claimed advantage of the TSDT over the FSDT is that the cubic expansion of the displacements automatically produces a parabolic distribution of transverse shear stresses over the cross section and as a consequence no shear correction factors are needed.
If on the one hand the mathematical procedure has no pitfalls, on the other hand the introduction of higher order stiffness terms introduces some interpretation difficulties from the purely physical and mechanical point of view; these matrices, in fact relate higher order stress resultants to the higher order deformations directly coming from the displacement field of Eq. 1.22. All of them, despite being mathematically consistent, have no direct counterparts in the elasticity theory. Moreover, if we look at Eq. 1.22 we notice that the first order derivative of the transverse deflection appears explicitly like in the CLT. As it will be further explained in a later section, the presence of derivatives in the model imposes the use of higher order interpolation functions for the finite element implementation; it is general practice to prefer linear interpolation functions to reduce the computational cost of the simulations. A TSDT that respects this guideline is the one proposed by Kant et al. [43], which only adds a third order term rotation to the FSDT. This model, described in Eq. 1.24 will be used later as a benchmark model for

the finite element model of the proposed development and analysis.

$$\begin{aligned} u(x,y,z) &= u_0(x,y) + z\theta_x(x,y) + z^3\theta^*(x,y) \\ v(x,y,z) &= v_0(x,y) + z\theta_y(x,y) + z^3\theta^*(x,y) \\ w(x,y,z) &= w_0(x,y) \end{aligned} \tag{1.24}$$

where θ^* represents the rotation of the cross-section proportional to the third-order term.

1.3 Layer-wise Theories

The elasticity solution obtained by Pagano [44, 45] shows that the actual displacement distribution in the thickness direction varies in a piece-wise manner. This result is a direct consequence of the continuity conditions of transverse shear stresses at layers' interface. All ESLT, on the other hand, predict the continuity of the displacement in the thickness direction thus implying the discontinuity of transverse shear stresses. The magnitude of transverse shear stresses is an important parameter in crack propagation and delamination initiation [46, 47] and its correct estimation is essential for the integrity of the laminated components.

The main objective of *Layer-wise Theories* (LWT) is to tackle the two requirements of transverse shear stresses continuity at layers' interface and piece-wise variation of displacements through the thickness, referred to as C_z^0 *requirements* by Carrera [48, 49]. Reddy [20] distinguishes between *full LWT*, which use a layer-wise expansions for all the three displacements components, and *partial LWT*, which use a layer-wise expansion for the in-plane components only. Fig. 1.7 shows the kind of behaviour that LWT seek to obtain.

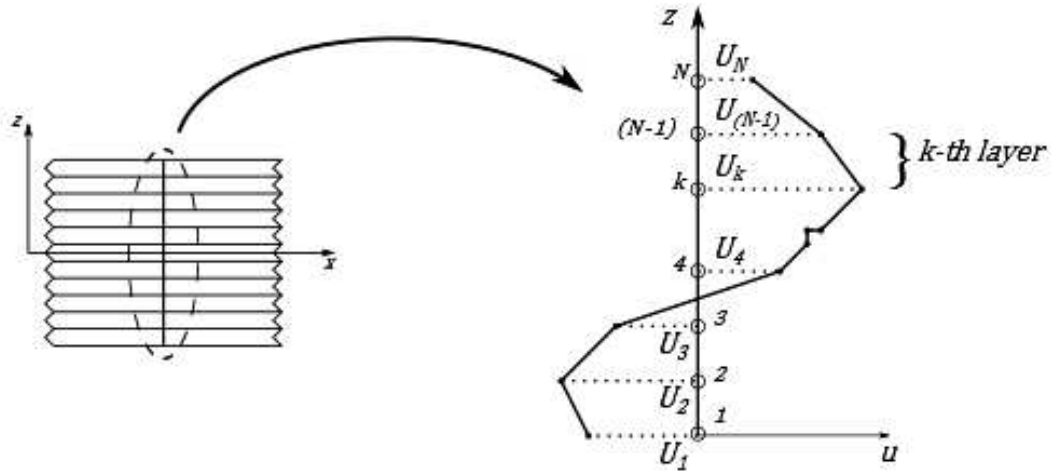

Fig. 1.7. Layer-wise distribution of the axial displacement u through the thickness

Many authors addressed the problem [50–56]. Most of these models assume a piecewise variation of the in-plane displacements in the through the thickness direction and then impose continuity conditions at layers interface, either in therms of displacements or in terms of stresses, the latter giving rise to *mixed formulations*. Reddy also proposed a layer-wise model [57, 58] oriented at finite element implementation thanks to the choice of Lagrangian functions for the expansion of the displacements in the thickness direction. As an example, the Carrera mixed-formulation [59] and the Reddy Lagrangian formulation [36] are reported in Eqs. 1.27.

Carrera Mixed Layer-wise Model

Stress-strain relationship in mixed form

$$\begin{aligned} \sigma_{ph}^k &= C_{pp}^k \varepsilon_{pG}^k + C_{pn}^k \sigma_{nM}^k \\ \varepsilon_{nH}^k &= C_{np}^k \varepsilon_{pG}^k + C_{nn}^k \sigma_{nM}^k \end{aligned} \tag{1.25}$$

Layer-wise expansion for stresses and strains

$$\begin{aligned} u^k &= F_t u_t^k + F_b u_b^k + F_r u_r^k = F_\tau u_{tau}^k \\ \sigma_{nM}^k &= F_t \sigma_{nt}^k + F_b \sigma_{nb}^k + F_r \sigma_{nr}^k = F_\tau \sigma_{n\tau}^k \end{aligned} \tag{1.26}$$

where the subscripts have the following meaning:
n=transverse component;
p=in-plane components;
H=stress given by the Hookes' law;
G=strains given by geometrical relationship;
M=stresses assumed by the model
F_τ=functions of z expressed by Legendre polynomials.

Reddy Layer-wise Model

$$\begin{aligned} u^k(x,y,z) &= \sum_{j=1}^{N_L} u_j^k(x,y)\phi_j^k(z) \\ v^k(x,y,z) &= \sum_{j=1}^{N_L} v_j^k(x,y)\phi_j^k(z) \\ w^k(x,y,z) &= \sum_{j=1}^{N_L} u_j^k(x,y)\psi_j^k(z) \end{aligned} \tag{1.27}$$

where $\{u^k, v^k, w^k\}$ are displacements in the $k-th$ layer and $\{\phi_j^k(z), \psi_j^k(z)\}$ are continuous functions of z. Being necessary to impose continuity conditions at layers' interface, it is evident that the number of unknowns is a function of the number of layers. This approach can then become highly expensive for thick laminates.

1.4 *Zigzag Theories* review

The proposition of *Zigzag Theories* (ZZT) originates from the need of combining the low computational cost of ESLT and the capabilities of LWT to reproduce the piece-wise behaviour of displacements as predicted by the 3D elasticity solution. In order to do so, ZZT take an equivalent single layer model and insert a piece-wise function of the thickness coordinate multiplied by an unknown displacement or rotation variable. The main difference and also main advantage of ZZT with respect to LWT is that the number of unknowns in the model is independent of the number of layers, making it more efficient from the computational point of view. Sometimes this difference is overlooked and confusion between the theories is made [60]. The additional variable is still an equivalent homogenised one but once multiplied by the z-function, the Zigzag model is able to reproduce the desired piece-wise behaviour.
The first to propose this approach was Murakami [61]. The zigzag function that he proposed has the form:

$$M(z) = (-1)^k \left(\frac{2}{h_k}\right) z_k \qquad \text{with } z_k = z - z_{k0}$$

being z_{k0} a local coordinate, the origin of which is at the centre of the k-th layer. The Murakami function can be superimposed to both linear and higher-order models; its magnitude is equal to one for each layer, the slope assumes opposite sign between adjacent layers and its magnitude is a function of the layer thickness. The unknown variable associated with the function is a displacement which adds up to the one predicted by the ELST chosen as base model. Rao and Mayer [62], Makhecha [63], Demasi [56, 64], Brank and Carrera [54], Auricchio and Sacco [65] investigated the inclusion of the Murakami zigzag function in first- and higher-order theories. The *Carrera Unified Formulation* (CUF) [66, 67] is an example of application of the Murakami function to generic $n^{th} - order$ models (Fig.1.8), expressed in compact form in Eq. 1.28

$$\mathbf{u}(x, y, z) = u_0 + u_{ZZ}(-1)^k \left(\frac{2}{h_k}\right) z_k + z^r u_r, \qquad r = 1, 2, ..., M \tag{1.28}$$

where u is the vector of generalised displacements, r is the order of the expansion and u_{ZZ} is the Zigzag displacement variable.

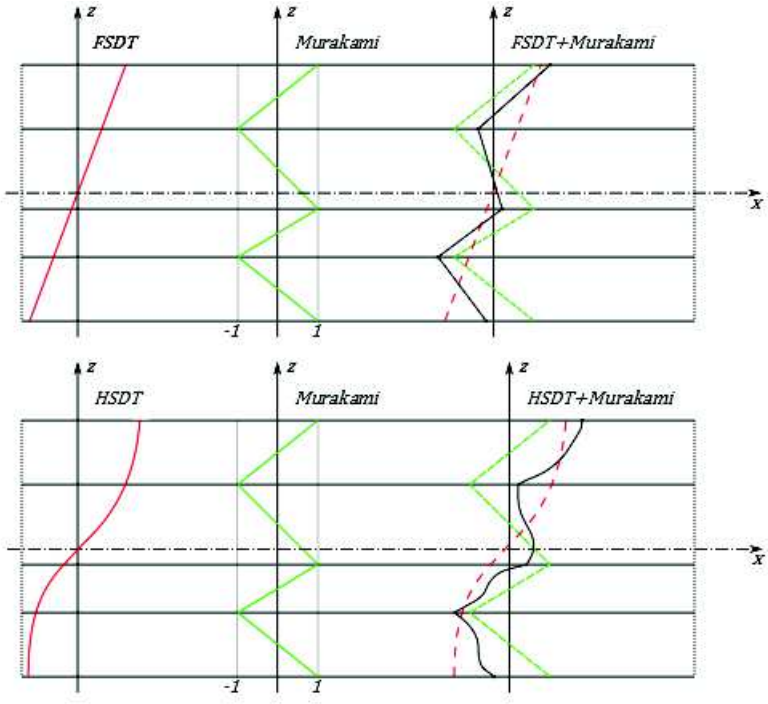

Fig. 1.8. Examples of superposition of the Murakami Zigzag function to FSDT an HSDT

As Murakami himself highlighted, however, his function was developed for laminates showing periodicity in material properties and geometry, for instance cross-ply or angle-ply laminates with uniform lamina thickness.

An interesting model is the one proposed by Ren [68,69], in which the Kirchhoff theory is enriched by a function of the thickness embedding material properties and derived from Lekhnitskii [23]. More recently Di Sciuva [70] and Averill [71] proposed two displacement Zigzag models which served as a starting point for Tessler for the development of his *Refined Zigzag Theory* (RZT) [72,73]. Di Sciuva's model, originally presented for beams, can be written as:

$$\begin{aligned} u^k(x,z) &= u_0(x) + z\theta(x) + \phi^k_{DS}(z)\psi(x) \\ w(x,z) &= w_0(x) \end{aligned} \tag{1.29}$$

where:

$\phi^{(k)}_{DS}(z)$= Di Sciuva's zigzag function amplitude $\qquad$ $\psi(x,y)$=Zigzag rotation

To determine the Zigzag function, Di Sciuva [70] enforced a set of continuity constraints on stresses, namely he imposed the equality of transverse shear stresses at layers' interface which implies that all layers share the same constant transverse shear stresses. However, this assumption only defines $N-1$ constraints against the $N+1$ interfacial displacements, being N the number of layers. The two missing equations are found

by imposing that the Zigzag function vanishes in the bottom layer. As a consequence, the transverse shear stresses in all layers are equal to that in the layer for which zero interfacial displacement was specified. Moreover, the choice of a layer with zero valued displacement at interface creates a bias in the definition of the homogenised modulus and, in addition to that, it excludes one of the layers from the calculation while the zigzag function should depend on all layers. The model of Di Sciuva presents two other theoretical difficulties: integration of the transverse shear stresses over the cross section gives a value that is different from that predicted by the beam's equilibrium equation; a non vanishing average transverse shear stress is found at clamps. On the other hand, the model proposed by Di Sciuva automatically returns to the base ESLT theory when homogeneous beams are considered.

The theoretical difficulties encountered by Di Sciuva motivated the Zigzag model of Averill [71]. Averill's model uses a penalty method to impose the continuity of transverse shear stresses through the thickness of the laminate. His model reads:

$$\begin{aligned} u^k(x,z) &= u_0(x) + (z + h - 2h^{(1)})\theta(x) + \phi_A^k(z)\psi(x) \\ w(x,z) &= w_0(x) \end{aligned} \tag{1.30}$$

where:

$\phi_A^{(k)}(z)$= Averill's zigzag function $\qquad$ $\psi(x,y)$= Zigzag rotation amplitude

The same approach of Di Sciuva is followed: one layer is chosen for which the interfacial displacement vanishes; in particular Eq. 1.30 holds when the second layer of a three-layer laminate is chosen. Transverse shear stress continuity is enforced by imposing that the average shear modulus is equal to that of the fixed layer. As Di Sciuva's model, Averill's model as well experiences some inconsistency at clamps and when transverse shear stresses are integrated over the cross-section. Moreover, it lacks invariance as the average modulus of the laminate depends on the layer chosen to have zero interfacial displacement. Fig. 1.9 shows the through the thickness variation foreseen by Di Sciuva and Averill theories.

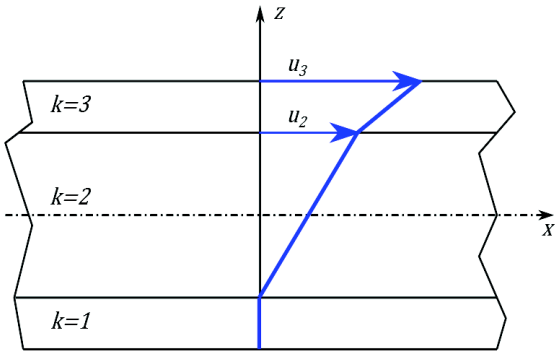

(a) *Di Sciuva's Zigzag displacements*

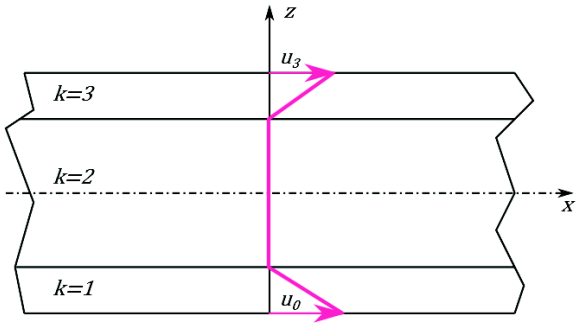

(b) Averill's Zigzag displacements

Fig. 1.9. Zigzag displacement as predicted by Di Sciuva (a) and Averill (b)

1.5 The *Refined Zigzag Theory*

Tessler [72] started from the theories of Di Sciuva and Averill to develop his *Refined Zigzag Theory* (RZT). The main difference between the RZT and Di Sciuva's and Averill's models is that the zigzag function is set to vanish on the bottom and top surface of the laminate rather than within one of the internal layers. A direct consequence of this assumption is that each layer contributes to the Zigzag deformation of the structure. Fig. 1.10 shows the Zigzag displacement predicted by the RZT and the geometry convention.

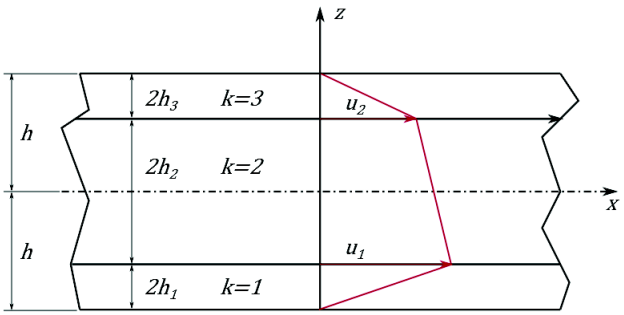

Fig. 1.10. Zigzag displacement predicted by the RZT

The mathematical model for a beam is given by:

$$\begin{aligned} u^k(x,z) &= u_0(x) + z\theta(x) + \phi^k(z)\psi(x) \\ w(x,z) &= w_0(x) \end{aligned} \tag{1.31}$$

The Zigzag function $\phi(z)$ can be expressed in terms of the interfacial displacement $u_x^{(k)}$. In order to do so, a local coordinate system is defined which is centred on the $k-th$ layer mid-axis and is made non-dimensional dividing by the $k-th$ layer thickness (Eqs. 1.32).

$$\xi^{(k)} = \frac{(z - z^{(k-1)}) + h^{(k)}}{h^{(k)}} \qquad k = 1, ..., N; \quad z \in [-h, h]; \quad \xi^{(k)} \in [-1, 1] \tag{1.32}$$

This leads to the following set of equalities (Eqs. 1.33):

$$z^{(0)} = -h; \quad z^{(k)} = z^{(k-1)} + 2h^{(k)}; \quad z^{(N)} = h; \tag{1.33}$$

The Zigzag function is assumed to vary linearly within each layer so that the following relations hold:

$$\phi^{(k)} = u^{(k-1)} \text{ for } \xi^{(k)} = -1; \quad \phi^{(k)} = u^{(k)} \quad \text{for } \xi^{(k)} = 1. \tag{1.34}$$

The Zigzag function in terms of interfacial displacement is then written as:

$$\phi^{(k)} = \frac{1}{2}(1 - \xi^{(k)})u^{(k-1)} + \frac{1}{2}(1 + \xi^{(k)})u^{(k)} \tag{1.35}$$

By definition $\beta^{(k)} \equiv \frac{d\phi^{(k)}}{dz}$, which leads to:

$$\beta^{(k)}(z) = \frac{u^{(k)} - u^{(k-1)}}{2h^{(k)}} \tag{1.36}$$

Starting from Eq. 1.31 we can write the strains in the beam as

$$\begin{aligned} \varepsilon_x^k(x,z) &= \frac{\partial u_0}{\partial x} + z\frac{\partial \theta}{\partial x} + \phi^{(k)}(z)\frac{\partial \psi}{\partial x} \\ \gamma_{xz}^{(k)}(x,z) &= \theta(x) + \frac{\partial \phi}{\partial z}\psi(x) + \frac{\partial w_0}{\partial x} = \gamma(x) + \beta^k(z)\psi(x) \\ \text{with } \gamma &= \theta(x) + \frac{\partial w_0}{\partial x} \end{aligned} \tag{1.37}$$

The quantity γ represents the average shearing strain in the FSDT sense. To simplify the subsequent notation it is useful to define the function $\eta(x) \equiv \gamma(x) - \psi(x)$ which allows us to rewrite the transverse shear deformation as

$$\gamma_{xz}^{(k)}(x,z) = (1 + \beta^{(k)})\gamma - \beta^{(k)}\eta \tag{1.38}$$

and the associated transverse shear stress as

$$\tau_{xz}^{(k)} = G_{xz}^{k}(1+\beta^{(k)})\gamma - G_{xz}^{k}\beta^{(k)}\eta \tag{1.39}$$

The piece-wise constant function $\beta^{(k)}$ has a useful property which verifies that γ is exactly the shear angle of the FSDT (Eq. 1.40, 1.41).

$$\int_A \beta^{(k)} dA \equiv \frac{A}{2h}\sum_{k=1}^{N} 2h^{(k)}\beta^{(k)} = \frac{A}{2h}(u^{(N)} - u^{(0)}) = 0 \tag{1.40}$$

$$\gamma = \frac{1}{A}\int_A \gamma^{(k)_{xz}} dA. \tag{1.41}$$

The property expressed by Eq. 1.40 can also be employed to show that $\psi(x)$ is a weighted-average shear strain (Eq. 1.42)

$$\psi = \frac{1}{\int_A (\beta^{(k)})^2 dA}\int_A \beta^{(k)}\gamma_{xz}^{(k)} dA. \tag{1.42}$$

In Tessler model the continuity is enforced on the $\gamma(x)$ variable such that Eq. 1.43 holds:

$$G_{xz}^{(k)}(1+\beta^{(k)}) = G_{xz}^{(k+1)}(1+\beta^{(k+1)}) \quad \text{for } k = 1, ..., N \tag{1.43}$$

which implies that $G \equiv G_{xz}^{(k)}(1+\beta^{(k)}) = constant$, being G a beam material constant and from which we can express $\beta^{(k)}$ as

$$\beta^{(k)} = \frac{G}{G_{xz}^{(k)}} - 1 \tag{1.44}$$

and by integration of Eq. 1.44 over the beam cross section we finally obtain the beam homogenised modulus as a function of the layers' transverse shear modulus and thickness (Eq. 1.45)

$$G = \left(\frac{1}{A}\int_A \frac{dA}{G_{xz}^{(k)}}\right)^{-1} \equiv h\left(\sum_{k=1}^{N}\frac{h^{(k)}}{G_{xz}^{(k)}}\right)^{-1}. \tag{1.45}$$

The beam axial displacement, transverse shear strain and transverse shear stress can now be expressed in terms of the Zigzag quantities previously defined (Eqs. 1.46- 1.48)

$$u^{(k)} = u^{(k-1)} + 2h^{(k)}\left(\frac{h}{G_{xz}^{(k)}\sum_{k=1}^{(N)}\frac{h^{(k)}}{G_{xz}^{(k)}}} - 1\right) \tag{1.46}$$

$$\gamma^{(k)} = \eta + \frac{G}{G_{xz}^{(k)}\psi} \tag{1.47}$$

$$\tau_{xz}^{(k)} = G\psi + G_{xz}^{(k)}\eta \equiv G\gamma + (G_{xz}^{(k)} - G)\eta \tag{1.48}$$

The model so derived overcomes the issues emerged in Di Sciuva's and Averill's models. With respect to the Murakami Zigzag model, the RZT defines the Zigzag function in terms of both layers' geometry and material properties. This difference is crucial to the accuracy of the model when non-periodic structures are considered, i.e. laminates with arbitrary lamination schemes, non-homogeneous layers' thickness, sandwiches. The additional cost of the model is that of an additional unknown variable for the beam and two unknown variables for plates. The upcoming chapter will discuss the development of a finite element based on the RZT.

Chapter 2

The development of a 1D element and benchmark against state of the art theories

2.1 The development of a 1D Finite Element

The theories described in the previous chapter serve as a starting point for the development of dedicated numerical models for the analysis of composite and sandwich structures.

2.1.1 The Finite Element Method for 1D structural problems

The Finite Element Method (FEM) is an essential tool in engineering practice. For many engineering problems exact solutions are not always available or easy to find. The FEM provides an approximate solution by dividing the problem's domain into *elements* and solving the problem's characteristic equations at specific locations for each element [74]. More precisely, a continuum is discretised into non-overlapping domains of simple geometry, the *finite elements*. The differential or integral equations, which usually describe physical phenomena, are reported into polynomial expansions on the element domain. By solving equilibrium equations at elements' corners, *nodes*, the numerical solution to the original problem is recomposed [75].
A finite element model requires the geometrical description of the structure, the mechanical properties of the materials, the definition of loads and constraints and the definition of the type of discretisation, such as element shape and size. Elements differ from one another depending on the number of variables associated with their nodes, *degrees of*

freedom (DOF), the number of nodes and the underlying beam theory which in turns determines the degree of the polynomial interpolation, or *shape functions*, used to reconstruct the spatial variation of DOF along the element. The main feature of the shape functions is that they vary between 0 and 1 such that when they assume unit value in one node they are null in all the others.

In one-dimensional (1D) structural analysis available elements are *bars, rods* and *beams*. Rods can withstand axial and torsional loads, bars are prismatic with axial, torsional and bending stiffness and beams can be seen as a generalisation of bars as they have the same stiffness characteristics and allow variable cross-section, shear centre offset from the neutral axis and other properties [76]. The stiffness characteristics of the elements, expressed in matrix form, are obtained by following one of two methods, the *direct method* or the *variational method* [77]. In the direct method, the equilibrium equations for the elements are written and the stiffness matrix obtained thanks to the force-displacement relations provided by the mechanics of materials. This procedure is feasible only when such mathematical relations exist and are easy to handle. In all other cases the variational formulation can be used, starting from the principle of virtual work or the minimum total potential energy principle [75].

In dynamic analyses, information on the mass of the structure is also needed and must be repartitioned on elements [78] and the accuracy of the results will depend on the method chosen [79]. This process is usually referred to as *lumping*. The most common lumping techniques are the *direct mass lumping* (DML) and the *variational mass lumping* (VML) [80]. When DML is pursued, the total mass of the element is merely split among the nodes of the element. Physically, the masses will show no inertial interaction. This procedure encounters physical inconsistencies when rotational DOF are present as the process does not preserve angular momentum [81] and other lumping techniques are to be used [82]. Alternative methods have been proposed [83, 84] but they are still not well established. VML starts from the kinetic energy of the beam; if the nodal velocities are interpolated using the same shape functions used for the displacement, we talk about *consistent mass matrix formulation*. The result is usually a non-diagonal mass matrix, which physically means that inertial interactions are accounted for.

The set of elements will in the end need to behave as the continuum that they represent; the assembly process takes each element's stiffness and mass matrices and recombine them in the global stiffness and mass matrices which eventually approximate the stiffness and mass of the real structure.

2.1.2 The RZT beam element

Few authors developed beam elements based on the Zigzag kinematics. Averill himself proposed a beam element with linear, quadratic and cubic Zigzag functions [85, 86]. Alam et al. [87] proposed a 2-noded beam element starting from Averill's zigzag theory and including a cubic in-plane displacement in each layer. Vidal and Polit [88] proposed a sine beam element using the Murakami zigzag function. Gherlone et al. [89] and Tessler et al. [90] proposed a C^0-continuous beam element based on the RZT. Oñate et al. [91, 92] developed a RZT beam but following a different procedure compared to Gherlone and Tessler.
Starting from Eq. 1.31 a beam element was built in MATLAB®. [93]. The model allows the use of linear interpolation functions (Eqs. 2.1, Fig. 2.1) since continuity is required only for the displacements and not for their derivatives (cf. 1.31 - 1.37).

$$N_1(x) = \frac{1-x}{l_{(e)})} \qquad N_2(x) = \frac{x}{l_{(e)}} \tag{2.1}$$

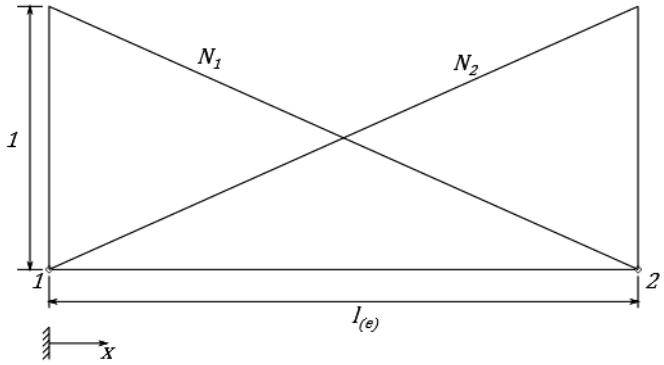

Fig. 2.1. RZT beam

Each node has four DOFs, i.e. the unknowns in Eq. 1.31. They can be grouped in the vector of generalised coordinates $\boldsymbol{a}^{(e)} = [u_1, w1, \theta_1, \psi_1, u_2, w_2, \theta_2, \psi_2]$. The spatial variation of the degrees of freedom along the element is then given by:

$$u(x) = u_1 N_1(x) + u_2 N_2(x) \tag{2.2}$$

$$w(x) = w_1 N_1(x) + w_2 N_2(x) \tag{2.3}$$

$$\theta(x) = \theta_1 N_1(x) + \theta_2 N_2(x) \tag{2.4}$$

$$\psi(x) = \psi_1 N_1(x) + \psi_2 N_2(x) \tag{2.5}$$

The element stiffness matrix is found by following the procedure described in reference [94]. The strains in Eqs. 1.37 can be written as:

$$\varepsilon_x^k(x,z) = \frac{\partial u_0}{\partial x} + z\frac{\partial \theta}{\partial x} + \phi^{(k)}(z)\frac{\partial \psi}{\partial x} = \left[1, z, \phi^{(k)}\right] \begin{Bmatrix} \frac{\partial u_0}{\partial x} \\ \frac{\partial \theta}{\partial x} \\ \frac{\partial \psi}{\partial x} \end{Bmatrix} = \boldsymbol{S}_p \hat{\boldsymbol{\varepsilon}}_p \tag{2.6}$$

$$\gamma_{xz}^{(k)}(x,z) = \gamma(x) + \beta^k(z)\psi(x) = \left[1, \beta^{(k)}\right] \begin{Bmatrix} \gamma \\ \psi \end{Bmatrix} = \boldsymbol{S}_t^{(k)} \hat{\boldsymbol{\varepsilon}}_t \tag{2.7}$$

with

$$\boldsymbol{S}_p = \left[1, z, \phi^{(k)}\right], \quad \hat{\boldsymbol{\varepsilon}}_p = \left\{ \tfrac{\partial u_0}{\partial x}, \tfrac{\partial \theta}{\partial x}, \tfrac{\partial \psi}{\partial x}^T \right\} \tag{2.8}$$

$$\boldsymbol{S}_t^{(k)} = \left[1, \beta^{(k)}\right], \quad \hat{\boldsymbol{\varepsilon}}_t = \left\{\gamma, \psi\right\} \tag{2.9}$$

where p and t refer to in-plane and out-of-plane quantities respectively and the superscript (k) refers to the $k-th$ layer. The in-plane and out-of-plane stresses are found by application of the Hooke's law (Eqs. 2.11)

$$\sigma_x^{(k)} = E^{(k)} \varepsilon_x^{(k)} = E^{(k)} \boldsymbol{S}_p^{(k)} \hat{\boldsymbol{\varepsilon}}_p^{(k)} \tag{2.10}$$

$$\tau_{xz}^{(k)} = G^{(k)} \gamma_{xz}^{(k)} = G^{(k)} \boldsymbol{S}_t^{(k)} \hat{\boldsymbol{\varepsilon}}_t^{(k)} \tag{2.11}$$

Integration of layers' stresses over the cross-section returns the stress resultants and from the resulting constitutive equations we can define the in-plane and out-of-plane stiffness matrices (Eqs. 2.12-2.13).

$$\hat{\boldsymbol{\sigma}}_p = \begin{Bmatrix} N \\ M \\ M_\phi \end{Bmatrix} = \iint_A \left[\boldsymbol{S}_p^{(k)}\right]^T \sigma_p^{(k)} dA = \left(\iint_A \left[\boldsymbol{S}_p^{(k)}\right]^T \left[\boldsymbol{S}_p^{(k)}\right] E^{(k)} dA \right) \hat{\boldsymbol{\varepsilon}}_p^{(k)} = \hat{\boldsymbol{D}}_p \hat{\boldsymbol{\varepsilon}}_p \tag{2.12}$$

$$\hat{\boldsymbol{\sigma}}_t = \begin{Bmatrix} Q \\ Q_\phi \end{Bmatrix} = \iint_A \left[\boldsymbol{S}_t^{(k)}\right]^T \tau_{xz}^{(k)} dA = \left(\iint_A \left[\boldsymbol{S}_t^{(k)}\right]^T \left[\boldsymbol{S}_t^{(k)}\right] G^{(k)} dA \right) \hat{\boldsymbol{\varepsilon}}_t^{(k)} = \hat{\boldsymbol{D}}_t \hat{\boldsymbol{\varepsilon}}_t \tag{2.13}$$

M_ϕ and Q_ϕ are an additional bending moment and shear force associated with the zigzag unknown respectively. Explicit expressions for the in-plane and out-of-plane stiffness matrices are given in Eqs. 2.14-2.15.

$$\hat{\boldsymbol{D}}_p = \iint_A E^{(k)} \begin{bmatrix} 1 & z & \phi^{(k)} \\ z & z^2 & z\phi^{(k)} \\ \phi^{(k)} & z\phi^{(k)} & \left(\phi^{(k)}\right)^2 \end{bmatrix} dA = \begin{bmatrix} A_{11} & B_{12} & B_{13} \\ B_{12} & D_{11} & D_{12} \\ B_{13} & D_{12} & D_{22} \end{bmatrix} \tag{2.14}$$

$$\hat{\boldsymbol{D}}_t = \iint_A G^{(k)} \begin{bmatrix} 1 & \beta^{(k)} \\ \beta^{(k)} & \left(\beta^{(k)}\right)^2 \end{bmatrix} dA = \begin{bmatrix} V_{11} & V_{12} \\ V_{12} & V_{22} \end{bmatrix} \tag{2.15}$$

In the above integrals we can recognise axial, bending, coupling and shearing stiffness presented in Chapter 1 (Eqs. 1.16-1.18). Three additional stiffness matrices arise from the zigzag model: B_{13}, D_{13}, V_{12} can be thought of as the extensional-, bending- and

shearing-zigzag coupling stiffness matrices, while D_{22} and V_{22} are the zigzag bending and zigzag shearing stiffness matrices respectively.
The RZT unknowns can be written in terms of the element DOF thanks to Eqs. 2.2-2.5:

$$\boldsymbol{u} = \begin{Bmatrix} u_0 \\ w_0 \\ \theta \\ \psi \end{Bmatrix} = \sum_{i=1}^{2} N_i \boldsymbol{a}_i^{(e)} \tag{2.16}$$

The strains vector defined in Eqs. 2.6-2.7 can be expressed in terms of the nodal vector according to following equalities

$$\hat{\boldsymbol{\varepsilon}}_p = \boldsymbol{B}_p \boldsymbol{a}^{(e)}; \quad \hat{\boldsymbol{\varepsilon}}_t = \boldsymbol{B}_t \boldsymbol{a}^{(e)} \tag{2.17}$$

The two newly introduced matrices (Eqs. 2.18) contain the derivatives of the shape functions N_i and allows us to express the strains in terms of generalised coordinates.

$$\boldsymbol{B}_{pi} = \begin{bmatrix} \frac{\partial N_i}{\partial x} & 0 & 0 & 0 \\ 0 & 0 & \frac{\partial N_i}{\partial x} & 0 \\ 0 & 0 & 0 & \frac{\partial N_i}{\partial x} \end{bmatrix}; \quad \boldsymbol{B}_{ti} = \begin{bmatrix} 0 & \frac{\partial N_i}{\partial x} & N_i & 0 \\ 0 & 0 & 0 & N_i \end{bmatrix}; \quad i = 1, ..., \text{number of nodes} \tag{2.18}$$

Application of the virtual work principle allows us to finally write the element stiffness matrix, $\boldsymbol{K}^{(e)} = \boldsymbol{K}_p^{(e)} + \boldsymbol{K}_t^{(e)}$ where:

$$\boldsymbol{K}_{p_{ij}}^{(e)} = \int_{l_{(e)}} \boldsymbol{B}_{p_i}^T \hat{\boldsymbol{D}}_p \boldsymbol{B}_{p_j} dx; \quad \boldsymbol{K}_{t_{ij}}^{(e)} = \int_{l_{(e)}} \boldsymbol{B}_{t_i}^T \hat{\boldsymbol{D}} \boldsymbol{B}_{t_j} dx \tag{2.19}$$

In Eqs. 2.19 the subscripts i and j are the element nodes.
The above integrals are usually calculated using numerical methods such as the *Gauss Quadrature* [95] which evaluates the integrand function at specific location along the element length, multiplies each value for a corresponding weight and then sum all the contributions.

$$I = \int_{-1}^{1} f(\xi) d\xi \Longrightarrow I \simeq I_{GQ} = \sum_{i=1}^{q} f(\xi_i) W_i \tag{2.20}$$

The number of sampling points depends on the order of the function $f(\xi_i)$, remembering that a Gauss Quadrature of order q exactly integrates a polynomial function of order $n = 2q - 1$. The use of numerical integration allows us to outflank the numerical problems which plague all elements based on the Timoshenko beam, i.e. *shear locking*. In brief, shear locking occurs in Timoshenko beam as the beam becomes slender and the shearing effects become negligible, such that the solution should converge to the Euler-Bernoulli one [94]. In practice, the Timoshenko beam behaves more rigidly as the

beam becomes more slender, therefore being unable to reproduce the correct solution. Reduced integration under-integrates the shear stiffness terms, thus reducing the effect of the transverse shear stiffness on the solution.
Numerically speaking, splitting the stiffness matrix between the in-plane and out-of-plane part makes it easier to perform numerical integration using a different Gauss Quadrature order, if necessary. In this case, the order needed for the exact integration of the in-plane stiffness matrix is $q_p = 2$; reduced integration of the out-of-plane stiffness matrix is performed using an order $q_t = 1$.

2.2 Finite elements benchmarking

The developed RZT beam accuracy was tested against other beam models. The benchmarking elements were chosen so that a multi-purpose MATLAB code could be implemented. In particular, the FSDT, the Murakami Zigzag Model (MZM) and Kant Third Order Shear Deformation Theory (KTSDT) were chosen. All these theories can actually be described by a linear element, allowing for a common infrastructure code in which different theories can be chosen. The objective of the comparison is to:

- compare the RZT and MZM;
- compare the Zigzag approach to the HSDT approach;
- verify the CUF, i.e. the superposition of the zigzag function to HSDT.

For easiness of understanding, the models, specified for a beam, and the resulting stiffness matrices for the benchmarking elements are reported below.

2.2.1 FSDT beam element

Kinematic model

$$\begin{aligned} u(x,y,z) &= u_0(x,y) + z\theta_x(x,y) \\ w(x,y,z) &= w_0(x,y) \end{aligned} \tag{2.21}$$

Stiffness matrix

$$\hat{\boldsymbol{D}}_p = \iint_A E^{(k)} \begin{bmatrix} 1 & z \\ z & z^2 \end{bmatrix} dA; \quad \hat{\boldsymbol{D}}_t = \iint_A G^{(k)} dA; \quad \hat{\boldsymbol{D}} = \begin{bmatrix} \hat{\boldsymbol{D}}_p & [0]_{2x1} \\ [0]_{1x2} & \hat{\boldsymbol{D}}_t \end{bmatrix} \tag{2.22}$$

2.2.2 KTSDT beam element

Kinematic model

$$\begin{aligned} u(x,y,z) &= u_0(x,y) + z\theta_x(x,y) + z^3\theta^*(x,y) \\ w(x,y,z) &= w_0(x,y) \end{aligned} \tag{2.23}$$

Element stiffness matrix

$$\hat{\boldsymbol{D}}_p = \iint_A E^{(k)} \begin{bmatrix} 1 & z & z^3 \\ z & z^2 & z^4 \\ z^3 & z^4 & z^6 \end{bmatrix} dA; \quad \hat{\boldsymbol{D}}_t = \iint_A G^{(k)} \begin{bmatrix} 1 & z^2 \\ z^2 & z^4 \end{bmatrix} dA; \quad \hat{\boldsymbol{D}} = \begin{bmatrix} \hat{\boldsymbol{D}}_p & [0]_{3x2} \\ [0]_{2x3} & \hat{\boldsymbol{D}}_t \end{bmatrix} \tag{2.24}$$

2.2.3 Zigzag theories + FSDT beam element

Kinematic model

$$\begin{aligned} u(x,y,z) &= u_0(x,y) + z\theta_x(x,y) + f_i^{(k)}(z)\delta_i(x,y) \\ w(x,y,z) &= w_0(x,y) \end{aligned} \tag{2.25}$$

where

$$i = Murakami, RZT; \quad \delta_i(x,y) = u_{ZZ}(x,y), \psi(x,y) \tag{2.26}$$

Element stiffness matrix

$$\begin{aligned} \hat{\boldsymbol{D}}_p &= \iint_A E^{(k)} \begin{bmatrix} 1 & z & f_i^{(k)} \\ z & z^2 & zf_i^{(k)} \\ f_i^{(k)} & zf_i^{(k)} & (f_i^{(k)})^2 \end{bmatrix} dA; \quad \hat{\boldsymbol{D}}_t = \iint_A G^{(k)} \begin{bmatrix} 1 & \beta(k) \\ \beta(k) & (\beta(k))^2 \end{bmatrix} dA; \\ \hat{\boldsymbol{D}} &= \begin{bmatrix} \hat{\boldsymbol{D}}_p & [0]_{3x2} \\ [0]_{2x3} & \hat{\boldsymbol{D}}_t \end{bmatrix} \end{aligned} \tag{2.27}$$

2.2.4 Zigzag theories + KTSDT beam element

Kinematic model

$$\begin{aligned} u(x,y,z) &= u_0(x,y) + z\theta_x(x,y) + f_i^{(k)}(z)\delta_i(x,y) + z^3\theta^*(x,y) \\ w(x,y,z) &= w_0(x,y) \end{aligned} \tag{2.28}$$

where

$$i = Murakami, RZT; \quad \delta_i(x,y) = u_{ZZ}(x,y), \psi(x,y) \tag{2.29}$$

Element stiffness matrix

$$\begin{aligned}
\hat{\boldsymbol{D}}_p &= \iint_A E^{(k)} \begin{bmatrix} 1 & z & f_i^{(k)} & z^3 \\ z & z^2 & zf_i^{(k)} & z^4 \\ f_i^{(k)} & zf_i^{(k)} & (f_i^{(k)})^2 & z^3 f_i^{(k)} \\ z^3 & z^4 & z^3 f_i^{(k)} & z^6 \end{bmatrix} dA; \\
\hat{\boldsymbol{D}}_t &= \iint_A G^{(k)} \begin{bmatrix} 1 & \beta(k) & z^2 \\ \beta(k) & (\beta(k))^2 & z^2\beta(k) \\ z^2 & z^2\beta^{(k)} & z^4 \end{bmatrix} dA; \\
\hat{\boldsymbol{D}} &= \begin{bmatrix} \hat{\boldsymbol{D}}_p & [0]_{4x3} \\ [0]_{3x4} & \hat{\boldsymbol{D}}_t \end{bmatrix}
\end{aligned} \tag{2.30}$$

2.3 Assessment of the beam elements vs Elasticity Theory and a refined finite element model

The performance of the RZT beam element is first assessed by comparing its results against the analytical solution calculated by Pagano [44] and the results of a refined finite element model created in LMS Samtech Samcef®. The Samcef model can be seen as a longitudinal section of the beam, in which the thickness is modelled explicitly to capture that zigzag behaviour foreseen by the elasticity theory.
The Pagano problem is that of a simply-supported beam subject to a sinusoidally distributed load (Fig. 2.2).

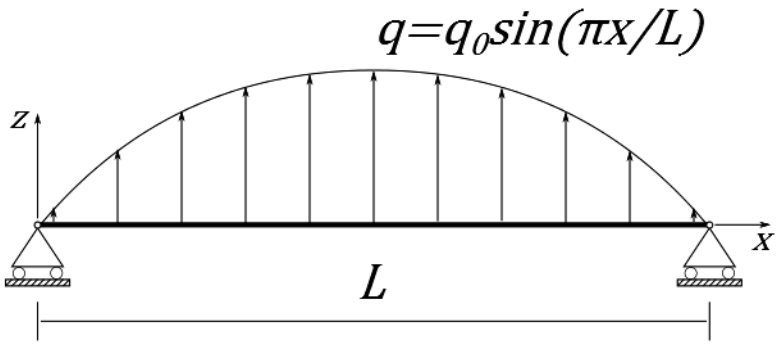

Fig. 2.2. The Pagano problem

Several test cases have been identified in the literature [72, 96–98]. The most relevant results are reported below. Small aspect ratios have been considered only to maximise

the influence of shearing. Tables 2.1-2.2 summarise material properties and layups respectively.

Material	E_1 [GPa]	E_2 [GPa]	G_{13} [GPa]	G_{23} [GPa]
m_1	25	1	0.5	0.2
m_2	73	–	29.2	–
m_3	21.9	–	8.76	–
m_4	32.57	1	8.21	3.28
$soft_1$	0.73	–	0.292	–
$soft_2$	3.65	–	1.46	–
$soft_3$	0.073	–	0.029	–

Table 2.1. Material properties

	Layup	**Thickness** (h_k/h)	**Material**
Test 1	(0/90/0)	$(0.333)_3$	$(m_1)_3$
Test 2	(0/soft/0)	(0.2/1.6/0.2)	$(m_2/soft_3/m_2)$
Test 3	$(0/90/0_3/90/0)$	$(0.0333_3/0.8/0.0333_3)$	$(m_1/m_1 10^{-5}/m_1)$
Test 4	$(0/90/0_2/90)$	(0.6/0.4/0.3/0.5/0.2)	$((m_1)_3/m_4/m_1)$
Test 5	(soft/0/soft)	$(0.66)_3$	$(soft_1/m_2/soft_2)$

Table 2.2. Beams' layup

The mid-span deflection and axial displacement at the top and bottom surfaces at $x = L$ have been compared. In particular, all the displacements are reported in non-dimensional forms according to Eqs. 2.33

$$\overline{\mathbf{w}} = \frac{100bE_1h^3w}{q_0L^4}; \quad \overline{\mathbf{u}} = \frac{E_1bu}{q_0h}; \qquad \text{for test 1} \tag{2.31}$$

$$\overline{\mathbf{w}} = \frac{\pi^4 D_{11}w}{100q_0L^4}; \quad \overline{\mathbf{u}} = \frac{\pi^4 D_{11}w}{100q_0L^4}; \quad \text{for tests 2,5} \tag{2.32}$$

$$\overline{\mathbf{w}} = \frac{100bE_2h^3w}{q_0L^4}; \quad \overline{\mathbf{u}} = \frac{E_2bh^2u}{q_0h}; \quad \text{for tests 3,4} \tag{2.33}$$

with

b = beam width; h = beam height; L = beam length; u = axial displacement; w = transverse displacement; E_1 = longitudinal modulus; E_2 = transverse modulus; D_{11} = corresponding element in the bending stiffness matrix.

The displacements are compared to the Pagano solution and when not available to the refined Samcef model. The percentage error is then calculated as:

$$E_{\%} = \frac{\text{Reference solution} - \text{Current solution}}{\text{Reference solution}} \cdot 100 \tag{2.34}$$

For each test, a table, gathering all the results, and the axial displacements plots are presented.

Test 1

Test 1 considers a 3-layer cross-ply beam with uniform layer thickness. For the MATLAB beam, 200 elements are used; in the refined Samcef finite element model 200 elements are chosen along the length and 14 in the thickness direction to model each layer. Table 2.3 shows the deflection and the axial displacement for each model.

Test 1	$\overline{\mathbf{w}}$	$\mathbf{E}_{\%}$	$\overline{\mathbf{u}}_{x,upper}$	$\mathbf{E}_{\%}$
		L/h=4		
Pagano	2.70	–	0.921	–
FEM (Samcef)	2.61	3.3	0.9566	-3.86
FSDT	2.41	10.7	0.5126	44.3
FSDT + RZT	-2.80	3.7	0.825	10.4
FSDT + MZM	-2.80	3.7	0.023	97.5
KTSDT	3.37	-24.8	1.1855	-28.7
KTSDT + RZT	3.92	-45.2	1.3920	-51.4
KTSDT+MZM	5.43	-101.1	0.476	48.31

Table 2.3. Test 1: 3-layer cross-ply beam

These results are completed by Fig. 2.3, which displays the actual distribution of the axial displacement in the thickness direction. From both the table and the plots it is clear that not only does the RZT correctly predicts the absolute value for the displacement, but it also correctly reproduces the distribution of the axial displacement in the thickness direction. If we compare its results with the MZM, we observe that the latter is still able to predict the deflection up to the same accuracy of the RZT but then it totally fails to capture the axial displacement distribution.

When we look at the KTSDT-based models, we notice that third order approximation are not capable at all to capture the real behaviour of the structure. A closer look shows that adding the RZT actually enables us to reconstruct the correct distribution

but scaled. The addition of the MZM on the other hand gives abrupt variation of slopes at layers' interface.

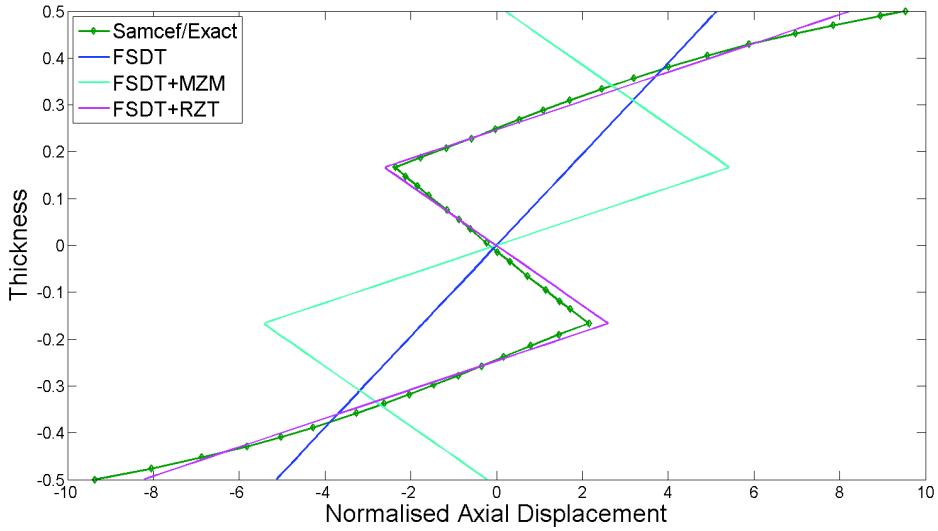

(a) FSDT and Zigzag functions

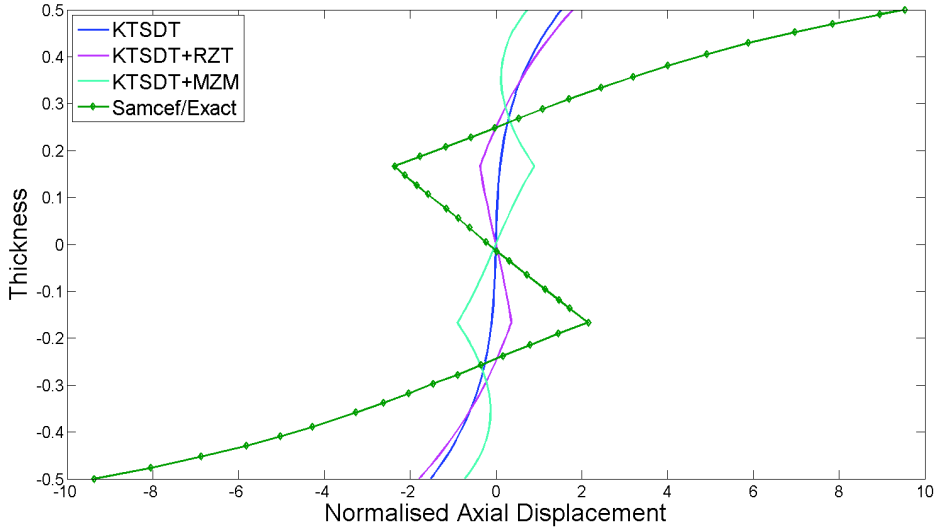

(b) KTSDT and Zigzag functions

Fig. 2.3. Test 1: Axial displacements

Test 2

Test 2 considers a traditional sandwich structure with two thin face sheets and a thick soft core. As for the previous case, 200 elements have been selected for the MATLAB beam model and along the length of the refined Samcef model, while 36 elements are chosen to model the thickness of the refined Samcef model. Table 2.4 and Fig. 2.4 describe the results. The same trend shown for Test 1 is recognisable for Test 2 as well. In this case, however, the zigzag effect is enhanced by the significant mismatch

of properties between face sheets and the core and the different layers' thickness. The importance of considering both geometry and layer's properties is highlighted by the FSDT+MZM curve which overpredicts the slope in all layers. The KTSDT, alone or enriched by the Zigzag functions, gives again inconsistent and unrealistic results.

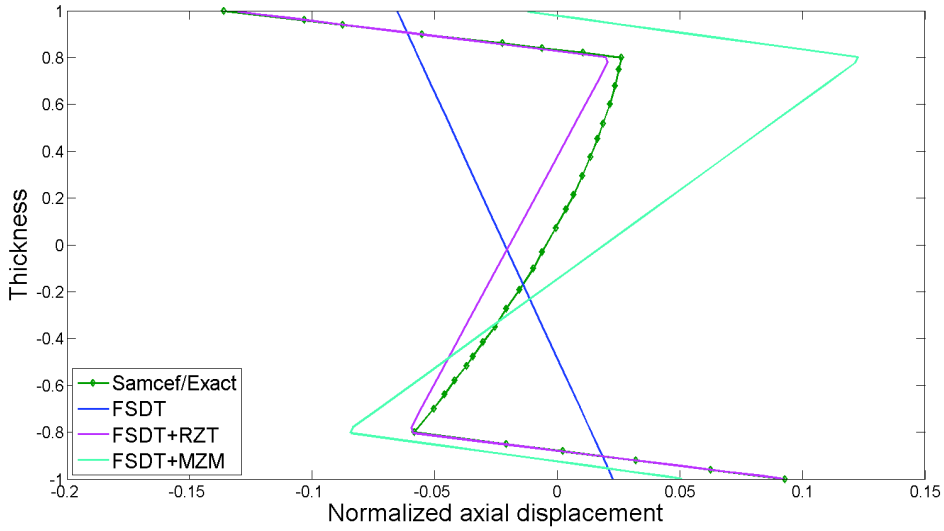

(a) FSDT and Zigzag functions

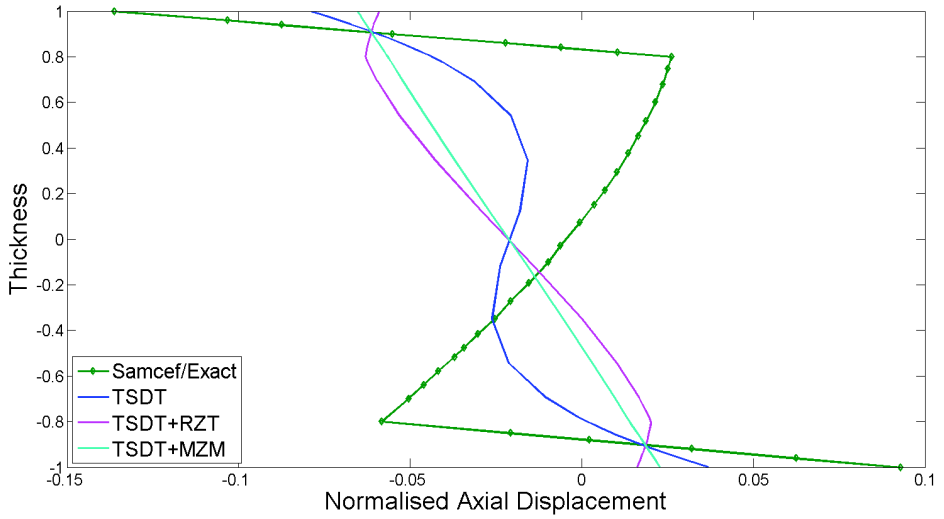

(b) KTSDT and Zigzag functions

Fig. 2.4. Test 2: Axial displacements

Test 2	$\overline{\mathbf{w}}$	$\mathbf{E}_{\%}$	$\overline{\mathbf{u}}_{x,lower}$	$\mathbf{E}_{\%}$	$\overline{\mathbf{u}}_{x,upper}$	$\mathbf{E}_{\%}$
			L/h=5			
Pagano	2.435	–	-0.130	–	0.092	–
FEM (Samcef)	2.45	-4.5	-0.13	0	0.092	0
FSDT	0.1641	93.6	-0.022	83.7	0.065	29.3
FSDT + RZT	2.46	-1.0	-0.13	0	0.092	0
FSDT + MZM	2.46	-1.0	-0.012	90	0.050	45.6
KTSDT	0.5851	75.8	-0.078	40	0.036	60.8
KTSDT + RZT	0.0214	99.1	-0.059	54.6	0.016	82.6
KTSDT+MZM	0.1334	94.5	-0.064	50.7	0.022	76.1

Table 2.4. Test 2: 3-layer sandwich beam

Test 3

Test 3 considers a sandwich beam with laminated cross-ply face sheets. Face sheets are very thin compared to the core. The beam model is made up of 200 elements; the refined model has 200 elements along the length and 120 along the thickness. Table 2.5 shows the numerical results. Fig. 2.5a shows an interesting phenomenon: the combination of ply thickness and material properties results in negligible zigzag effect in the face sheets region. The RZT is able to predict such behaviour while the MZM forces anyway the variation in slope (Fig. 2.5b).

Test 3	$\overline{\mathbf{w}}$	$\mathbf{E}_{\%}$	$\overline{\mathbf{u}}_{x,lower}$	$\mathbf{E}_{\%}$
		L/h=8		
Pagano	–	–	-0.398	–
FEM (Samcef)	131.64	–	-0.391	1.75
FSDT	1.74	98.67	-0.0234	94.97
FSDT + RZT	131.00	0.48	-0.407	-0.50
FSDT + MZM	2.54	98.07	-0.018	94.97
KTSDT	1.89	98.56	-0.02	94.97
KTSDT + RZT	1.68	98.72	-0.025	93.71
KTSDT+MZM	1.94	98.52	-0.023	94.22

Table 2.5. Test 3: 7-layer cross-ply beam with soft core

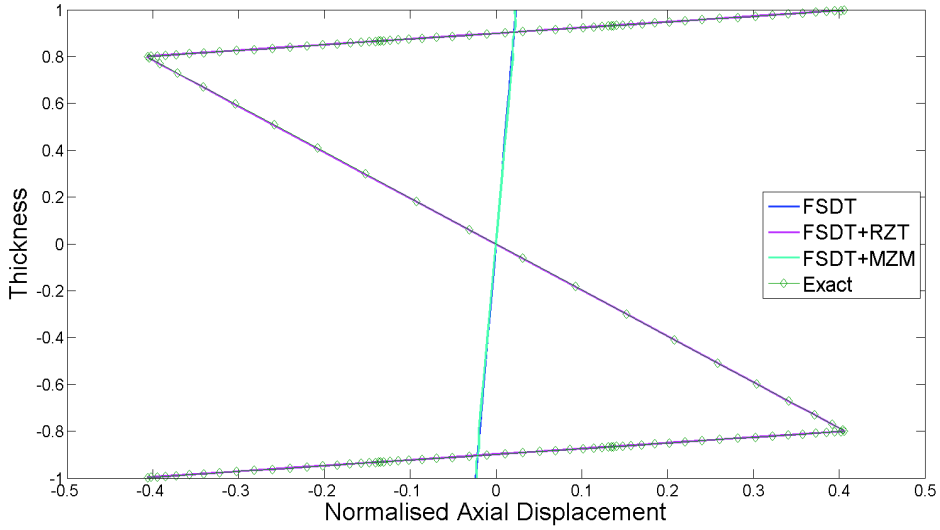

(a) FSDT and Zigzag functions

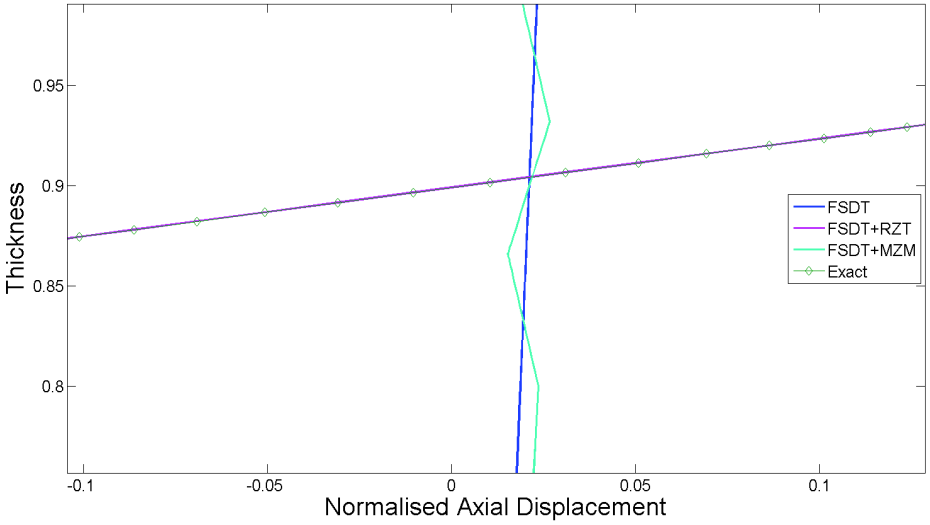

(b) FSDT and Zigzag functions - Close up in the face sheet region

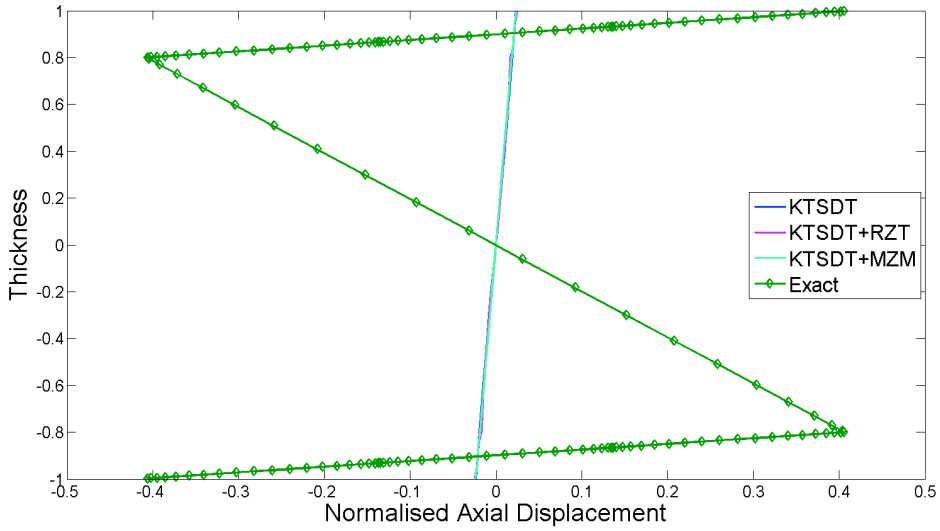

(c) KTSDT and Zigzag functions with exact solution

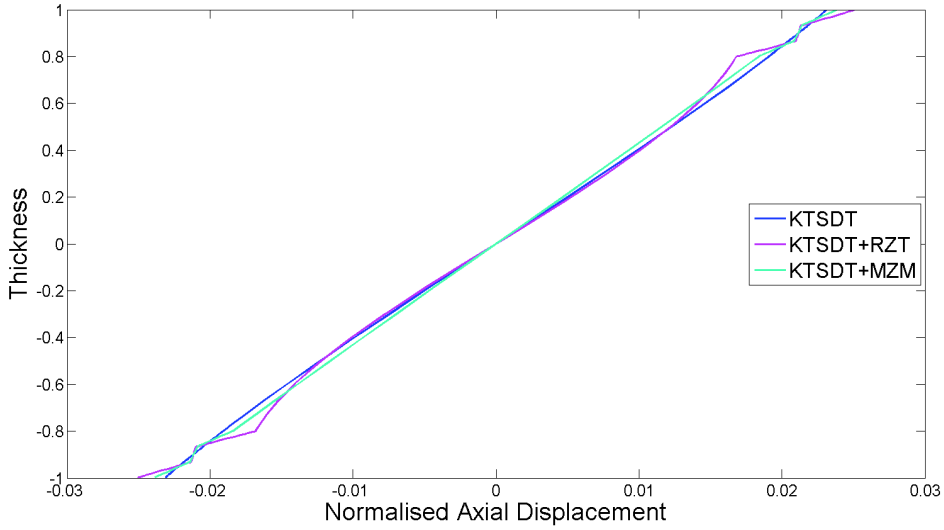

(d) KTSDT and Zigzag functions without exact solution

Fig. 2.5. Test 3: Axial displacements

On the other hand, when the zigzag functions are superposed to the KTSDT (Fig. 2.5d), they both predict a variation in slope even in the face sheets area, which proves again the inconsistent outcomes of this approach. Comparison with the exact solution eventually confirms it (Fig. 2.5c).

Test 4

This particular case falls into the category of laminate with *External Weak Layer* (EWL). The EWL has been studied by Gherlone in [98]. As Fig. 2.6 shows, the elasticity theory in this case predicts no change in slope, due to the fact that the weak layer's deformation will be driven by that of the stiff layer adjacent to it.

The Zigzag theories are not able to automatically reproduce this effect; however, the RZT compared to the MZM can actually be modified by imposing a logical condition on the continuity of the slope for the top (or bottom) layer. In particular, Gherlone [98] imposes the following conditions:

a) if $G_{xz}^{(1)} \leq G_{xz}^{(2)}$, then $G_{xz}^{(1)} = G_{xz}^{(2)}$;

b) if $G_{xz}^{(N)} \leq G_{xz}^{(N-1)}$, then $G_{xz}^{(N)} = G_{xz}^{(N-1)}$.

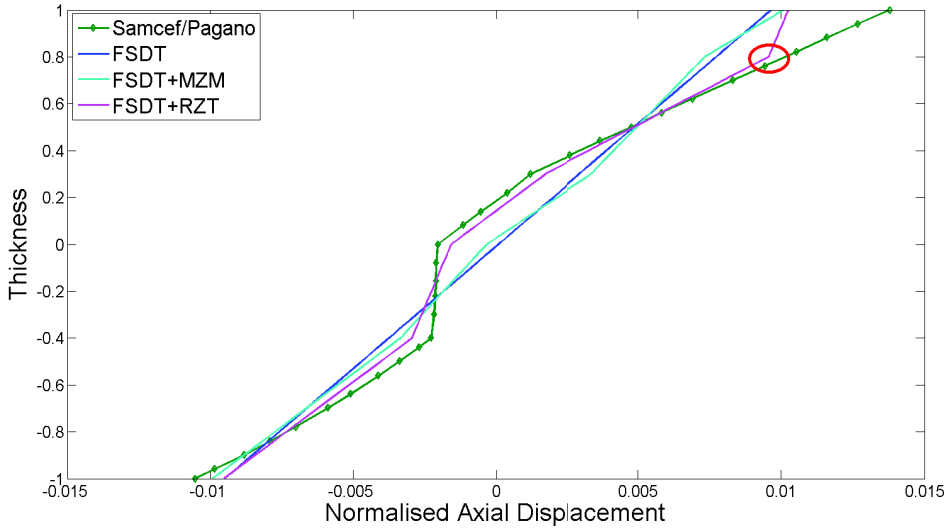

Fig. 2.6. Test 4: FSDT and zigzag functions, axial displacement

Test 4	$\overline{\mathbf{w}}$	$\mathbf{E}_{\%}$	$\overline{\mathbf{u}}_{x,lower}$	$\mathbf{E}_{\%}$	$\overline{\mathbf{u}}_{x,upper}$	$\mathbf{E}_{\%}$
			L/h=8			
Pagano	1.2	–	-0.01	–	0.014	–
FEM (Samcef)	1.15	4.17	-0.01	0	0.0138	1.43
FSDT	0.6773	43.56	-0.0095	5.0	0.0097	30.71
FSDT + RZT	1.0181	15.16	-0.0095	5.0	0.0103	26.43
FSDT + MZM	0.7591	36.74	0.0101	201.00	0.0103	173.57
KTSDT	0.7191	40.08	-0.0101	-1.0	0.0104	25.71
KTSDT + RZT	0.3065	74.46	-0.0078	22.0	0.0070	50.0
KTSDT+MZM	0.4978	54.68	-0.0078	22.0	0.0077	45.0

Table 2.6. Test 4: 5-layer beam with EWL

However, these logical conditions impact on the value of the homogenised modulus, as in Eq. 1.45, since it does not take into account the actual transverse modulus of the top or bottom layer. Therefore, a modification is proposed in the present study, where the continuity condition is rather imposed on the slope so that homogenised modulus is correctly calculated considering the correct value of the transverse modulus of each layer. Conditions a) and b) take the form:

a) if $G_{xz}^{(1)} \leq G_{xz}^{(2)}$, then $\beta^{(1)} = \beta^{(2)}$;

b) if $G_{xz}^{(N)} \leq G_{xz}^{(N-1)}$, then $\beta^{(N)} = \beta^{(N-1)}$.

The modified model leads to the following results:

Test 4	$\overline{\mathbf{w}}$	$\mathbf{E}_{\%}$	$\overline{\mathbf{u}}_{x,lower}$	$\mathbf{E}_{\%}$	$\overline{\mathbf{u}}_{x,upper}$	$\mathbf{E}_{\%}$
			L/h=8			
Pagano	1.2	–	-0.01	–	0.014	–
FEM (Samcef)	1.15	4.17	-0.01	0	0.0138	1.43
FSDT + RZT	0.6773	43.56	-0.0095	5.0	0.0097	30.71
FSDT + RZT Modified	1.158	3.50	-0.00975	5.0	0.01385	1.07

Table 2.7. Test 4: 5-layer beam with EWL - Modified Zigzag function

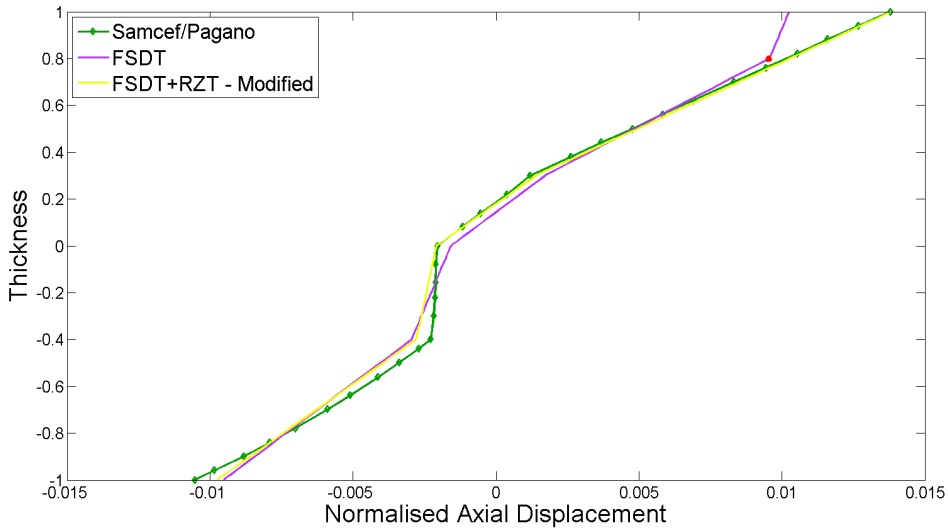

Fig. 2.7. Test 4: Modified FSDT+RZT, axial displacement

Finally, the KTSDT's results are shown in Fig.2.8.

Test 5

An extreme case of the EWL effect is presented below: a soft layer is applied on the top and bottom surface of a stiff layer. In such a configuration it will be the stiff layer to determine the deformation of the entire laminate so that, despite the difference in transverse stiffness between the layers, no Zigzag effect takes place and the beam behaves as a standard homogeneous beam. The exact solution coincides with the FSDT one (Fig. 2.9).

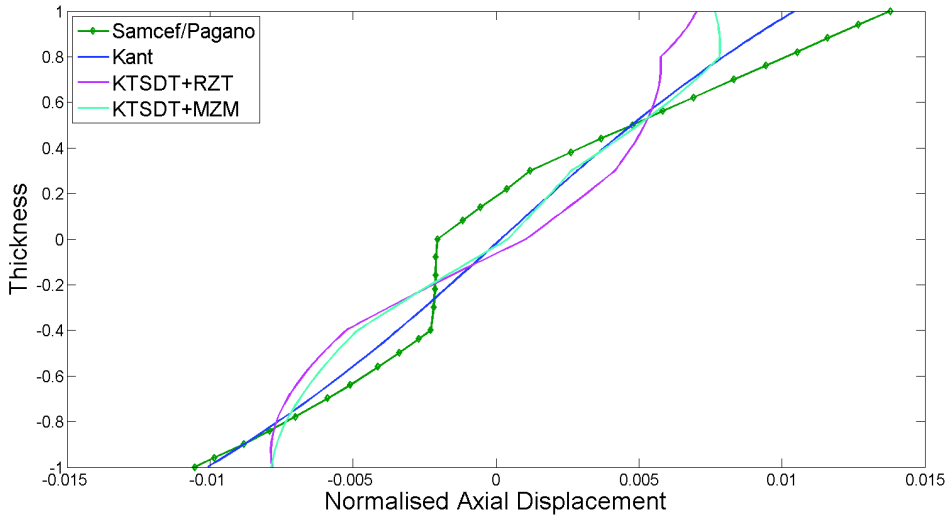

Fig. 2.8. Test 4: KTSDT and zigzag theories, axial displacement

Test 5	$\overline{\mathbf{w}}$	$\mathbf{E}_{\%}$	$\overline{\mathbf{u}}_{x,lower}$	$\mathbf{E}_{\%}$	$\overline{\mathbf{u}}_{x,upper}$	$\mathbf{E}_{\%}$
			L/h=5			
Pagano	0.1028	–	-0.030	–	0.0305	–
FEM (Samcef)	0.1044	-1.55	-0.0319	-6.3	0.0305	0
FSDT	0.1029	-0.09	-0.0325	-8.3	0.0309	-1.3
FSDT + RZT	0.1030	-0.19	-0.0310	-3.3	0.0308	-0.9
FSDT + MZM	0.1034	-0.58	-0.0321	-4	0.0305	0
KTSDT	0.1027	-0.09	-0.0322	-7.3	0.0307	0.6
KTSDT + RZT	0.1027	-0.09	-0.0325	-8.3	0.0305	0
KTSDT+MZM	0.1015	1.26	-0.03072	-0.8	0.02911	2.9

Table 2.8. Test 5: 3-layer beam with stiff core and soft outer layers

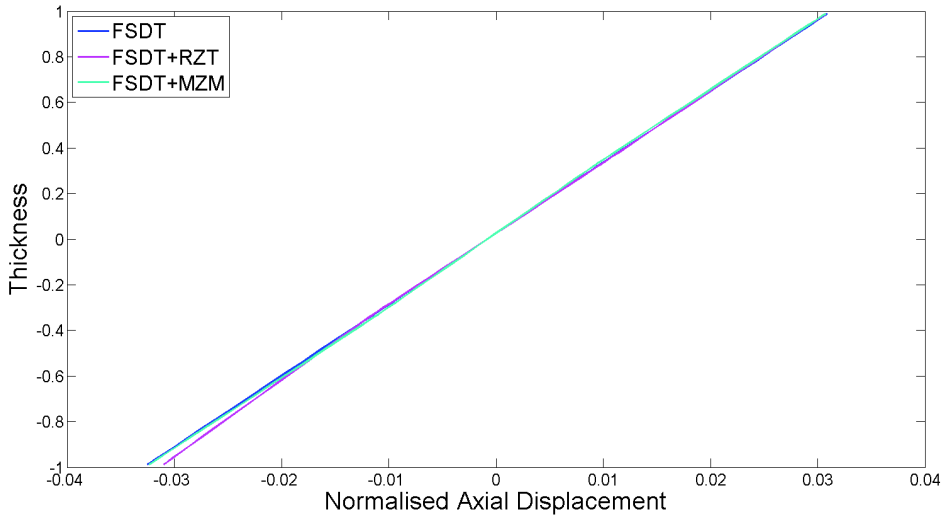

(a) FSDT and zigzag functions

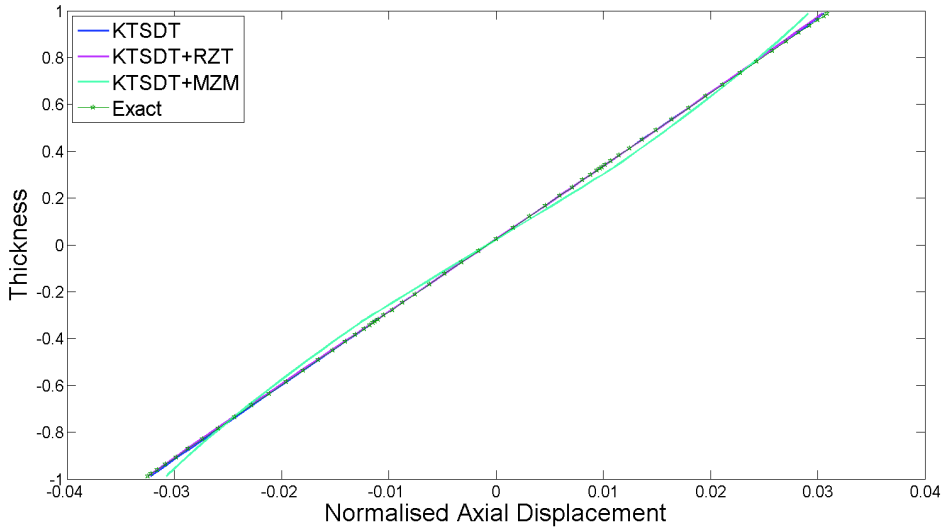

(b) KTSDT and zigzag functions

Fig. 2.9. Test 5: axial displacements

2.4 Conclusions

The results shown so far can be summarised as follows:

- the RZT proved superior to the MZM; in particular, considering both material properties and geometry in the definition of the zigzag function leads to consistency in results for all types of lamination schemes considered. However, this is not surprising as Murakami warned about the possible inaccuracy of his function whenever periodicity was not present.

- Comparison of the zigzag approach to higher order approximation reveals some limitations regarding the latter. If on the one hand it is true that a third order approximation naturally leads to parabolic transverse shear stresses, on the other there is no clear evidence that axial displacements are distributed in a cubic fashion; the mathematical consistency of the theory is not directly linked to the physical phenomena and the limitation of this approach can be seen in the significant discrepancies with the elasticity solution, as shown in the previous paragraph.
- The addition of the zigzag function to the FSDT generally brings improved results; the addition of the zigzag theory to higher order theories shows that this is true only if the base theory is consistent with the physics of the beams' deformation. Results actually show that, irrespective of the zigzag function used, its combination with the KTSDT leads to unpredictable results.

Based on these preliminary conclusions, only the study of the RZT will be pursued in the dynamic domain and for further extension of the finite element model for plates and shells.

Chapter 3

Dynamic analysis of multilayered beams

3.1 The equations of motion

Most engineering structures are subject to loadings that vary with time and it is therefore essential to know the time-varying pattern of their response to ensure their integrity, reduce discomfort caused by vibrations and associated aural phenomena. The study of vibrations is a specific area of dynamics, which analyses the motion of physical systems and structures. Vibrations can be defined as the oscillation of a body with respect to a reference state, usually the static equilibrium [99]. The motion is caused by an external disturbance which removes the system from its reference state; other effects influencing a vibrating system are: the elastic forces which try to restore the equilibrium state; the inertial forces which will affect the interaction between the external disturbance and the elastic forces; the momentum associated with the accelerations of the system; dissipative phenomena such as internal friction, friction at joints which oppose the system's movement. At any instant t the configuration of the system will be defined by its *generalised coordinates*, which are the independent parameters (displacements or rotations) that define the actual state of the system with respect to its reference configuration. The number of generalised coordinates represents the degrees of freedom of the system.
To determine the governing equations of a vibrating system several approaches are available [100], which all lead to a set of differential equations referred to as *equations of motion* (EoM). The EoM are a system characteristic and their form is independent of the method used to derive them. As an example consider the system in Fig. 3.1.

Newton's second law of motion. Application of the Newton's second law of motion (NSL), which states that the force acting on a mass is equal to its rate of change of

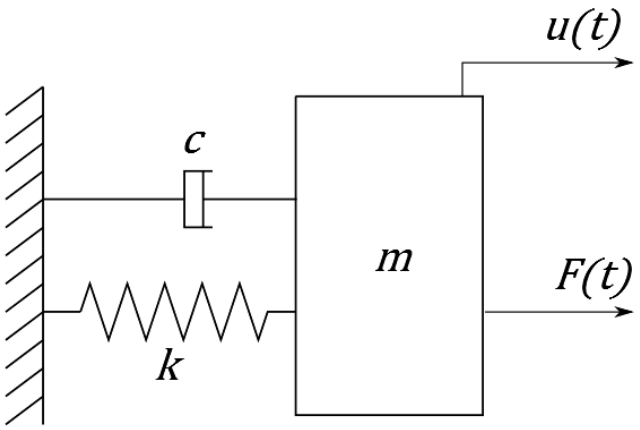

Fig. 3.1. 1 DOF Mass-Spring-Damper System

momentum, enables us to write the equation of dynamic equilibrium. The forces that act on the mass are: the external force $F(t)$, the elastic force $F_{el}(t) = ku(t)$, the viscous force exerted by the damper $F_{visc}(t) = c\dot{u}(t)$ and the inertial force $F_{in}(t) = m\ddot{u}(t)$. The elastic, viscous and inertial forces all oppose the motion of the mass m, being $u(t)$ the displacement of the mass. The equilibrium equation takes the form:

$$m\ddot{u} + c\dot{u} + ku = F \tag{3.1}$$

The application of the NSL is straightforward and can be easily extended to multi-degree of freedom systems (multi-DoF): the equilibrium equation is found for each mass in the system and the resulting equation can be expressed in compact matrix form as:

$$[M]\{\ddot{u}\} + [C]\{\dot{u}\} + [K]\{u\} = \{F\} \tag{3.2}$$

where $[M]$ is the mass matrix, $[C]$ is the damping matrix and $[K]$ is the stiffness matrix. The analysis of the system in Fig. 3.2 will highlight some important properties of the matrices involved.

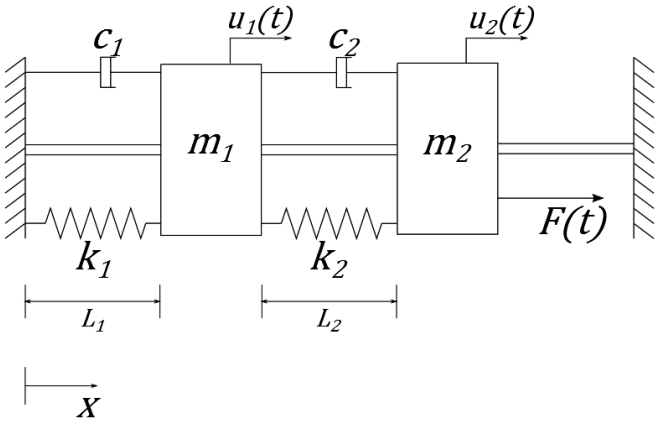

Fig. 3.2. 2 DOF system

Let l_1 and l_2 be the undeformed lengths of the springs; their elongations are defined as $\Delta_1 = L_1 + u_1 - l_1$ and $\Delta_2 = L_2 + u_2 - u_1 - l_2$ respectively; the elongation rates are therefore $\dot{\Delta_1} = \dot{u_1}$ and $\dot{\Delta_2} = \dot{u_2} - \dot{u_1}$. The equilibrium equations for the two bodies in the x direction are

$$\begin{aligned} \sum F_x^1 &= -k_1\Delta_1 - c_1\dot{\Delta_1} + k_2\Delta_2 + c_2\dot{\Delta_2} = m_1\ddot{u}_1; \\ \sum F_x^2 &= F - k_2\Delta_2 - c_2\dot{\Delta_2} = m\ddot{u}_2 \end{aligned} \tag{3.3}$$

Rearranging and grouping in matrix form all mass, stiffness and damping terms we eventually find:

$$\begin{bmatrix} m_1 & 0 \\ 0 & m_2 \end{bmatrix} \begin{Bmatrix} \ddot{u}_1 \\ \ddot{u}_2 \end{Bmatrix} + \begin{bmatrix} (c_1 + c_2) & -c_2 \\ -c_2 & c_2 \end{bmatrix} \begin{Bmatrix} \dot{u}_1 \\ \dot{u}_2 \end{Bmatrix} + \begin{bmatrix} (k_1 + k_2) & -k_2 \\ -k_2 & k_2 \end{bmatrix} \begin{Bmatrix} u_1 \\ u_2 \end{Bmatrix} = \begin{Bmatrix} 0 \\ F \end{Bmatrix} \tag{3.4}$$

In general, the mass matrix is diagonal; if this is not the case then the system is *inertially coupled*; the stiffness matrix is not diagonal but symmetric; the damping matrix deserves an independent discussion which will be dealt with in a later section.

Principle of Virtual Displacement. When more complex systems are to be analysed energy methods are more convenient. An example is the Principle of Virtual Displacement (PVD). Consider a system in equilibrium under a set of forces; if a virtual displacement δu is applied to it then the work done by the forces is zero. Application of the principle to the 1 DOF system of Fig. 3.1 leads to:

$$-m\ddot{u}\delta u - c\dot{u}\delta u - ku\delta u + F\delta u = 0; \tag{3.5}$$

$$\delta u\left(-m\ddot{u} - c\dot{u} - ku + F\right) = 0; \tag{3.6}$$

Since δu is arbitrary and non-zero, Eq. 3.6 is satisfied only if

$$m\ddot{u} + c\dot{u} + ku = F \tag{3.7}$$

which is equal to the equation found by the application of Newton's second law.

Hamilton's Principle. The PVD still requires the calculation of the work, i.e. the scalar product of forces and displacements vectors, which can become lengthy for multi-DoF systems. We can avoid this process applying the Hamilton's Principle which expresses the dynamics of a system in variational form. Mathematically it takes the form:

$$\int_{t_1}^{t_2} \left(\delta\left(T - U\right) + \delta W_{nc}\right) dt = 0 \tag{3.8}$$

where:
$T = \frac{1}{2}m\dot{u}$ is the kinetic energy;
$U = \frac{1}{2}ku^2$ is the elastic potential energy;
δW_{nc} is the work done by the non-conservative forces.
If we apply Eq. 3.8 to the sample 1 DOF system we obtain:

$$T = \frac{1}{2}m\dot{u}, \quad U = \frac{1}{2}ku^2, \quad \delta W_{nc} = F\delta u - c\dot{u}\delta u;$$

Introducing the above expression in Eq. 3.8 and integrating we find again Eq. 3.1.

The above mentioned methods are easily applicable for discrete systems for which the number of DoF is a finite number. Continuous systems on the other hand are regarded to have an infinite number of DoFs as the displacement field will be not only a function of time but also a function of the position within the continuum. The Hamilton's principle can be extended to continuous systems taking the form of the Rayleigh-Ritz Method and the finite element method.

The Rayleigh-Ritz Method. Using the Hamilton's Principle, the continuous displacement field $u(x,t)$ for the mono-dimensional case is found and later approximated by a finite expansion:

$$u^n(x,t) = \sum_{j=1}^{n} \phi_j(x) q_j^n(t) \tag{3.9}$$

where $\phi_j(x)$ are linearly independent function of x, which must satisfy the geometric boundary conditions, and $q_j^n(t)$ are unknown functions of time. The number of terms in the expansion, n, now represents the finite number of DoF to which the original continuous solution has been approximated. The equations of motion is written in matrix form as:

$$[M]\{\ddot{q^n}\} + [K]\{\dot{q^n}\} = \{Q^n\} \tag{3.10}$$

The mass and stiffness matrix are derived by substituting the displacement approximation in the kinetic and potential energy expression respectively. For the simple case of a rod of length L loaded by a force $F(t)$ at $x = L$ this process leads to:

$$M_{jk} = \int_0^L \rho A \phi_j(x)\phi_k(x)dx; \quad K_{jk} = \int_0^L EA\phi_j(x)\phi_k(x)dx \tag{3.11}$$

The vector $\{Q^n\}$ is the vector of generalised force given by:

$$Q_j^n = \phi_j(L)F(t). \tag{3.12}$$

The dissipative effects are included in the non-dissipative work expression (Eq.3.8). The Rayleigh-Ritz method can be of difficult application when more complex structures are analysed because it becomes difficult to find the functions which satisfy the geometric boundary conditions. This is where the finite element method comes into play.

The Finite Element Method (FEM). The basic principles of the FEM have been explained in the previous chapter and no substantial differences are found in the dynamic analysis. With respect to the Rayleigh-Ritz method, the set of functions used to approximate the displacement field coincides with the shape functions of the elements chosen to approximate the structure. This makes the procedure quite simple even for complex systems. In a later paragraph the mass matrix construction process for the RZT beam will be explained in details.

The EoM are essential to solve vibration problems which are often divided in the analysis of *free vibrations* and *forced vibrations*.

3.1.1 Free vibrations of undamped and damped systems

In free vibration analysis we observe a system that is free to oscillate after being removed from its reference equilibrium state. Observation is made after the disturbance has been applied; it is normally accounted for in the definition of initial conditions such as initial displacement or velocity. The type of motion is harmonic, with constant amplitude if no dissipative phenomena take place, or decaying if damping is present. The parameters that a free vibration analysis allows us to determine are the vibration frequencies of the system, *natural frequencies*, the pattern of vibration, *mode shape*, and the dissipation magnitude, *damping factors* [101]. They can be found both analytically, or numerically, by solving the equations of motion. As an example, consider again the system in Fig. 3.1. In the first place we can assume that actually the dashpot constant c is zero so that no decay in the response will occur. We impose also that the force is zero, $F(t) = 0$. Finally, the motion $u(t)$ of the mass m will be harmonic, $u(t) = Asin(\omega t - \phi) = \Re\left[Ae^{i\omega t - \phi}\right]$, where $\omega t - \phi$ is the phase. In such conditions, Eq. 3.1 becomes

$$m\ddot{u} + ku = 0 \tag{3.13}$$

which is a homogeneous linear differential equation. To solve it, we seek the solution of the characteristic equation:

$$m\lambda^2 + k = 0 \Longrightarrow \lambda_{1,2} = \pm\sqrt{\frac{k}{m}} = \pm i\omega_n \tag{3.14}$$

where $\omega_n \overset{\text{def}}{=}$ *natural frequency of the system.* The motion of the system will therefore evolve with time according to

$$u(t) = \Re\left[Ae^{i\omega_n t - \phi)}\right] \tag{3.15}$$

In multi-DoF systems the differential equation is in matrix form and we assume as a trial solution the harmonic function $\{u\} = \Re\left[B\{\Phi\}e^{i\omega t}\right]$, so that the characteristic equation becomes

$$\left[[K] - \omega^2 [M]\right] \{\Phi\} = 0 \tag{3.16}$$

We exclude the solution $\{\Phi\} = 0$ as it will imply that the displacements are zero and no vibration actually occurs. Eq. 3.16 is a matrix *eigenvalue problem* and

$$\left[[K] - \omega^2 [M]\right] \ = 0 \tag{3.17}$$

is its characteristic equation. Eq. 3.17 is satisfied when the matrix on the left-hand side is singular. The values ω_j^2 for which this happens are the eigenvalues, which represent the square of the natural frequencies of the system. Substitution of the eigenvalues in Eq. 3.16 allows us to find the associated *eigenvector*, the components of which define the mode shape of the structure. Mode shapes have two important properties, that of orthogonality with respect to the mass and stiffness matrices (Eq. 3.19), which make it possible, by a variable change, to decouple the equations of motion so that a system with N DoF can be solved as N uncoupled single DoF systems [102]. This process is called *modal transformation* and allows us to describe the motion of the structure in terms of modal coordinates, η_j, which are more easily handled. Eventually, the response of the structure can be written as

$$\{u\} = \sum_{j=1}^{N} \{\Phi_j\}\{\eta_j\}. \tag{3.18}$$

The above equation states that the response can be obtained as the superposition of the normal modes, the contribution of which to the global response is given by the modal coordinates η_j. Thanks to the modal transformation, the property of orthogonality takes the form:

$$\begin{aligned} &\{\Phi_l\}^T [M] \{\Phi_j\} = \delta_{lj}; \qquad \delta_{jn}\text{=Kronecker delta} \\ &\{\Phi_l\}^T [K] \{\Phi_j\} = \omega_j^2 \delta_{lj} \end{aligned} \tag{3.19}$$

where both equations have been normalised with respect to the mass.

Another important characteristic of mode shapes are *nodes*, which are points of the structure which do not undergo any displacement or rotation during the oscillation. The location of nodes is especially important in experimental modal analysis and in forced

vibration analysis. In real structures dissipative effects are always present and usually not easily accounted for unless all the dissipation is exerted by mechanical elements such as dashpots, for which damping constants can be defined. In most practical applications this is not the case and dissipation comes from multiple sources: materials' structural damping, frictions at joints, air damping etc. For a single DoF system, the equation to solve in the presence of damping is:

$$m\ddot{u} + c\dot{u} + ku = 0 \tag{3.20}$$

The dissipation will not only depend on the coefficient c but also on the mutual interaction between mass and stiffness; consequently Eq. 3.20 is usually written in terms of the *damping ratio*, ζ:

$$\ddot{u} + 2\zeta\omega_n\dot{u} + \omega_n^2 u = 0; \quad \zeta = \frac{c}{2m\omega_n} \tag{3.21}$$

The solution of the differential equation will depend on the damping ratio according to Eq. 3.22:

$$\lambda_{1,2} = -\zeta\omega_n \pm \omega_n\sqrt{\zeta^2 - 1} \tag{3.22}$$

We define the natural frequency of the damped system as

$$\omega_d = \omega_n\sqrt{\zeta^2 - 1} \tag{3.23}$$

The response of the system is then given by:

$$u(t) = B_1 e^{\lambda_1 t} + B_2 e^{\lambda_2 t} \tag{3.24}$$

In particular, three regimes can be identified:

Underdamped response

For $0 \leq \zeta < 1$ the system is said *underdamped* and the two roots $\lambda_{1,2}$ are conjugate complex. The response will be harmonic but decaying and bounded by the two decaying exponential functions (Fig. 3.3a):

$$u(t) = e^{-\zeta\omega_n t}\Re\left[Ae^{i\omega_d t}\right] = e^{-\zeta\omega_n t}A\cos(\omega_d t - \phi) \tag{3.25}$$

$$f(t) = \pm Ae^{-\zeta\omega_n t}, \quad f(t) = \text{Decaying Exponential Envelopes} \tag{3.26}$$

Overdamped response

For $\zeta > 1$ the roots $\lambda_{1,2}$ will be real and distinct so that the solution will be the sum of two real exponentials:

$$u(t) = c_1 e^{\lambda_1 t} + c_2 e^{\lambda_2 t} \tag{3.27}$$

The coefficients c_1 and c_2 depend on the condition imposed on the initial displacement and the initial velocity of the system. Unlike the underdamped system, the response will be aperiodic.

Critically damped response

For $\zeta = 1$ the system is said to be critically damped; the roots are real and coincident. Despite meaningful from the mathematical point view, this condition is hardly met in practice. The solution can be calculated in a limiting sense but, as Fig. 3.3b shows, there is little difference between a critically damped and a slightly overdamped system. By taking to the limits the underdamped and overdamped formulations, it can be however inferred that critical damping will restore the equilibrium position in the shortest time.

For multi-DoF systems, few approaches have been proposed over time to include the damping matrix in the equation of motion while taking advantage of the decoupling introduced with the modal transformation [103]. The first one relies on the assumption of *light damping*: the damping matrix $[C]$ is approximated by a diagonal matrix with respect to which the orthogonality property of mode shapes holds. This is only valid if the coefficients are small. The second approach is referred to as *proportional damping* because the damping matrix is actually expressed as a linear combination of the mass and stiffness matrices (Eq. 3.28)

$$[C] = \alpha\,[M] + \beta\,[K]\,. \tag{3.28}$$

By comparison of Eq. 3.28 and Eq. 3.21, we can write the components of $[C]$ as

$$\zeta_j = \frac{\alpha + \beta\omega_j^2}{2\omega_j} \tag{3.29}$$

3.1.2 Forced vibration of undamped and damped systems

In forced vibration analysis we are directly interested in the effect of a force applied to the system. We will consider a harmonic excitation $Q(t) = \Re\left[Fe^{i\omega t)}\right]$. In such a case the EoM is no longer homogeneous and the solution of the differential equation will be made up of two parts: the complementary and the particular solution. The particular solution is found by the *method of undetermined coefficients*, according to which the particular solution that corresponds to a harmonic excitation is also harmonic at the excitation frequency. The harmonic response in its complex form is expressed as

$$u(t) = \Re\left[Xe^{i\omega t}\right] \tag{3.30}$$

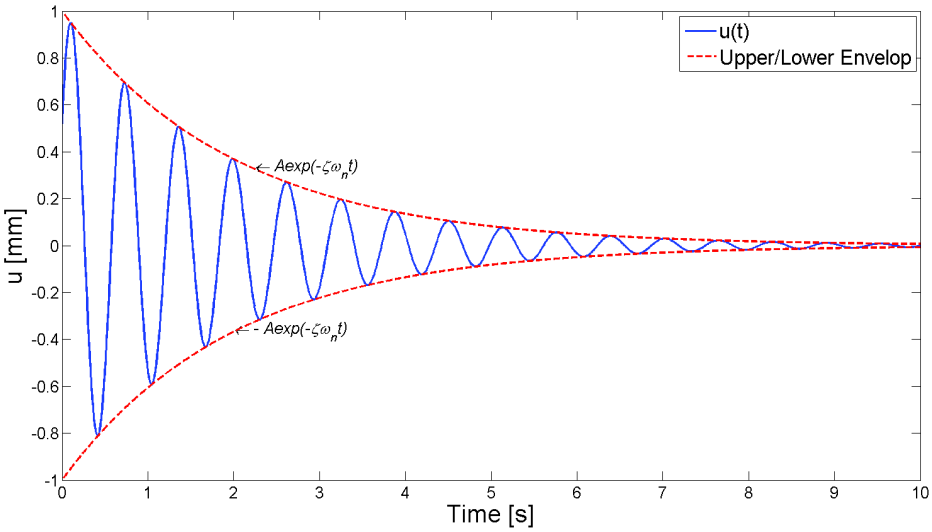

(a) Free vibration of an underdamped 1 DoF system

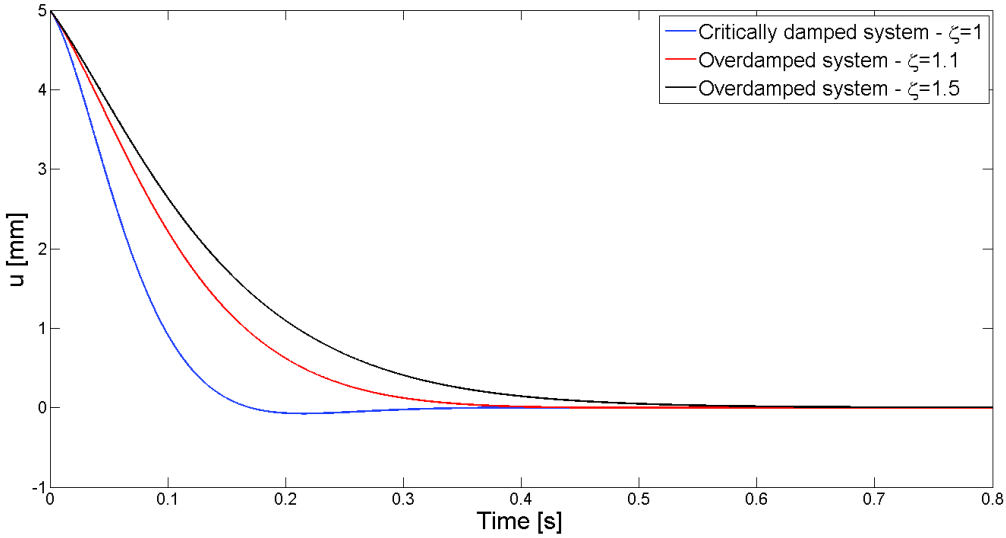

(b) Free vibration of an overdamped and critically damped 1 DoF system

Fig. 3.3. Effect of the damping ratio on the free vibration of a 1 DoF system

where X is the complex amplitude. The latter is determined by imposing that Eq. 3.30 is the particular solution of the EoM:

$$\Re\left[\left(-M\omega^2 + i\omega C + K\right) X e^{i\omega t}\right] = \Re\left[F e^{i\omega t}\right] \tag{3.31}$$

The equation must be satisfied at every time instant t; we therefore equal the terms in brackets which eventually leads to:

$$X = \frac{F}{K + i\omega C - M\omega^2} \tag{3.32}$$

The denominator is usually referred to as dynamic stiffness. Using the definition of natural frequencies and damping ratio given in Eq. 3.14 and Eq. 3.21 respectively, the following equalities hold:

$$M = \frac{K}{\omega_n^2}; \tag{3.33}$$

$$C = 2\zeta\omega_n M = \frac{2\zeta K}{\omega_n}; \tag{3.34}$$

which allow us to rewrite Eq. 3.32 in a more compact form as:

$$X = D\left(\frac{\omega}{\omega_n}, \zeta\right)\frac{F}{K} \quad \text{where } D\left(\frac{\omega}{\omega_n}, \zeta\right) = \frac{1}{1 + 2i\zeta\frac{\omega}{\omega_n} - \left(\frac{\omega}{\omega_n}\right)^2}. \tag{3.35}$$

$D\left(\frac{\omega}{\omega_n}, \zeta\right)$ is referred to as *Complex Frequency Response Function*. The amplitude and phase of the Complex Frequency Response Function can be analysed separately and plot against the frequency ratio $\frac{\omega}{\omega_n}$ giving important information on the system's behaviour. In Fig. 3.4a we observe that for ω which tends to zero, the dynamic response tends to 1 and the phase tends to zero (Fig. 3.4b) which are the same results we would obtain if the force was statically applied. We can therefore interpret the amplitude of the Complex Frequency Response as a *magnification factor* by which the response is amplified due to the dynamics of the system; the phase represents the lag of the response with respect to the excitation.

In absence of damping, $\zeta = 0$, we observe a discontinuity for $\frac{\omega}{\omega_n} = 1$, that is when the excitation frequency matches the natural frequency of the system. This condition is referred to as *resonance*. In real structures, however, sources of damping are always present, so that their response will actually never show such a discontinuity; for positive values of the damping ratio the response will rather show a maximum when the excitation frequency is equal to

$$\omega = \omega_n\sqrt{1 - 2\zeta^2}. \tag{3.36}$$

It is common practice to refer to it as the resonance of the system. As the value of ζ increases the peak decreases and it moves to the left in accordance with Eq. 3.23; the value and the position of the peak are obtained by studying the first order derivative of Eq. 3.35 which allows to define the critical values of damping ratio, $\zeta = 0.707$, above which the response will be monotonically decaying. The effect on the phase is that of introducing a lag (cf. Eq. 3.31) with respect to the excitation. As Fig. 3.4b shows, the higher the damping the lower the phase difference in the all frequency range.

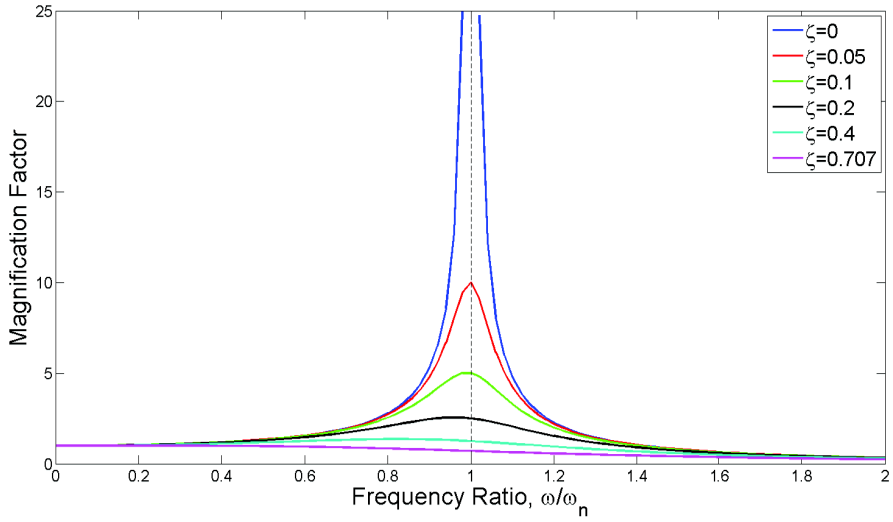

(a) Magnification factor of the harmonic response as a function of the excitation frequency

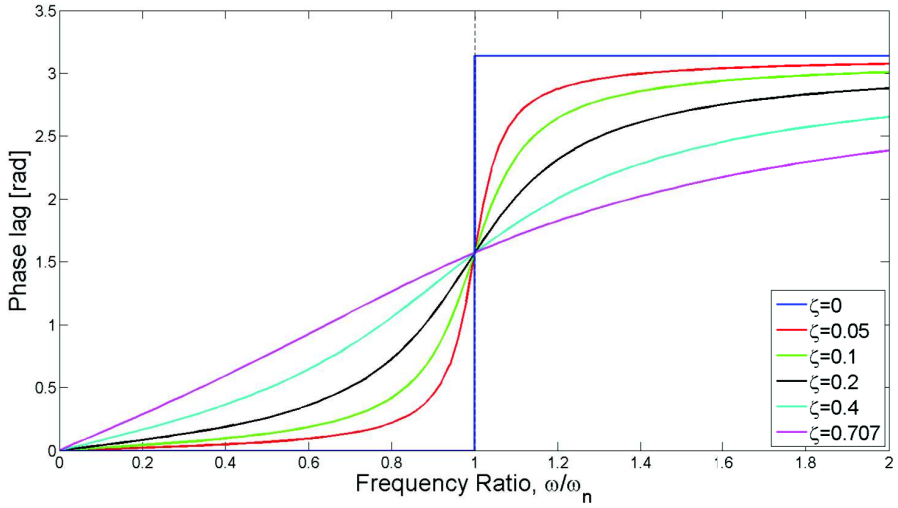

(b) Phase lag of the harmonic response as a function of the excitation frequency

Fig. 3.4. Harmonic response of a 1 DoF system

In multi-DoF systems the harmonic excitation and the corresponding harmonic response are represented by the vectors:

$$\{Q\} = \Re\left[\{F\}e^{i\omega t}\right]; \tag{3.37}$$

$$\{u\} = \Re\left[\{X\}e^{i\omega t}\right]; \tag{3.38}$$

which substituted in the EoM lead to:

$$\Re\left[[K] + i\omega\,[C] - \omega^2\,[M]\,\{X\}e^{i\omega t}\right] = \Re\left[\{F\}e^{i\omega t}\right]. \tag{3.39}$$

The response vector $\{X\}$ is given by:

$$\{X\} = \left[[K] + i\omega\,[C] - \omega^2\,[M]\right]^{-1}\{F\} \tag{3.40}$$

The term $\left[[K] + i\omega\,[C] - \omega^2\,[M]\right]^{-1}$ is referred to as the *Transfer Function* and it is defined as

$$[G(\omega)] = \left[[K] + i\omega\,[C] - \omega^2\,[M]\right]^{-1} \tag{3.41}$$

so that the response $\{u\}$ is related to the excitation $\{Q\}$ by the following equation:

$$\{u\} = \Re\left[[G(\omega)]\,\{Q\}\right] = \Re\left[[G(\omega)]\,\{F\}e^{i\omega t}\right] \tag{3.42}$$

$[[G(\omega)]$ is equivalent to the Complex Frequency Response Function and for this reason is also called *Frequency Response Function Matrix*. Each element of this matrix, $G_{ij}(\omega)$, describes the amplitude and phase of the response of the generalised coordinate i when only the force F_j is acting on the system. A plot similar to that shown in Fig. 3.4 is obtained by plotting the rows of the Frequency Response Function Matrix with respect to the excitation frequency. The plot will show as many peaks as the number of DoF; there are however two circumstances in which peaks will not be present:

1. the force is applied in a node of a mode shape;
2. the response is measured or calculated in a node of a mode shape.

These conditions are of particular importance in experimental testing because they help choosing the location for the sensors and the excitation.

3.2 The problem of damping in composite and sandwich structures

Beside their increased strength-to-weight ratio, composites generally show a higher damping capacity than metals, the main reason being the viscoelasticity of the polymeric matrix. Damping in composites can be optimised by properly choosing their constitutive parameters, such as fibre orientation, layup and constituents' properties. However, in most cases the optimal damping configuration leads to insufficient strength and stiffness, so that a trade-off is usually sought. Sandwiches with viscoelastic cores are designed on purpose to achieve high energy dissipation, but depending on the location and the constraints conditions of the viscoelastic layer, different performances are obtained. An extensive review of the damping properties of composites and sandwiches and modelling techniques can be found in [104–107].

3.2.1 Damping mechanisms in composites

The main source of damping in composites comes from their constituent materials and in particular from the polymeric matrix. With this respect, thermoplastics would better serve the scope but their stiffness is too low for structural applications, so that thermosets are usually preferred [108]. Generally speaking, the damping capacity is proportional to the matrix volume fraction [109–111] but the relative proportion of matrix and fibres are normally set by stiffness and strength requirements. Fibres also contribute to damping, not only with their inherent damping capacity [112–114], but also due to their relative motion with respect to the matrix [115]. Matrix-fibres interaction is crucial for load transmission occurring in shearing, which is the main cause of dissipation in the matrix [116]. To ensure that load transmission occurs without debonding, fibres are chemically treated; the treatment also contributes to the dissipation both due its properties and due to the improved load transmission [117, 118]. Some authors identified a third-phase in the coating or arising from manufacturing processes that alter the area surrounding the fibres creating a zone with intermediate properties [119–121]. The geometry of the reinforcement [122] and the fibres' packing [123] directly impact the friction due to the relative motion of fibres in the matrix or with respect to each other in fabrics [124, 125]. At the scale of the plies and laminate, the orientation of fibres plays a role as it determines the amplitude of shear stresses within the lamina [126–128] and at the interface because of properties' mismatch [129–131]. All polymer-based composites are sensitive to temperature and frequency. Damping has a peak when the material works near the glass transition temperature [104,132]. The effects of frequency are controversial although for most applications the frequency range of interest is such that the material properties can be considered constant [111].

3.2.2 Damping mechanisms in sandwiches

The principal source of damping in sandwiches with a viscoelastic core is the shearing that arises in the core because of the high stiffness mismatch that occurs at core-skins interfaces. The use of viscoelastic layers is an established method to increase damping [133–139]. Damping is found to increase as the thickness of the core increases [140, 141]; moreover, for a given viscoelastic fraction, damping is higher when one layer is placed on the plane of maximum shearing rather than using two layers at arbitrary locations in the layup. On the other hand, an experimental comparison of distributed and patched treatments [142] shows that if patches are applied at nodes' location the same damping of a distributed treatment can be achieved together with a reduction in weight. The use of composites as face sheets creates an issue as co-curing of core and skins become

necessary [143]. As an alternative, the viscoelastic layer is applied on top of the structure, covering it all or just part of it [144,145]. As a matter of fact, the addition of viscoelastic layers tends to degrade the stiffness properties; in order to overcome this issue the addition of carbon nano-tubes at the interface between the stiff and soft layers has been proposed [108] which has the twofold effect of increasing the stiffness and the temperature resistance.

3.2.3 Damping models

Damping models for composites and sandwiches are based on models for polymeric materials. The simplest way to represent damping is using linear viscoelastic models [146] such as Maxwell, Kelvin, Maxwell-Kelvin and Zener models (Fig. 3.5).

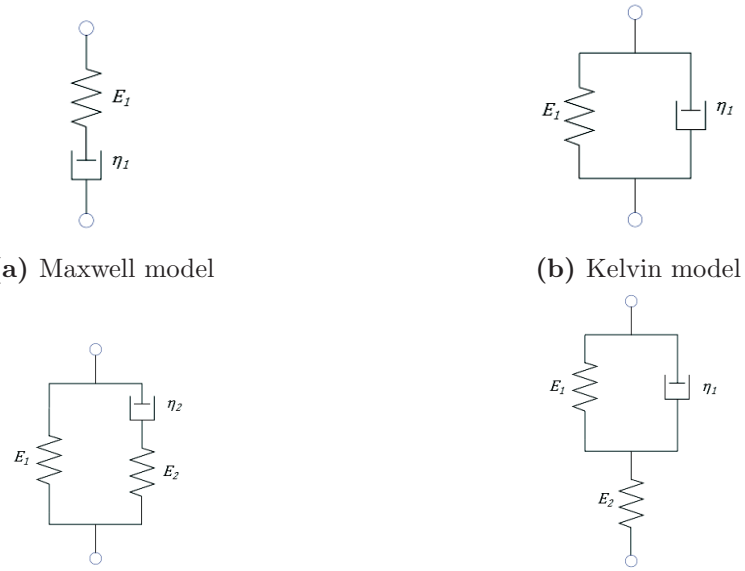

(a) Maxwell model

(b) Kelvin model

(c) Maxwell-Kelvin model

(d) Zener model

Fig. 3.5. Linear Viscoelastic Models

If on the one hand they are easy to handle from the mathematical point of view and require only few material parameters, on the other hand they are simplistic and fail to represent the underlying physics of the dissipation phenomena. Some improvements are achieved using the Prony Series model, which describes damping as a summation of decaying exponentials. Another way to improve the viscoelastic models is the use of fractional derivatives [147]. The accuracy of this method depends on the number of parameters chosen but in general it is fairly accurate over a broad frequency range and can model materials with asymmetric loss factors' peaks. A commonly used approach, especially in finite element codes, is that of the complex modulus. The Young and or the shear modulii are defined as complex numbers in which the real part describes

the elastic behaviour of the material and the imaginary part describes its dissipative behaviour. The ratio between the imaginary and the real part is the *loss factor*. The use of this method is limited to frequency domain because in time-domain its use may lead to non-causality issues [148, 149]. Strain-energy methods are also easily embedded in finite element codes. They express the damping in terms of the *Specific Damping Capacity* (SDC) that is calculated as the ratio between the stored and the dissipated energy [126,150,151]. In the same framework are the *Modal Strain Energy Method* (MSE) and the *Iterative Modal Strain Energy Method* (ISME) [152]. The MSE calculates the modal loss factor starting from the strain energy of the undamped configuration; the IMSE accounts for the frequency dependency of the material by iteratively solving the equations. Physics-based models try to model the physics of the energy dissipation. They can be defined as *Internal Variables Models* because they rely on the definition of additional internal variables to physically describe damping. Examples of this approach are given by the *Anelastic Displacement Field Model* [153], the Golla-Hughes-McTavish model [154], the *Augmented Thermodynamic Field* [155]. All of them are very accurate in the description of the damping mechanisms but they are hardly applicable because of the high number of parameters needed and the difficulty to determine them.

3.2.4 The complex stiffness matrix of the RZT beam

For the RZT beam the complex modulus approach was chosen for its easiness of implementation and considering that the beam element is used for preliminary analysis of beam-like structures and as such a more detailed representation of damping is not needed. In the derivation of the RZT it was assumed that the zigzag effect was exclusively due to the transverse shear stresses arising at the interface of layers with different material properties. Moreover, from the preceding analysis of damping mechanisms it is clear that shearing will drive the dissipation. Therefore, in the analysis of damping of composites and sandwich beams, the complex modulus formulation will be employed for the transverse shear modulus only. In Eq. 3.43 G^*_{13} is the complex shear modulus, G'_{13} is the storage modulus (elastic part) and G''_{13} is the loss modulus (dissipative part).

$$G^*_{13} = G'_{13} + iG''_{13} \tag{3.43}$$

$$\eta = \text{loss factor} = \frac{G''_{13}}{G'_{13}} \tag{3.44}$$

$$G^*_{13} = G'_{13}(1+\eta) \tag{3.45}$$

The loss factor is assumed constant over the frequency range of interest. The zigzag function strictly depends on the shear modulus; however for its computation only the real part of the modulus is considered. The resulting element stiffness matrix will be

given by:

$$\boldsymbol{K}^{(e)} = \boldsymbol{K}_p^{(e)} + \boldsymbol{K}_t^{*(e)} = \boldsymbol{K}_p^{(e)} + (1+\eta)\boldsymbol{K}_t^{'(e)} \tag{3.46}$$

3.3 The mass matrix of the RZT beam

The mass matrix of the RZT beam was obtained following the variational formulation and using the same linear interpolation functions used for the definition of the stiffness matrix, i.e. consistent mass matrix formulation. The kinetic energy of a beam of density ρ, volume V, moving at velocity $\boldsymbol{v}$ is given by:

$$T = \frac{1}{2}\int_V \rho \boldsymbol{v}^T \boldsymbol{v} dV \tag{3.47}$$

The vector of generalised velocities is obtained by derivation of Eq. 1.31 with respect to time:

$$\begin{aligned} \dot{u} &= \dot{u_0} + z\dot{\theta} + \phi^{(k)}\dot{\psi} \\ \dot{w} &= \dot{w_0} \end{aligned} \tag{3.48}$$

The kinetic energy can be re-written as:

$$T = \frac{1}{2}\int_V \rho \left(\dot{u}^2 + \dot{w}^2\right) dV \tag{3.49}$$

Combination of Eq. 3.49 and Eq. 3.48 gives:

$$T = \frac{1}{2}\int_V \rho \left[\dot{u_0}^2 + z^2\dot{\theta}^2 + (\phi^{(k)})^2\dot{\psi}^2 + 2\left(z\dot{\theta}\dot{u_0} + \dot{u_0}\phi^{(k)}\dot{\psi} + z\dot{\theta}\phi^{(k)}\dot{\psi}\right) + \dot{w_0}^2\right] dV \tag{3.50}$$

Let L be the length of the beam, b its width and h its thickness. Eq. 3.50 can be re-written as:

$$\begin{aligned} T = \frac{1}{2}\int_0^L \int_{-\frac{b}{2}}^{\frac{b}{2}} \int_{-\frac{h}{2}}^{\frac{h}{2}} \rho \Big[&\dot{u_0}^2 + z^2\dot{\theta}^2 + (\phi^{(k)})^2\dot{\psi}^2 + \dot{w_0}^2 \\ &+2\left(z\dot{\theta}\dot{u_0} + \dot{u_0}\phi^{(k)}\dot{\psi} + z\dot{\theta}\phi^{(k)}\dot{\psi}\right)\Big] dxdydz \end{aligned} \tag{3.51}$$

The width b of the beam is constant; the density ρ is constant over each layer but varies from one layer to the other so that the kinetic energy takes the following form:

$$\begin{aligned} T = \frac{1}{2}b\int_0^L \sum_{k=1}^{N-1} \int_{z_k}^{z_{k+1}} \rho^{(k)} \Big[&\dot{u_0}^2 + z^2\dot{\theta}^2 + (\phi^{(k)})^2\dot{\psi}^2 + \dot{w_0}^2 \\ &+2\left(z\dot{\theta}\dot{u_0} + \dot{u_0}\phi^{(k)}\dot{\psi} + z\dot{\theta}\phi^{(k)}\dot{\psi}\right)\Big] dxdz \end{aligned} \tag{3.52}$$

Integration over the layer thickness gives the following inertial quantities:

$$(\rho_0, \rho_1, \rho_2) = b \sum_{k=1}^{N-1} \int_{z_k}^{z_{k+1}} \rho^{(k)}(1, z, z^2); \tag{3.53}$$

$$(\rho_1^{\phi}, \rho_2^{\phi}) = b \sum_{k=1}^{N-1} \int_{z_k}^{z_{k+1}} \rho^{(k)}(z\phi^{(k)}, (\phi^{(k)})^2; \tag{3.54}$$

We can group all the inertial terms in matrix form:

$$\boldsymbol{R} = \begin{bmatrix} \rho_0 & 0 & \rho_1 & \rho_1^{\phi} \\ 0 & \rho_0 & 0 & 0 \\ \rho_1 & 0 & \rho_2 & \rho_1^{\phi} \\ \rho_1^{\phi} & 0 & \rho_1^{\phi} & \rho_2^{\phi} \end{bmatrix} \tag{3.55}$$

Finally, to obtain the RZT element mass matrix we need to express the above quantities in terms of the element's DoF. In accordance with the consistent formulation chosen, linear interpolation functions are employed (Eq. 2.1) and integration is performed over the element's length $l^{(e)}$.

$$\boldsymbol{M^{(e)}} = \int_0^{l^{(e)}} \boldsymbol{N}^T \boldsymbol{R} \boldsymbol{N} dx \tag{3.56}$$

The same procedure is followed to derive the FSDT mass matrix. The assembly process to obtain the mass matrix of the entire structure is the same as that for the stiffness matrix.

3.4 Undamped free vibrations of laminated beams

Free vibration analysis is performed on two beams, one composite [98] and one sandwich [156], using the RZT beam and the FSDT beam [157]. Results are compared to a refined finite element model solved in Samcef. Tables 3.1-3.2 summarise material properties and beams' geometry.

Composite beam	
$E_{(1)}/E^{(2)} = 25$	$h_{(1)}/h = 0.35$
$E_{(3)}/E^{(2)} = 32.57$	$h_{(2)}/h = 0.35$
$G_{(1)} = 0.02E^{(1)}$	$h_{(3)}/h = 0.25$
$G_{(2)} = 0.2E^{(1)}$	$b = 1$
$G_{(3)} = 8.21E^{(2)}$	$S = \frac{L}{2h} = 8, 16, 32$
$\frac{\rho^{(2)}}{\rho^{(1,3)}} = 0.6818$	

Table 3.1. Composite beam properties and geometry

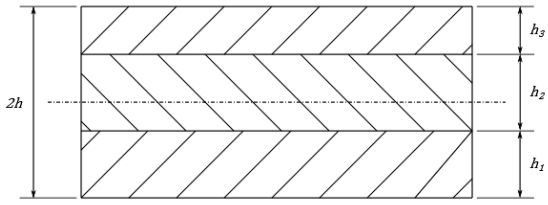

Fig. 3.6. 3-layer asymmetric composite beam

Sandwich beam	
$E_{fs} = 68.9$ GPa	$h_{fs} = 0.40624mm$
$G_{fs} = 26.5$ GPa	$h_c = 6.3475mm$
$\rho_{fs} = 2687.3kg/m^3$	$b = 25.4mm$
$E_c = 179.14MPa$	$S = \frac{L}{b} = 5, 10, 15$
$G_c = 68.9MPa$	
$\rho_c = 119.69kg/m^3$	

Table 3.2. Sandwich beam properties and geometry

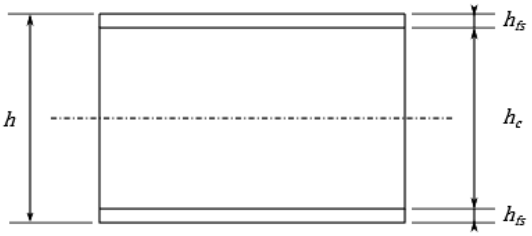

Fig. 3.7. Sandwich beam

The subscripts refer to the layers as specified in Figs. 3.6-3.7 and b is the width of the beams.

The two beams constitute a challenge for the FSDT and ESLT in general for the following reasons:

- in the composite beam properties mismatch and geometric non-periodicity of layers' thickness occur concurrently;
- in the sandwich beam a significant mismatch in material properties occurs at face sheets/core interfaces.

The beams are free at the right end and clamped at the left one. As described in the previous chapter, clamped boundary conditions are challenging for many zigzag theories and eventually overcome by the RZT, which is now tested under dynamic conditions. Three different aspect ratios S are chosen for each beam to show that the FSDT is inadequate also for beams of intermediate slenderness when material properties and

layers' geometry vary steeply in the thickness direction. The values for the sandwich beam with aspect ratio $S = 5$ and $S = 10$ are normalised according to:

$$\bar{\omega}_n = \frac{L^2}{b}\sqrt{\frac{\rho_c}{G_c}} \tag{3.57}$$

and the percentage error given by:

$$\Delta_{\%} = \frac{Sol_{Samcef} - Sol_i}{Sol_{Samcef}} \cdot 100; \quad i = \text{FSDT, RZT} \tag{3.58}$$

An idea of the computational saving that can be obtained with the RZT beam consider Table. 3.3 which gives the total number of DoF for the three models used.

	FSDT Beam	**RZT Beam**	**Samcef Beam**
No. DoF Composite	600	800	2320
No. DoF Sandwich	600	800	32000

Table 3.3. Number of DoF of the finite element beams

Tables 3.4-3.5 contain the eigenfrequencies of the composite and sandwich beams for the different aspect ratios. As the two tables show, the RZT beam can better estimate the eigenfrequencies for all the aspect ratios. For the highest values of S the FSDT beam should converge to the refined Samcef model solution. However, due to the combination of material properties and non uniform layers' geometry the FSDT beam is not able to converge at a faster rate.

Composite beam, S=8						**Composite beam, S=16**					**Composite beam, S=32**				
Mode	Samcef	FSDT	$\Delta_{\%}$	RZT	$\Delta_{\%}$	Samcef	FSDT	$\Delta_{\%}$	RZT	$\Delta_{\%}$	Samcef	FSDT	$\Delta_{\%}$	RZT	$\Delta_{\%}$
1	5.49	6.57	-19.59	5.53	-0.82	1.59	1.68	-5.75	1.59	-0.08	0.42	0.42	-0.71	0.42	0.80
2	21.86	35.08	-60.49	22.18	1.46	7.70	10.05	-30.57	7.79	-1.18	2.38	2.62	-10.02	2.39	-0.37
3	46.85	70.36	-50.18	47.69	-1.78	17.44	26.34	-51.06	17.69	-1.41	5.94	7.19	-21.10	5.99	-0.85
4	68.48	82.90	-21.05	69.55	-1.56	28.24	35.21	-24.67	28.67	-1.53	10.27	13.73	-33.65	10.39	-1.20
5	75.21	136.57	-81.58	77.05	-2.45	34.99	47.59	-36.00	35.13	-0.40	15.07	17.61	-16.83	15.28	-1.41
6	106.92	191.96	-79.53	111.58	-4.36	40.26	72.01	-78.86	40.88	-1.53	17.58	21.98	-25.01	17.59	-0.08
7	139.00	209.80	-50.94	149.93	-7.86	53.33	98.39	-84.49	54.21	-1.65	20.20	31.65	-56.67	20.50	-1.47
8	160.98	249.47	-54.97	169.17	-5.09	67.58	105.36	-55.90	68.88	-1.93	25.59	42.47	-65.96	25.97	-1.50
9	171.72	306.04	-78.22	195.70	-13.96	82.83	126.06	-52.19	84.91	-2.51	31.25	52.76	-68.84	31.72	-1.50
10	176.70	341.28	-93.14	202.37	-14.53	98.52	154.05	-56.37	101.84	-3.37	37.20	54.24	-45.81	37.75	-1.48

Table 3.4. Composite beams eigenfrequencies [Hz]

Sandwich beam, S=5						**Sandwich beam, S=10**					**Sandwich beam, S=15**				
Mode	Samcef	FSDT	$\Delta_{\%}$	RZT	$\Delta_{\%}$	Samcef	FSDT	$\Delta_{\%}$	RZT	$\Delta_{\%}$	Samcef	FSDT	$\Delta_{\%}$	RZT	$\Delta_{\%}$
1	0.37	0.43	16.06	0.37	-0.44	0.41	0.43	4.10	0.41	-0.31	55.9	56.94	1.86	55.83	-0.13
2	1.45	2.58	77.68	1.45	0.00	2.10	2.66	26.78	2.10	-0.13	314.9	355.33	12.84	314.40	-0.16
3	2.98	6.85	129.91	2.98	0.12	4.79	7.34	53.27	4.79	-0.02	772.9	988.38	27.88	772.14	-0.10
4	4.43	7.26	63.84	4.44	0.27	7.69	14.09	83.84	7.69	0.05	1311.2	1918.57	46.32	1310.67	-0.04
5	5.89	12.56	113.44	5.91	0.47	10.64	14.52	36.40	10.65	0.11	1886.2	2890.65	53.25	1886.29	0.00
6	7.31	19.32	164.16	7.26	-0.75	13.57	22.72	67.39	13.59	-0.18	2472.4	3133.83	26.75	2473.50	0.04
7	8.75	21.77	148.89	7.36	-15.82	16.47	32.97	100.13	14.52	-11.89	3059.3	4615.25	50.86	2890.65	-5.51
8	10.18	26.77	163.05	8.84	-13.19	19.35	43.55	125.07	16.52	-14.64	3642.9	6342.22	74.10	3062.09	-15.94
9	11.63	34.70	198.50	10.31	-11.30	22.21	44.61	100.86	19.42	-12.56	4222.2	8293.18	96.42	3648.07	-13.60
10	13.07	36.29	177.58	11.82	-9.60	25.05	57.40	129.13	22.31	-10.95	4797.6	8672.13	80.76	4230.74	-11.82

Table 3.5. Sandwich beams eigenfrequencies [Hz]

3.5 Damped forced response of laminated beams

To understand the ability of the RZT beam to predict the behaviour of damped structures, the harmonic response has been calculated. The same models were used for all simulations except for the sandwich beam for which a full 3D model is employed to be sure to capture the behaviour of the very soft core. The model has 23296 DoF. The time needed to perform the simulation for the refined models is around 1h while the FSDT and the RZT beams require on average 10 s. The simulations were run a Dell Precision M4800 workstation with 8GB RAM and an Intel Core i7-4810MQ Processor (Quad Core 2.80GHz, 3.80GHz Turbo, 6MB). Sample points were taken every 10 Hz. Again, clamped-free boundary conditions are used.

3.5.1 Harmonic response of the composite beam

For the composite beam a loss factor $\eta = 0.35$ is chosen for all layers, being a typical value for glass/epoxy composites [158]. Fig. 3.8 shows the amplitude and phase plots for the transverse response of the composite beam, evaluated at the mid-span, and on the centre line for the refined model, for $S = 16$. As the plots show, the FSDT model fails

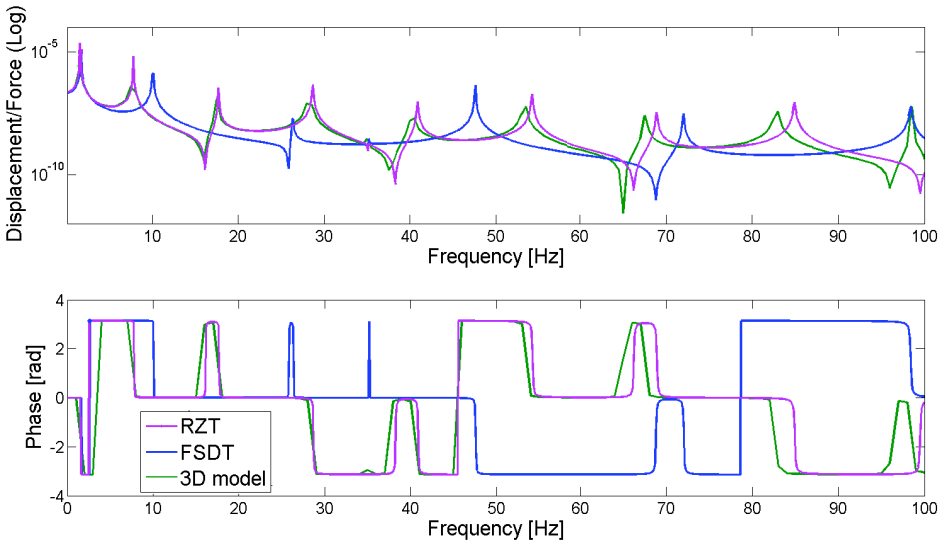

Fig. 3.8. Amplitude (top) and phase (bottom) for the composite beam, S=16

to capture the behaviour of the beam. The peaks are misplaced and the amplitude is also wrongly estimated. In general the FSDT corresponds to a stiffer behaviour. On the other hand the RZT is able to reproduce the response of the refined model. At higher frequencies some discrepancies are found but they are in the order of magnitude of the error made in eigenfrequencies computation.

3.5.2 Harmonic response of the sandwich beam

In the harmonic response of the sandwich beam the force is applied at the free end and the response evaluated at the mid-span. Two tests are run corresponding to two different loss factors. First a low loss factor $\eta = 0.1$ and then $\eta = 1.58$, which corresponds to the value for an automotive damping treatment [159], are used. The loss factor is considered only for the viscoelastic core, being it predominant both geometrically and also for the damping properties with respect to the face sheets. The first test aimed at verifying the behaviour of the RZT beam in presence of a very thick and damped viscoelastic layer. In both cases, the loss factor is assumed constant over the entire frequency range. Figs. 3.9 and 3.10 show the amplitude and phase of the transverse response for an aspect ratio $S = 5$. In 3.9 the peaks are well separated, suggesting again an overestimation of the

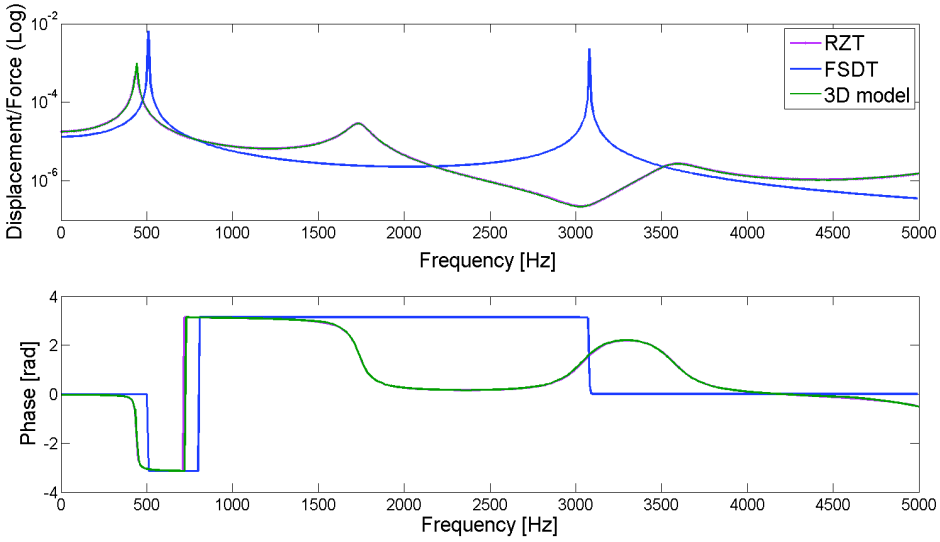

Fig. 3.9. Amplitude (top) and phase (bottom) for the sandwich beam, $S = 5$ and $\eta = 0.1$

stiffness, and the amplitude does not seem to be affected by the presence of damping. On the other hand the RZT beam perfectly reproduces the forced response. The inability of the FSDT beam to correctly predict the damped response of the beam in the case $\eta = 1.58$ is more striking. Despite being more damped than the previous case, the FSDT beam still identify two clear peaks. The second mode is in reality totally damped as the refined model and RZT predictions show. The latter are perfectly overlapping both in amplitude and phase.

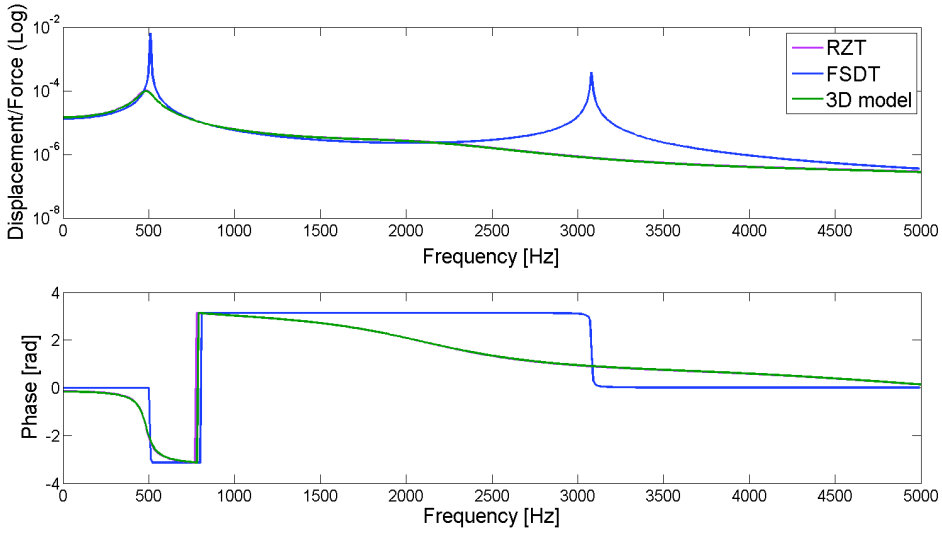

Fig. 3.10. Amplitude (top) and phase (bottom) for the sandwich beam, $S = 5$ and $\eta = 1.58$

3.6 Conclusions

From the preceding analysis it appears that the RZT beam element performance in dynamic analyses is superior to the FSDT beam element. Moreover, the results are in close agreement with those of the refined finite element model and are obtained at a considerably lower computational cost.

The eigenfrequencies predicted by the FSDT reveal an overestimation of stiffness confirmed in the forced response plots by the peaks that are shifted with respect to the reference solution. As far as it concerns damping, FSDT is less sensitive to the presence of the loss factor.

The use of the zigzag function reduces the stiffness of the element and, globally, of the structure eventually matching closely that of a refined 3D model but with a significantly lower number of DoF. The presence of the zigzag function improves also the representation of damping which suggests that the zigzag function is accounting for the transverse shearing in a mathematically and physically consistent way.

Chapter 4

The development of a 2D element and the dynamic analysis of plates and shells

4.1 Plate and shell elements

Many structures of practical interest can be analysed under the assumptions of 2D elasticity, i.e. plane stress and plane strain. A plane stress state occurs in structures that have one dimension, the thickness, which is much smaller than the other two; a plane strain state occurs when the length is much larger than the other two dimensions [75]. In most composite and sandwich plate-like structures, the thickness is considerably smaller than the width and the length and therefore plane stress hypothesis can be used.
In the finite element method such structures are modelled using 2D elements, namely plate and shell elements. The underlying theories that allow us to develop bi-dimensional finite elements were presented in Chapter 1. In the foregoing analysis only the Mindlin theory, which is the 2D equivalent of the FSDT, and the RZT will be considered.
The main difference between plate and shell elements is that plates are flat, thus undergoing only flexural loading, while shells are curved, which implies the rise of membrane forces. However, in laminated structures movements of the mid-plane in the in-plane directions are possible also for flat geometries and therefore combined bending and axial effects take place [94]. Nonetheless other differences exist between the plate and the shell elements as the following paragraphs will show.

4.1.1 The flat plate element stiffness

The derivation of the stiffness matrix starts from the displacement field of Eq. 1.19, repeated here for convenience:

$$\begin{aligned} u(x,y,z) &= u_0(x,y) + z\theta_x(x,y) \\ v(x,y,z) &= v_0(x,y) + z\theta_y(x,y) \\ w(x,y,z) &= w_0(x,y) \end{aligned} \tag{4.1}$$

A plane-stress state is assumed, which allows to neglect the normal transverse strain ε_z. The resulting strains are:

$$\varepsilon_x = \frac{\partial u}{\partial x} = \frac{\partial u_0}{\partial x} + z\frac{\partial \theta_x}{\partial x}; \tag{4.2}$$

$$\varepsilon_y = \frac{\partial v}{\partial y} = \frac{\partial v_0}{\partial y} + z\frac{\partial \theta_y}{\partial y}; \tag{4.3}$$

$$\gamma_{xy} = \frac{\partial u}{\partial y} + \frac{\partial v}{\partial x} = \frac{\partial u_0}{\partial y} + \frac{\partial v_0}{\partial x} + z\left(\frac{\partial \theta_x}{\partial y} + \frac{\partial \theta_y}{\partial x}\right); \tag{4.4}$$

$$\gamma_{xz} = \frac{\partial u}{\partial z} + \frac{\partial w}{\partial x} = \frac{\partial w_0}{\partial x} + \theta_x; \tag{4.5}$$

$$\gamma_{yz} = \frac{\partial v}{\partial z} + \frac{\partial w}{\partial y} = \frac{\partial w_0}{\partial y} + \theta_y; \tag{4.6}$$

In the above equations the membrane, bending and shear deformation can be identified and grouped in the following generalised vector form:

$$\boldsymbol{\varepsilon}_p = \hat{\boldsymbol{\varepsilon}}_{\boldsymbol{m}} + z\hat{\boldsymbol{\varepsilon}}_{\boldsymbol{b}} \quad \boldsymbol{\varepsilon}_s = \hat{\boldsymbol{\varepsilon}}_{\boldsymbol{s}} \tag{4.7}$$

with: (4.8)

$$\hat{\boldsymbol{\varepsilon}}_{\boldsymbol{m}} = \left[\tfrac{\partial u_0}{\partial x}, \tfrac{\partial v_0}{\partial y}, \tfrac{\partial u_0}{\partial y} + \tfrac{\partial v_0}{\partial x}\right]^T; \tag{4.9}$$

$$\hat{\boldsymbol{\varepsilon}}_{\boldsymbol{b}} = \left[\tfrac{\partial \theta_x}{\partial x}, \tfrac{\partial \theta_y}{\partial y}, \left(\tfrac{\partial \theta_x}{\partial y} + \tfrac{\partial \theta_y}{\partial x}\right)\right]^T; \tag{4.10}$$

$$\hat{\boldsymbol{\varepsilon}}_{\boldsymbol{s}} = \left[\tfrac{\partial w_0}{\partial x} + \theta_x, \tfrac{\partial w_0}{\partial y} + \theta_y\right]^T; \tag{4.11}$$

(4.12)

where p refers to in-plane strains and s to transverse shear strains.
Following the same procedure as in the previous chapters, we can derive the laminate stiffness matrix which is paramount for the definition of the element stiffness matrix. The stress-strain relationship reads:

$$\boldsymbol{\sigma_p} = \boldsymbol{D_p}\boldsymbol{\varepsilon_p}; \quad \boldsymbol{\sigma_s} = \boldsymbol{D_s}\boldsymbol{\varepsilon_s}; \tag{4.13}$$

Being h the thickness of the plate, the membrane, bending and shear stress resultants are respectively:

$$\hat{\boldsymbol{\sigma}}_{\boldsymbol{m}} = \begin{Bmatrix} N_x \\ N_y \\ N_{xy} \end{Bmatrix} = \int_{-\frac{h}{2}}^{\frac{h}{2}} \hat{\boldsymbol{\sigma}}_{\boldsymbol{p}} dz; \quad \hat{\boldsymbol{\sigma}}_{\boldsymbol{b}} = \begin{Bmatrix} M_x \\ M_y \\ M_{xy} \end{Bmatrix} = \int_{-\frac{h}{2}}^{\frac{h}{2}} z\hat{\boldsymbol{\sigma}}_{\boldsymbol{p}} dz \quad \hat{\boldsymbol{\sigma}}_{\boldsymbol{s}} = \begin{Bmatrix} Q_x \\ Q_y \end{Bmatrix} = \int_{-\frac{h}{2}}^{\frac{h}{2}} \hat{\boldsymbol{\sigma}}_{\boldsymbol{s}} dz; \tag{4.14}$$

By combination of Eq.4.13 and Eqs.4.14 we obtain:

$$\hat{\boldsymbol{\sigma}}_{\boldsymbol{m}} = \hat{\boldsymbol{D}}_{\boldsymbol{m}}\hat{\boldsymbol{\varepsilon}}_{\boldsymbol{m}} + \hat{\boldsymbol{D}}_{\boldsymbol{mb}}\hat{\boldsymbol{\varepsilon}}_{\boldsymbol{b}}; \tag{4.15}$$

$$\hat{\boldsymbol{\sigma}}_{\boldsymbol{b}} = \hat{\boldsymbol{D}}_{\boldsymbol{mb}}\hat{\boldsymbol{\varepsilon}}_{\boldsymbol{m}} + \hat{\boldsymbol{D}}_{\boldsymbol{b}}\hat{\boldsymbol{\varepsilon}}_{\boldsymbol{b}}; \tag{4.16}$$

$$\hat{\boldsymbol{\sigma}}_{\boldsymbol{s}} = \hat{\boldsymbol{D}}_{\boldsymbol{s}}\hat{\boldsymbol{\varepsilon}}_{\boldsymbol{s}}; \tag{4.17}$$

where:

$$\hat{\boldsymbol{D}}_{\boldsymbol{m}} = \int_{-\frac{h}{2}}^{\frac{h}{2}} D_p dz; \qquad \hat{\boldsymbol{D}}_{\boldsymbol{mb}} = \int_{-\frac{h}{2}}^{\frac{h}{2}} z D_p dz; \tag{4.18}$$

$$\hat{\boldsymbol{D}}_{\boldsymbol{b}} = \int_{-\frac{h}{2}}^{\frac{h}{2}} z^2 D_p dz; \qquad \hat{\boldsymbol{D}}_{\boldsymbol{s}} = \int_{-\frac{h}{2}}^{\frac{h}{2}} k_{ij}(D_s)_{ij} dz \text{ with } i,j = x,y,z; \tag{4.19}$$

where k_{ij} is the shear correction factor. The above membrane, bending and membrane/bending matrices can be grouped in an in-plane stiffness matrix as:

$$\boldsymbol{D}_p = \begin{bmatrix} \hat{\boldsymbol{D}}_{\boldsymbol{m}} & \hat{\boldsymbol{D}}_{\boldsymbol{mb}} \\ \hat{\boldsymbol{D}}_{\boldsymbol{mb}} & \hat{\boldsymbol{D}}_{\boldsymbol{b}} \end{bmatrix} \tag{4.20}$$

The stiffness coefficients $\hat{D}_m, \hat{D}_{mb}, \hat{D}_s$ are a function of plies' material properties and lamination angle as explained in Chapter 1. Being material properties variable through the thickness, the above integrals are actually re-written in discrete form:

$$\hat{\boldsymbol{D}}_{\boldsymbol{m}} = \sum_{k=1}^{N}(z_{k+1} - z_k)\boldsymbol{D}_{\boldsymbol{p}_k}, \quad \hat{\boldsymbol{D}}_{\boldsymbol{mb}} = \sum_{k=1}^{N}\frac{1}{2}(z_{k+1}^2 - z_k^2)\boldsymbol{D}_{\boldsymbol{p}_k}, \quad \hat{\boldsymbol{D}}_{\boldsymbol{b}} = \sum_{k=1}^{N}\frac{1}{3}(z_{k+1}^3 - z_k^3)\boldsymbol{D}_{\boldsymbol{p}_k} \tag{4.21}$$

Once the laminate stiffness matrix is known, it is necessary to express it in terms of the element quantities.

In the same fashion as for 1D problems, the geometry to be analysed is discretised into smaller bi-dimensional domains. If in beams analysis discretisation was mainly a matter

of element length, in 2D problems the geometry of the finite elements also plays a role. The most common geometries are triangles and quadrilaterals. The Mindlin theory allows for the use of linear shape functions, which have to be defined on each side of the element always bearing in mind that their value is 1 in only one node at a time. Comparison of linear triangular elements and linear quadrilateral elements shows that the linear quadrilateral performs better [74,75]. It is indeed common to prefer quadrilateral elements in structural analysis. Mindlin elements suffer, just as Timoshenko beams, from shear-locking problems that are again overcome by using reduced integration to reduce the effect of the shear stiffness on the global behaviour of the element (see Chapter 2). As an alternative, the addition of an internal node has been proposed, to which a so-called *bubble function* is associated. Following the general rule of shape functions, the bubble function takes a unity value at the centre of the element and identically vanishes on the boundaries. The additional displacements and rotations associated with the internal node are just fictitious and the node itself can actually be disregarded after the stiffness matrix has been obtained.

The choice of the shape functions along each side is independent but it is generally preferred to employ an *isoparametric formulation*, that is the same shape functions for all edges. Not only does it simplify the mathematical formulation, but it also positively impacts on the computational efforts.

Linear quadrilateral elements are chosen in this case. The shape functions for a generic quadrilateral element are given in Eq. 4.22 and Fig. 4.1.

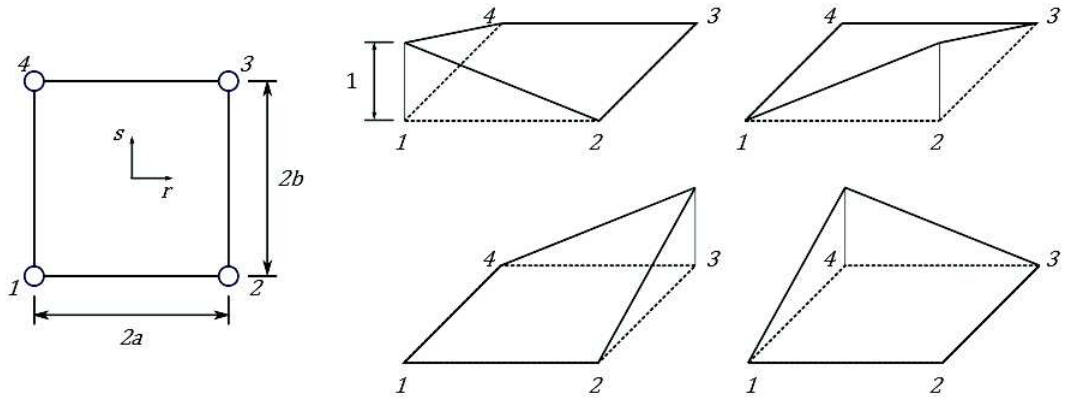

Fig. 4.1. Linear shape functions for a flat quadrilateral element

$$
\begin{aligned}
N_1 &= \frac{1}{4}\left(1-\frac{r}{a}\right)\left(1-\frac{s}{b}\right); \qquad N_2 = \frac{1}{4}\left(1+\frac{r}{a}\right)\left(1-\frac{s}{b}\right) \\
N_3 &= \frac{1}{4}\left(1+\frac{r}{a}\right)\left(1+\frac{s}{b}\right); \qquad N_4 = \frac{1}{4}\left(1-\frac{r}{a}\right)\left(1+\frac{s}{b}\right)
\end{aligned}
\tag{4.22}
$$

For each node of the element the number of unknown variables is 5, namely $a_i^{(e)} = [u_0, v_0, w_0, \theta_x, \theta_y]_i$ where $i = 1, ...,$number of nodes. In this specific case the element will have 4 nodes so that globally the element has 20 DoF. The vector of generalised coordinates, $\boldsymbol{u}$, can therefore be written in terms of nodal displacement as:

$$\boldsymbol{u} = \sum_{i=1}^{N_{nodes}} N_i \boldsymbol{a}_i^{(e)} = \boldsymbol{N}\boldsymbol{a}^{(\boldsymbol{e})} \tag{4.23}$$

being $\boldsymbol{N}$ the shape functions matrix. Substitution of Eq. 4.23 in Eq. 4.6 leads to the following expression:

$$\hat{\boldsymbol{\varepsilon}} = \boldsymbol{B}\boldsymbol{a}^{(e)} \tag{4.24}$$

where $\boldsymbol{B}$ is the strain matrix as already defined in Chapter 2.
The element stiffness matrix is eventually obtained by the integral in equation Eq. 2.19. The global matrix will actually be given by the membrane, bending, membrane-bending coupling and transverse shear contributions, each calculated respectively as:

$$\boldsymbol{K}^{(e)}_{\boldsymbol{m}_{ij}} = \int_{A^{(e)}} \boldsymbol{B}^T_{\boldsymbol{m}_{ij}} \hat{\boldsymbol{D}}_{\boldsymbol{m}} \boldsymbol{B}_{\boldsymbol{m}_{ij}} dA, \qquad \boldsymbol{K}^{(e)}_{\boldsymbol{b}_{ij}} = \int_{A^{(e)}} \boldsymbol{B}^T_{\boldsymbol{b}_{ij}} \hat{\boldsymbol{D}}_{\boldsymbol{b}} \boldsymbol{B}_{\boldsymbol{b}_{ij}} dA, \tag{4.25}$$

$$\boldsymbol{K}^{(e)}_{\boldsymbol{mb}_{ij}} = \int_{A^{(e)}} \boldsymbol{B}^T_{\boldsymbol{mb}_{ij}} \hat{\boldsymbol{D}}_{\boldsymbol{mb}} \boldsymbol{B}_{\boldsymbol{mb}_{ij}} dA, \quad \boldsymbol{K}^{(e)}_{\boldsymbol{s}_{ij}} = \int_{A^{(e)}} \boldsymbol{B}^T_{\boldsymbol{s}_{ij}} \hat{\boldsymbol{D}}_{\boldsymbol{s}} \boldsymbol{B}_{\boldsymbol{s}_{ij}} dA, \tag{4.26}$$

where the integration is performed over the element area. As previously done for the FSDT beam, reduced integration is used for the transverse shear contribution to remove the problem of shear locking.

4.1.2 The flat shell element stiffness

Classification of shell elements is usually done based on the shape of their mid-surface, which is generally curved. The geometrical definition of curved shells and their governing equations are complex [20], so that a common approach is to replace the shell by folded flat elements. It was mentioned in the previous paragraph that a flat laminated element already features all the characteristics of a shell, that is it already accounts for membrane and bending stiffness. In the development of a laminated flat shell some modifications are however needed in order to guarantee continuity and consistency of quantities at elements' common boundaries.
The first thing to account for is the fact that the shell element can be arbitrary oriented with respect to a global coordinate system. The derivation of the stiffness matrix for a composite shell element follows the procedure outlined in the previous chapter with the only difference that all the involved quantities are calculated in a local element frame (x', y', z') (Fig. 4.2).

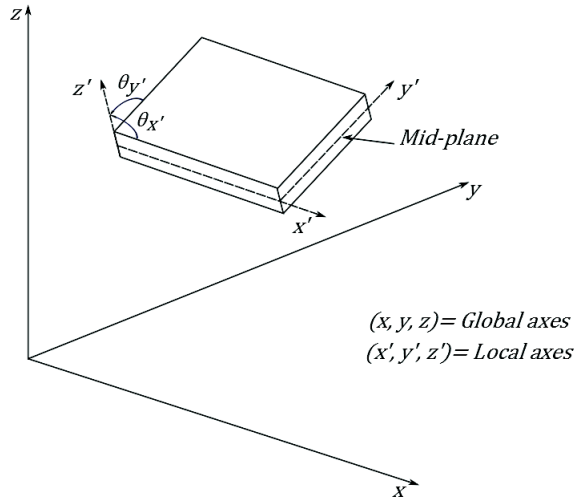

Fig. 4.2. Global and local frame for shell elements definition

Each element of the discretised domain will have its own local axes system (Fig. 4.3). Assembly of the stiffness matrix and nodal forces vector requires however all of them to be defined in the same reference frame.

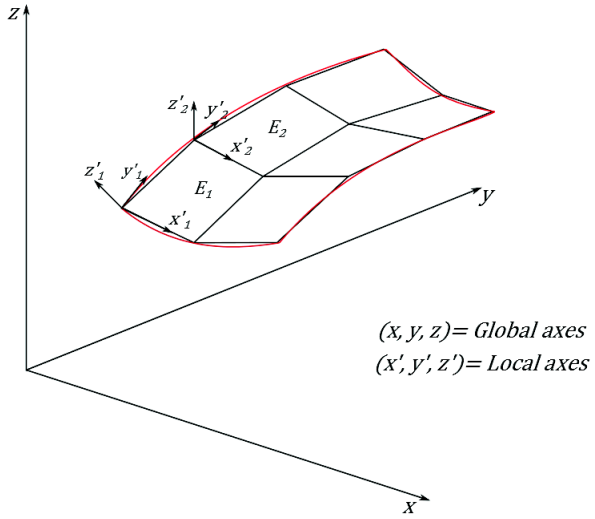

Fig. 4.3. Orientation of neighbouring flat shell elements

Transformation of the matrices is therefore needed. For shells this process is made more cumbersome by the rise of an extra rotation around the z axis during the transformation of the two rotations $\theta_{x'}$ and $\theta_{y'}$, which also introduces an extra bending moment, M_{z_i}. The relation between the local and global displacements for an element (e) is:

$$\boldsymbol{a}_i^{\prime(e)} = \boldsymbol{L}_i \boldsymbol{a}_i^{(e)} \tag{4.27}$$

where now the vector $\mathbf{a}^{(e)}$ contains the rotation around the z axis:

$$\boldsymbol{a}_i^{(e)} = [u_{0_i}, v_{0_i}, w_{0_i}, \theta_{x_i}, \theta_{y_i}, \theta_{z_i}]^T \tag{4.28}$$

The element we are considering is flat, which implies that the transformation matrix $\boldsymbol{L}_i$ is constant for all the nodes and defined as:

$$\boldsymbol{L}_i = \begin{bmatrix} \left[\lambda_{displ}^{(e)}\right] & \mathbf{0} \\ \mathbf{0} & \left[\lambda_{rot}^{(e)}\right] \end{bmatrix} \tag{4.29}$$

with

$$\lambda_{displ}^{(e)} = \begin{bmatrix} \lambda_{x'x} & \lambda_{x'y} & \lambda_{x'z} \\ \lambda_{y'x} & \lambda_{y'y} & \lambda_{y'z} \\ \lambda_{z'x} & \lambda_{z'y} & \lambda_{z'z} \end{bmatrix} \quad \lambda_{rot}^{(e)} = \begin{bmatrix} -\lambda_{y'x} & -\lambda_{y'y} & -\lambda_{y'z} \\ \lambda_{x'x} & \lambda_{x'y} & \lambda_{x'z} \end{bmatrix} \tag{4.30}$$

where each element of the matrix is the cosine of the angle between the axes indicated in the subscript. The complexity of the transformation depends on the choice of the local axis system for which several options are available [94]. The shell element used in the foregoing analysis belongs to the structural library of Samcef and has the local frame defined such that the x' axis lays on an element's edge [160].

Shell elements can also be used to model flat geometries. In this case all the elements are coplanar and during the assembly process the rotation around the z axis, $\theta_{z'}$ is zero making the global stiffness matrix singular. Different techniques have been proposed to overcome the singularity issue in coplanar and quasi-coplanar cases [94], such as the *selective assembly in local axis* or the use of a sixth DoF corresponding to the z axis rotation. This DoF can be fictitious so that the associated rotational stiffness is artificial or can have a real physical meaning, being usually referred to as *drilling DoF*. The Samcef shell element employs the sixth DoF with artificial rotational stiffness.

4.2 The RZT 2D element

Tessler RZT served as a starting point for several authors and their proposed finite element and analytical formulations.

Versino et al. [161] proposed both a 6-noded and a 3-noded C^0-continuous triangular plate element. To avoid the shear locking that occurs in Mindlin elements with isoparametric interpolation functions, anisoparametric shape functions are used: linear interpolation is used for in-plane displacements, bending rotations, zigzag amplitudes; parabolic interpolation is used for the deflection. In the 6-noded triangle the corner nodes have 7 DoF, while the mid-side nodes have just 1 DoF that is the transverse deflection. To reduce the element to a 3-noded triangle, it is imposed that the shear strains

along the edges are constant with respect to the local edge coordinate. By comparing the numerical results to Pagano 3D elasticity solution, the superiority of the 6-noded element is assessed. Barut et al. [162] presented a C^0 triangular element based on the RZT. The element consists of 6 nodes, 3 on the corners and 3 on the mid-sides, with 11 and 3 DoF respectively. The element uses 2^{nd} order expansions for both in-plane and transverse displacements. The element is validated against a 3D FE model, leading accurate results for both symmetric and non-symmetric laminated plates with different boundary conditions. In Iurlaro et al. [163] the RZT is assessed for the bending, free vibration and buckling of plates. Results are compared to the exact and 3D elasticity solutions, the Linear Zigzag Theory, the Higher Order Zigzag model and the HSDT. All the zigzag formulations show a higher degree of accuracy when compared to the HSDT [64]. Eijo et al. [164] used a 4-noded C^0 quadrilateral with 7 DoF per node. The shear locking is avoided by assuming a linear strain field. Unlike the previous one, the interpolation is Lagrangian isoparamteric. The authors question the hypothesis of constant transverse modulus adopted by Tessler that ensures continuity but does not accurately predict the actual distribution. Therefore an *a posteriori* procedure for the computation of transverse stress components is proposed. In the case of highly heterogeneous materials and clamped boundary conditions, however, the convergence to the 3D elasticity solution is slower. Kumar et al [165] proposed a 9-noded quadrilateral having 7 DoF per node. The model uses a parabolic variation across the thickness to retain the possibility of strain jumps at layer interface and C^0 continuity is maintained by assuming that rotations are independent. However, to keep the formulation consistent a penalty matrix approach is employed for the stiffness.

The current RZT shell element is implemented in Samcef. A 4-noded, C^0 continuous quadrilateral element is developed. The mono-dimensional theory discussed in Chapter 2 is readily extended to bi-dimensional problems. The displacement fields used to derive the element stiffness matrix is [73]:

$$\begin{aligned} u_1^k(x,y,z) &= u_0(x,y) + z\theta_1(x,y) + \phi_1^k(z)\psi_1(x,y) \\ u_2^k(x,y,z) &= u_0(x,y) + z\theta_2(x,y) + \phi_2^k(z)\psi_2(x,y) \\ u_3(x,y,z) &= w_0(x,y) \end{aligned} \tag{4.31}$$

where the subscripts $(1,2,3)$ refers to the (x,y,z) axes respectively and the other symbols have the usual meaning. The definition of the zigzag functions in the x and y directions follows the same procedure as the beam theory with the only difference that the homogenised transverse shear modulus is a function of the corresponding coefficient

in the laminate stiffness matrix, Eqs. 4.32-4.33.

$$\beta_1^{(k)} = \frac{G_1}{Q_{11}^{(k)} - 1}; \qquad \beta_2^{(k)} = \frac{G_2}{Q_{22}^{(k)} - 1} \tag{4.32}$$

where:

$$G_1 = \frac{1}{h}\sum_{k=1}^{N} \frac{h^{(k)}}{Q_{11}^{(k)}}; \qquad G_2 = \frac{1}{h}\sum_{k=1}^{N} \frac{h^{(k)}}{Q_2^{(k)}} \tag{4.33}$$

The resulting element has 9 DoF, that is the 7 unknowns in Eq. 4.31 to which two extra rotations are added in the same fashion of the Mindlin element, one to account for the transformation of θ_x and θ_y and one which allows the transformation of the zigzag rotations ψ_x and ψ_y. The resulting generalised coordinates vector for the $i-$th node eventually takes the following form:

$$\boldsymbol{a}_i^{(e)} = [u_{0_i}, v_{0_i}, w_{0_i}, \theta_{x_i}, \theta_{y_i}, \theta_{z_i}, \psi_{x_i}, \psi_{y_i}, \psi_{z_i}]^T \tag{4.34}$$

4.3 Static analysis of beam-like and plate structures

Verification of the implementation of the element is performed through a simple static test. First, beam-like flat structures [72,96] are chosen and results compared to those of the RZT beam element that has already been validated. Then, a flat square panel with different layups is considered. Unlike the beam element, the layer-wise variation of the axial displacement cannot be reconstructed, therefore only the transverse displacements are compared.

4.3.1 Beam-like structures

Two test cases are considered. Material properties, in GPa, and layup are summarised in Table 4.1.

	E_1	E_2	G_{13}	G_{23}
3-layer composite beam, [0/90/0]	25	1	0.5	0.2
3-layer sandwich beam				
Upper face sheet	73	–	29.2	–
Core	0.073	–	0.029	–
Lower face sheet	21.9	–	8.76	–

Table 4.1. Beam-like structures layups and materials

The simulations are run for cantilever and clamped-clamped boundary conditions and the load is uniformly distributed over the entire beam length. Every beam is modelled using the FSDT and RZT beam elements, the RZT shell and a refined finite element model. The composite beam is tested for an aspect ratio, S=length/thickness, equal to 5 and 10. Table 4.2 details the number of elements used for each model.

	FSDT beam/RZT beam	**RZT shell**	**Refined FE model**
Composite beam, S=5	200	1024	1216
Composite beam, S=10	200	1024	2400
Sandwich beam	200	1024	7200

Table 4.2. Number of elements for the different models

The deflection is measured at the beam tip for the cantilever case and the beam mid-span for the clamped-clamped case. Table 4.3 summarises the results. Deflections are normalised according to Eq. 4.35 and to Eq. 4.36 for the composite and sandwich beam respectively:

$$\overline{\mathbf{w}} = \frac{100 b E_1 h^3 w}{q_0 L^4}; \tag{4.35}$$

$$\overline{\mathbf{w}} = \frac{\pi^4 D_{11} w}{100 q_0 L^4}; \tag{4.36}$$

	FSDT beam	RZT beam	RZT shell	Refined FE model
Cantilever				
Composite beam, S=5	6.7033	7.347	7.348	7.5997
Composite beam, S=10	3.3283	3.6037	3.6045	3.6736
Sandwich beam	0.6931	7.5202	7.5201	7.5838
Clamped-clamped				
Composite beam, S=5	1.6296	1.7009	1.701	1.7772
Composite beam, S=10	0.5046	0.5753	0.5754	0.5968
Sandwich beam	0.0651	1.9172	1.9172	1.9408

Table 4.3. Static deflection for the different models

The expectations for this set of simulations was to obtain, with the RZT shell, values that are comparable to those given by the RZT beam when beam-like structures are analysed. However, a closer look at numerical values reveals once again the superior behaviour of the RZT theory when low aspect ratio composite beams and sandwiches are studied.

4.3.2 Plate structures

The analysis of plates involves both composites and sandwiches. They all have an edge clamped and a concentrated load applied on the opposite side at half of its length. The plates are modelled using the Samcef Mindlin element and the RZT shell and they are compared to a 3D model for validation purposes. The composite plate is made of Carbon/Epoxy layers; the sandwich has Carbon/Epoxy layers and a PVC core. The material properties, the geometry and the layups are given in Tables 4.4-4.6. Fig. 4.4 shows the composite and sandwich plates 3D meshes and the application of boundary conditions and loads. Table 4.7 shows the different number of elements and DoF used to model the composites and sandwich plates.

Materials' Properties			
	Normal Moduli	**Shear Moduli**	**Poisson's Ratio**
Carbon/Epoxy	$E_1 = 157.9$ GPa	$G_{12} = 5.930$ GPa	$\nu_{12} = 0.32$
	$E_2 = 9.584$ GPa	$G_{13} = 3.277$ GPa	$\nu_{13} = 0.32$
	$E_3 = 9.584$ GPa	$G_{23} = 5.930$ GPa	$\nu_{23} = 0.49$
PVC	$E = 104$ MPa	$G = 40$ MPa	$\nu = 0.3$

Table 4.4. Materials' properties of plates

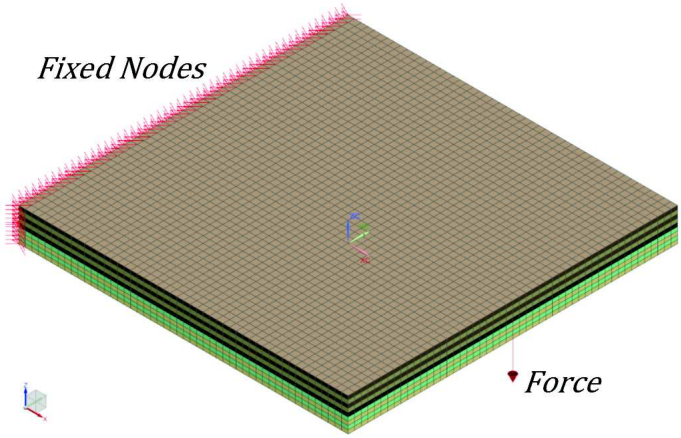

(a) Composite plate

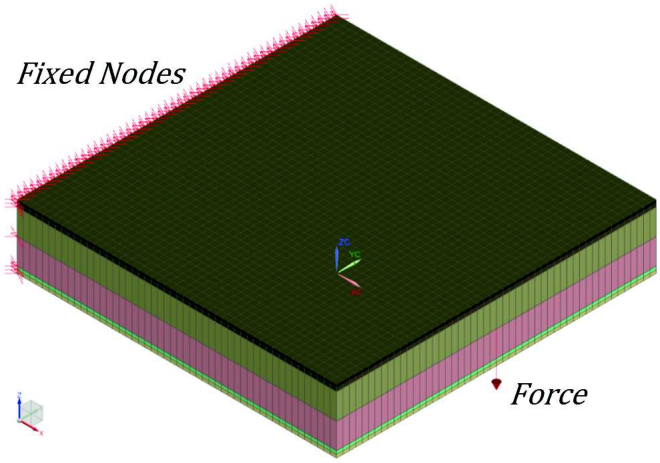

(b) Sandwich plate

Fig. 4.4. 3D meshes, boundary conditions and load for the composite and sandwich plate

Geometry		
	Side	**Layer Thickness**
Composite Plates	0.1 m	h_i=1.12·10^{-3} m for i=1,...9
Sandwich Plates	0.1 m	h_i=1·10^{-3} m for i=1,2,3,4 h_{Core}=16·10^{-3} m

Table 4.5. Plates' geometry

Stacking sequence	
Composite Plate 1	$[30/-45/30/-45/0/45/-30/45/-30]$
Composite Plate 2	$[0/90/0/90/0/90/0/90/0]$
Sandwich Plate 1	$[30/-45/Core/45/-30]$
Sandwich Plate 2	$[0/90/Core/90/0]$

Table 4.6. Plates layups

Flat plates number of Elements and DoF			
	3D Model	**Mindlin Shell**	**RZT Shell**
Composite plates			
No. Elements	25000	2500	2500
No. DoF	85833	15606	23409
Sandwich plates			
No. Elements	15000	2500	2500
No. DoF	54810	15606	23409

Table 4.7. Plates' number of elements and DoF

The deflection is estimated on the mid-plane at the centre of the plate. Results are reported below (Table 4.8-4.9) and the percentage error is calculated as:

$$E_{\%} = \frac{\text{3D Solution} - \text{Current solution}}{\text{3D Solution}} \cdot 100 \tag{4.37}$$

The results show that for the composite plates the RZT does not have a significant impact on the results compared to the Mindlin shell; different conclusions can be drawn from the sandwich results, for which the RZT shell brings a higher accuracy.

Composite plates					
	3D Model	Mindlin Shell	$E_{\%}$	RZT Shell	$E_{\%}$
Plate 1	$2.1996 \cdot 10^{-7}$ m	$2.2013 \cdot 10^{-7}$ m	-0.08	$2.1467 \cdot 10^{-7}$ m	-2.41
Plate 1	$1.2567 \cdot 10^{-7}$ m	$1.2640 \cdot 10^{-7}$ m	-0.58	$1.2510 \cdot 10^{-7}$ m	0.46

Table 4.8. Composite plates' centre deflection

4.3.3 Conclusions

The different impact that the use of the zigzag function has on the composite and sandwich plates allows us to make some important remarks. First of all, the comparable

Sandwich plates					
	3D Model	Mindlin Shell	$E_{\%}$	RZT Shell	$E_{\%}$
Plate 1	$5.8690 \cdot 10^{-7}$ m	$6.7020 \cdot 10^{-7}$ m	-14.19	$5.8400 \cdot 10^{-7}$ m	0.5
Plate 1	$5.1774 \cdot 10^{-7}$ m	$5.9827 \cdot 10^{-7}$ m	-15.55	$5.1592 \cdot 10^{-7}$ m	0.35

Table 4.9. Sandwich plates' centre deflection

accuracy of the Mindlin and RZT elements suggests that no significant zigzag effect occurs in the composite panels. A closer look at the deformation in the 3D model confirms this hypothesis (Fig. 4.5a). The reasons behind it are to be found in material properties and geometry. Compare the percentage error for the composite plates. For Plate 1, the difference in transverse shear properties as we move from one layer to the next is minimum (Fig. 4.6); in addition to this, the individual layer thickness is also low. In Chapter 2 the RZT has been defined showing that its slope depends on no layers' thickness and transverse shear stiffness. These two effects, i.e. similar transverse shear moduli and thin layers, concur to reduce the zigzag effect in the laminate. In particular the slope will only slightly vary from one layer to the other and the overall contribution of the zigzag function will be negligible compared to the Mindlin's one. The effect related to the geometry were explained in Chapter 2 when discussing the static results for Test 3. The same behaviour can be observed within the laminate that constitutes the face sheets of the sandwich plate (Fig. 4.5b), which further confirms the previous considerations.

The effects of the material properties can be appreciated when comparing the percentage errors for Plate 1 and Plate 2. In Plate 2 the transverse shear properties mismatch at layers' interface is higher since we are moving from a 0 ° to a 90° layer (Fig. 4.6). The effect of the zigzag function in this case is that of a minimal improvement with respect to the Mindlin element. However, the difference is not such as to justify the increased DoF number. That being said, one would expect the RZT element converge to the Mindlin one for quasi-homogeneous or homogeneous materials [72]. However, this is not the case because of the implementation performed in Samcef which disregards the calculation of the shear correction factor when the RZT element is used to model homogeneous structures. It is worth to remind that the definition of the zigzag function prescribes it to return to the underlying FSDT for homogeneous materials. While this information can be used for validation purposes, it is hardly of any use in practice since the use of the RZT to model homogeneous materials will just increase the number of DoF, thus the computational effort, without improving the accuracy. In cases where some differences occur in transverse shear properties through the thickness the use of the RZT shell should be evaluated considering the mutual interaction of layers' thickness and material properties in the definition of the zigzag function.

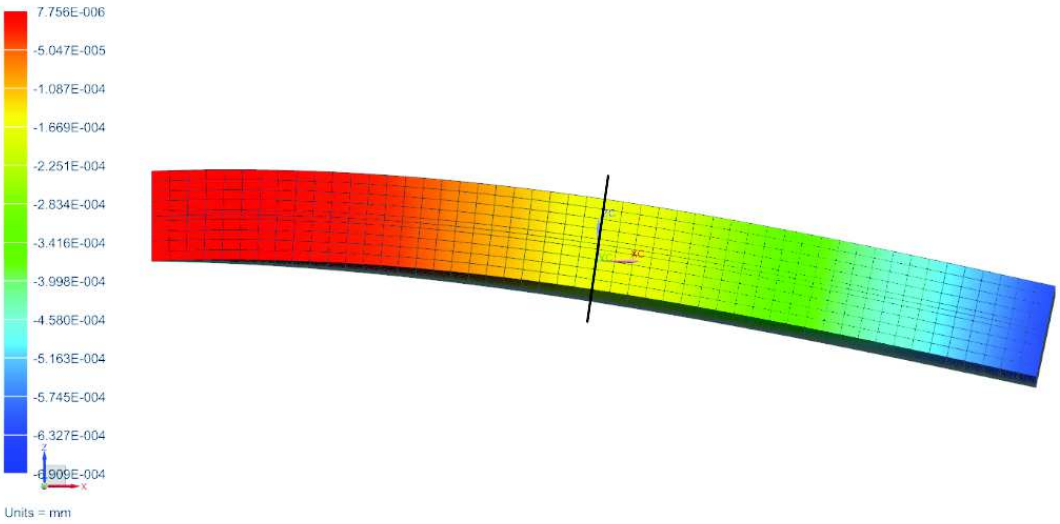

(a) Through-the-thickness deformation of the composite plates computed for the 3D model

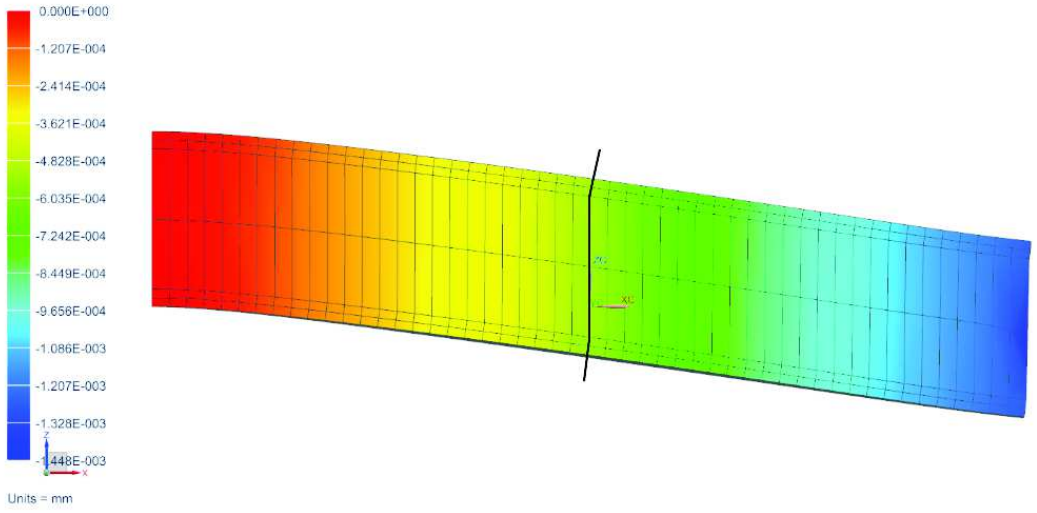

(b) Through-the-thickness deformation of the sandwich plates computed for the 3D model

Fig. 4.5. Zigzag effect in the composite and in the sandwich plates

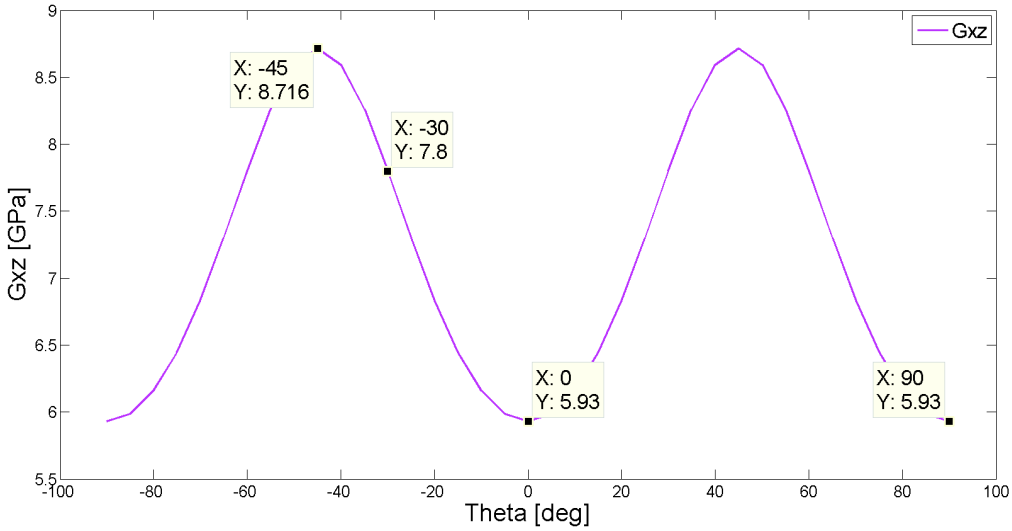

(a) G_{xz} vs. θ

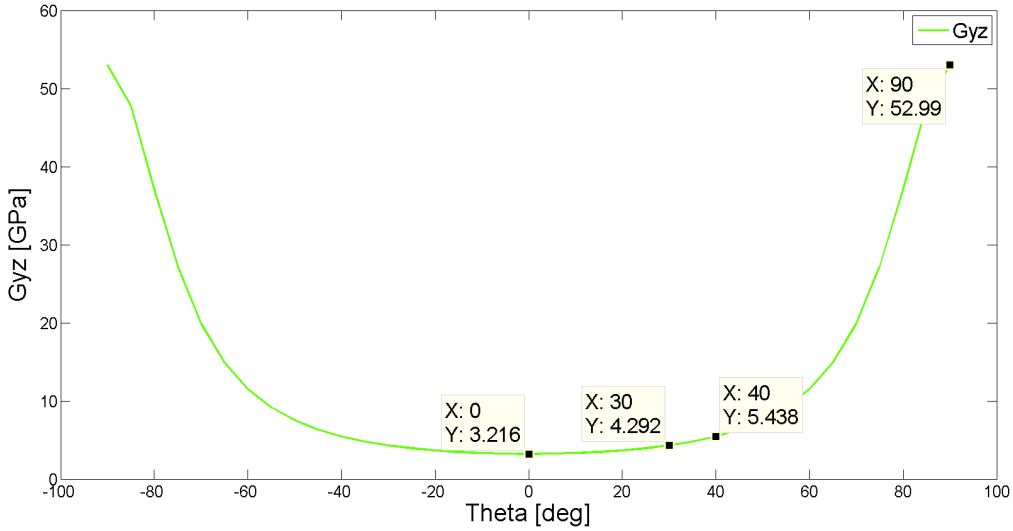

(b) G_{yz} vs. θ

Fig. 4.6. Transverse Shear Moduli variation with θ

The behaviour changes when considering the sandwich, where the improvements brought by the zigzag function are evident. In this case, the transverse shear stiffness mismatch and the thick core both concur to a remarkable variation in slope.

4.4 Model Correlation - Eigenfrequencies and Mode Shapes comparison

The comparison of modal analysis data is usually done on two levels, the eigenfrequencies and the mode shapes. The eigenfrequencies give a direct indication on the accuracy of the mass and stiffness assumptions made for the structure at a global level; the mode

shapes give more detailed information on how mass and stiffness are distributed over the structure [166].

When comparing natural frequencies, it is important to bear in mind that the modes correspondence may no be one-by-one and therefore corresponding modes have to be identified first [167]. The data can further be arranged in graphical form, plotting the frequencies of the model to verify against the frequencies of the reference model. A good agreement is found when all the data points lay on the bisector.

Comparison of mode shapes can be done in several ways: visual comparison, 45° plot, *Modal Assurance Criterion*, *Co-ordinate Modal Assurance Criterion*, *Cross Orthogonality*. [101]. Visual comparison is based on comparison of modes' plots. As a first tool, it is helpful to identify missing modes or significant differences in the deformed shapes. Just as for the frequencies, corresponding mode shapes can be plotted against each other. If the mode shapes are identical and scaled in the same way, then all the point will lay on a line at 45°. The distance of the points from the 45°-line is an indicator of the degree of correlation, i.e. the further the points the worse the correlation.

The Modal Assurance Criterion (MAC) expresses in numerical form the information of the 45° plots. Each mode shape of one set is compared to every mode shape of the reference set. The MAC values are calculated according to:

$$MAC(i,j) = \frac{\left\| \{\psi\}_i^{M1^T} \{\psi\}_j^{M2^T} \right\|}{\left(\{\psi\}_i^{M1^T} \{\psi\}_i^{M1^T} \right) \left(\{\psi\}_j^{M2^T} \{\psi\}_j^{M2^T} \right)} \tag{4.38}$$

where:

M_i: models for which correlation is sought;
$\{\psi\}_{ij}$: mode shape vectors;
i=1,..., N: number of modes of Model 1;
j=1,..., N: number of modes of Model 2.

Eq. 4.38 returns a number which measures how similar the mode shapes are. Two identical modes will have MAC=1; on the other end MAC=0 means that the two modes do not show any correlation. The MAC can take intermediate values and as a rule of thumb it is assumed that two modes are well correlated for MAC$\geq$0.8. The MAC values for all the modes can be plot in matrix form, as it will be shown later, to conceive correlation information in an immediate and compact way .

4.5 Modal analysis of flat and curved panels

The RZT shell is used in this chapter to perform the dynamic analysis of flat and curved laminated panels. The mass matrix of the element is again derived according to the consistent formulation. As previously done, the results obtained with the RZT shell are compared to the Mindlin and 3D modelling, with the latter assumed as reference. Eigenfrequencies will be directly compared and the percentage error with respect to the reference solution will be taken as a measure of the models' accuracy. For the mode shapes comparison the MAC matrix will be constructed. The correlation analysis is run in Siemens LMS Virtual.Lab - Correlation workbench. The results of the static analysis in the previous chapter showed that the performance of the RZT shell justify its use when significant mismatch in properties at layers' interface and non-uniform distribution of layers' thickness occurred. Consequently, the dynamic validation of the element has been done preferably on sandwich structures.

4.5.1 Flat square plates

The sandwich panels considered for the dynamic analysis are the same used for the static test. Material properties, geometry and layup are reported below for convenience (Table 4.10-4.12). The first 15 modes are computed. Frequency values, in Hz, and comparison among the models are given in Tables 4.13-4.14. The percentage error is calculated as usual:

$$E_{\%} = \frac{\text{3D Solution} - \text{Current solution}}{\text{3D Solution}} \cdot 100 \tag{4.39}$$

The number of elements and DoF for the different models are reported in Table 4.7

Materials' Properties			
	Normal Moduli	**Shear Moduli**	**Poisson's Ratio**
Carbon/Epoxy	$E_1 = 157.9$ GPa	$G_{12} = 5.930$ GPa	$\nu_{12} = 0.32$
	$E_2 = 9.584$ GPa	$G_{13} = 3.277$ GPa	$\nu_{13} = 0.32$
	$E_3 = 9.584$ GPa	$G_{23} = 5.930$ GPa	$\nu_{23} = 0.49$
PVC	$E = 104$ MPa	$G = 40$ MPa	$\nu = 0.3$

Table 4.10. Plates' materials' properties

The MAC matrix is calculated for the Mindlin Shell-3D model and the Zigzag shell-3D model pairs. Figs. 4.7-4.8 show the results for Plate 1 and Plate 2.

Geometry		
	Side	**Layer Thickness**
Sandwich Plates	0.1 m	h_i=1·10^{-3} m for i=1,2,3,4 h_{Core}=16·10^{-3} m

Table 4.11. Plates' geometry

Stacking sequence	
Sandwich Plate 1	$[30/-45/Core/45/-30]$
Sandwich Plate 2	$[0/90/Core/90/0]$

Table 4.12. Plates layups

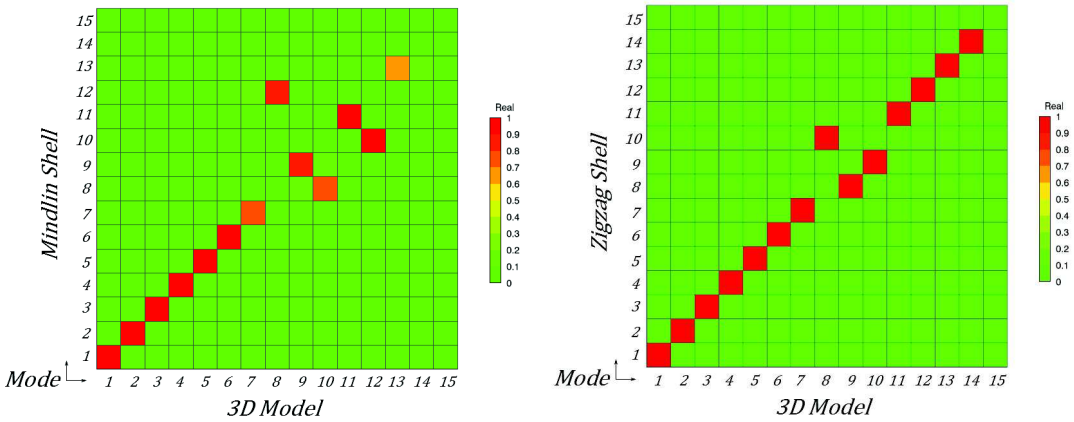

(a) Mindlin Shell vs. 3D Model **(b)** Zigzag Shell vs. 3D Model

Fig. 4.7. MAC matrices for Plate 1

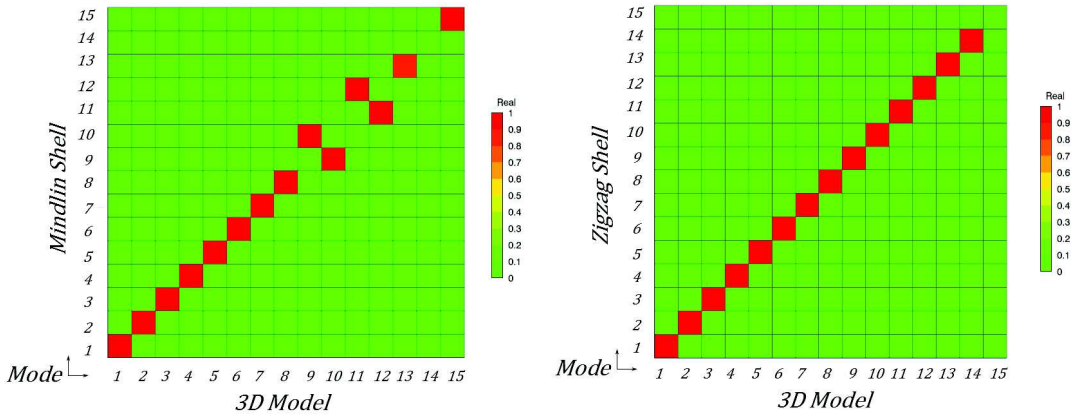

(a) Mindlin Shell vs. 3D Model **(b)** Zigzag Shell vs. 3D Model

Fig. 4.8. MAC matrices for Plate 2

Plate 1 - $[30/-45/Core/45/-30]$				
3D Model	**Mindlin Shell**	$E_{\%}$	**RZT Shell**	$E_{\%}$
1, 442.50	1, 413.28	6.60	1, 443.90	-0.32
2, 852.40	2, 826.27	3.07	2, 858.10	-0.67
3, 1383.10	3, 1237.30	10.54	3, 1393.00	-0.72
4, 1706.00	4, 1521.25	10.83	4, 1718.00	-0.70
5, 1757.40	5, 1669.08	5.03	5, 1769.00	-0.66
6, 2414.30	6, 2104.86	12.82	6, 2434.00	-0.82
7, 2528.10	7, 2134.03	15.59	7, 2567.00	-1.54
8, 2650.00	12, 2853.15	-7.67	10, 2873.00	-8.42
9, 2690.00	9, 2480.47	7.79	8, 2745.00	-2.04
10, 2791.00	8, 2295.80	17.74	9, 2824.00	-1.18
11, 3354.00	11, 2819.60	15.94	11, 3397.00	-1.31
12, 3428.00	10, 2728.14	20.42	12, 3473.00	-1.31
13, 3864.00	13, 3006.09	22.21	13, 3944.00	-2.07
14, 3923.00	14, 3121.71	20.42	14, 3997.00	-1.89
15, 4007.00	15, 3314.46	17.28	15, 4173.00	-4.14

Table 4.13. Plate 1 Eigenfrequencies and percentage error

Plate 2 - $[0/90/Core/90/0]$				
3D Model	**Mindlin Shell**	$E_{\%}$	**RZT Shell**	$E_{\%}$
1, 466.60	1, 433.44	7.11	1, 467.76	-0.25
2, 699.30	2, 687.08	1.75	2, 708.25	-1.28
3, 1464.10	3, 1304.06	10.94	3, 1472.77	-0.59
4, 1685.10	4, 1522.66	9.64	4, 1695.42	-0.61
5, 1788.50	5, 1668.11	6.68	5, 1803.30	-0.88
6, 1984.40	6, 2059.55	-3.79	6, 2059.57	-3.79
7, 2330.50	7, 2084.82	10.50	7, 2350.08	-0.88
8, 2650.30	8, 2214.98	16.43	8, 2679.82	-1.11
9, 2726.00	10, 2437.90	10.57	9, 2807.27	-2.98
10, 2804.10	9, 2354.95	16.02	10, 2835.37	-1.12
11, 3253.30	12, 2760.06	15.16	11, 3303.27	-1.54
12, 3280.10	11, 2744.95	16.32	12, 3320.57	-1.23
13, 4034.30	13, 3109.75	22.92	13, 4110.13	-1.88
14, 4070.90	14, 3213.32	21.05	14, 4139.42	-1.71
15, 4155.40	15, 3281.00	21.04	15, 4237.13	-1.97

Table 4.14. Plate 2 Eigenfrequencies and percentage error

4.5.2 Cylindrical panels

The curved panel considered is a 90° section of a cylinder of radius R=0.250 m and height H=0.50 m as shown in Fig. 4.9.

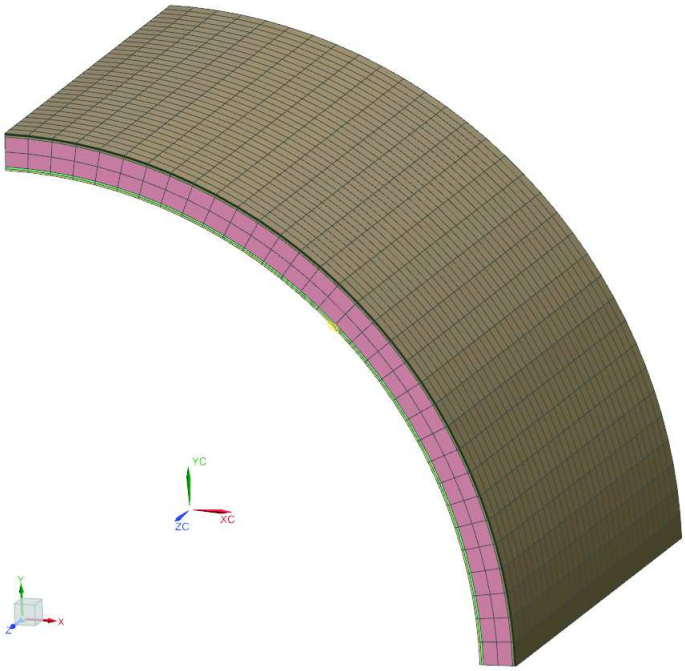

Fig. 4.9. Curved sandwich panel geometry

Material properties and layups are the same as the ones considered for the flat panels (Table 4.15). Modal analysis is performed clamping all edges. Table 4.16 shows the number of elements and DoF for the three models and Tables 4.17-4.18 report the eigenfrequencies for the two configurations. Figs. 4.10-4.11 show the MAC matrices for both panels for the pairs Mindlin Shell vs. 3D model and RZT Shell vs. 3D Model.

Stacking sequence	
Sandwich Panel 1	$[30/-45/Core/45/-30]$
Sandwich Panel 2	$[0/90/Core/90/0]$

Table 4.15. Curved panels' layups

Curved panels' number of Elements and DoF			
	3D Model	**Mindlin Shell**	**RZT Shell**
No. Elements	6144	1024	1024
No. DoF	35937	6534	9801

Table 4.16. Plates' number of elements and DoF

Panel 1 - $[30/-45/Core/45/-30]$				
3D Model	**Mindlin Shell**	$E_{\%}$	**RZT Shell**	$E_{\%}$
1, 1008.00	1, 981.06	2.67	2, 1015.62	-0.76
2, 1008.40	2, 990.02	1.82	1, 1007.04	0.13
3, 1247.60	3, 1209.23	3.08	3, 1284.04	2.92
4, 1324.20	4, 1293.46	2.32	4, 1359.94	-2.70
5, 1467.20	6, 1421.11	3.14	5, 1471.05	-0.26
6, 1470.30	5, 1415.95	3.70	6, 1478.37	-0.55
7, 1564.60	7, 1545.82	1.20	7, 1628.12	-4.06
8, 1643.60	8, 1580.76	3.82	9, 1684.33	-2.48
9, 1645.00	10, 1613.96	1.89	8, 1670.99	-1.58
10, 1659.90	9, 1585.84	4.46	11, 1730.09	-4.23
11, 1692.80	11, 1718.46	-1.52	10, 1719.34	-1.57
12, 1760.30	12, 1770.22	-0.56	12, 1818.65	-3.31
13, 1833.10	13, 1826.14	0.38	13, 1884.33	-2.79
14, 1900.70	14, 1827.69	3.84	14, 1930.62	-1.57
15, 1902.10	15, 1836.42	3.45	15, 1932.28	-1.59

Table 4.17. Panel 1 Eigenfrequencies and percentage error

Panel 2 - $[0/90/Core/90/0]$				
3D Model	**Mindlin Shell**	$E_{\%}$	**RZT Shell**	$E_{\%}$
1, 806.00	1, 784.90	2.62	1, 818.75	-1.58
2, 824.90	2, 812.77	1.47	2, 829.47	-0.55
3, 1047.00	3, 1018.77	2.70	3, 1073.65	-2.55
4, 1182.90	4, 1143.66	3.32	4, 1192.07	-0.78
5, 1205.10	5, 1158.67	3.85	6, 1253.35	-4.00
6, 1205.90	6, 1158.83	3.90	5, 1222.66	-1.39
7, 1414.30	7, 1352.58	4.36	7, 1459.10	-3.17
8, 1450.50	9, 1415.15	2.44	8, 1477.19	-1.84
9, 1479.90	8, 1409.90	4.73	9, 1558.34	-5.30
10, 1574.80	10, 1490.54	5.35	10, 1599.33	-1.56
11, 1585.40	11, 1506.32	4.99	11, 1606.06	-1.30
12, 1684.70	13, 1622.44	3.70	12, 1756.97	-4.29
13, 1695.80	12, 1608.43	5.15	14, 1800.83	-6.19
14, 1729.00	14, 1644.17	4.91	13, 1776.65	-2.76
15, 1788.30	15, 1695.70	5.18	15, 1842.98	-3.06

Table 4.18. Panel 2 Eigenfrequencies and percentage error

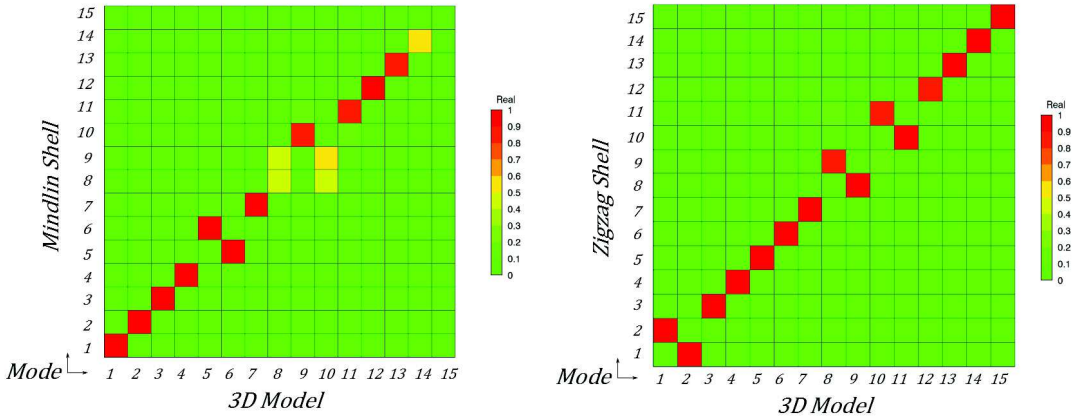

(a) Mindlin Shell vs. 3D Model **(b)** Zigzag Shell vs. 3D Model

Fig. 4.10. MAC matrices for Panel 1

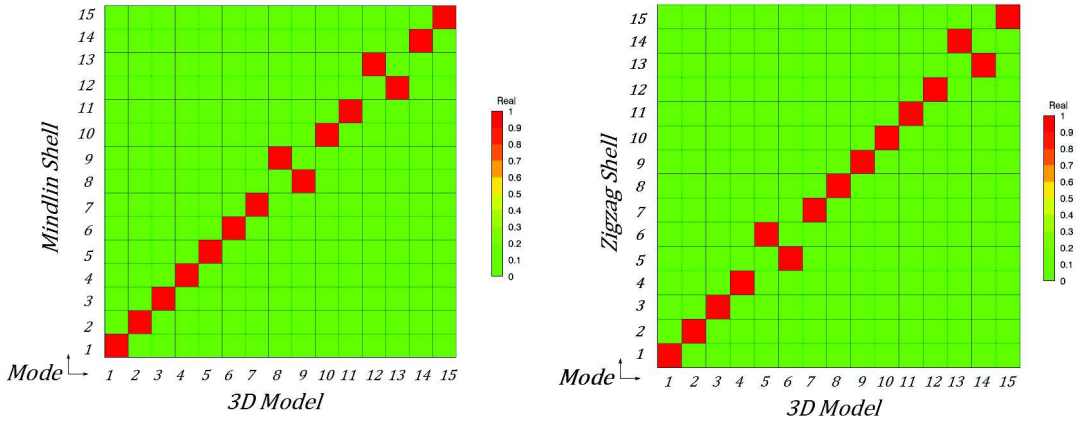

(a) Mindlin Shell vs. 3D Model **(b)** Zigzag Shell vs. 3D Model

Fig. 4.11. MAC matrices for Panel 2

4.5.3 Hemispherical panel

The last case analysed is a double-curvature geometry (Fig. 4.12) with a sandwich layup characterised by thick isotropic face sheets and a thick polymer core. The part is a 90 degrees section of a hemisphere of radius R=1 m. The face sheets are 5 mm thick and the core is 16 mm thick. Material properties are reported in Table 4.19. A

Materials' Properties			
	Young Modulus	**Shear Moduli**	**Poisson's Ratio**
Aluminium	$E = 70$ GPa	$G = 26$ GPa	$\nu = 0.35$
PVC	$E = 104$ MPa	$G = 40$ MPa	$\nu = 0.30$

Table 4.19. Hemisphere materials' properties

Mindlin shell, RZT and 3D model (Fig. 4.13) are created and compared; Table 4.20

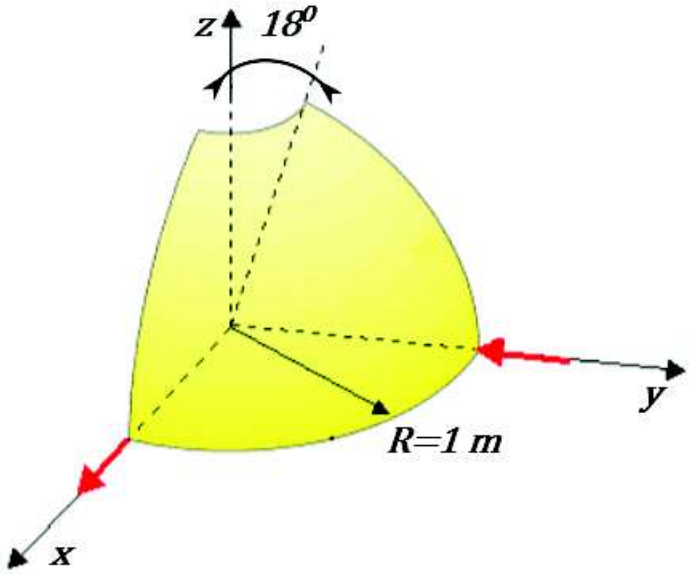

Fig. 4.12. Hemisphere geometry

gives an overview of the number of elements and degrees of freedom for each model. The comparison is done on the basis of modal analysis results, that is eigenfrequencies comparison and mode shapes correlation, assuming the 3D model as the reference. The geometry is clamped along two edges as shown in Fig. 4.13.

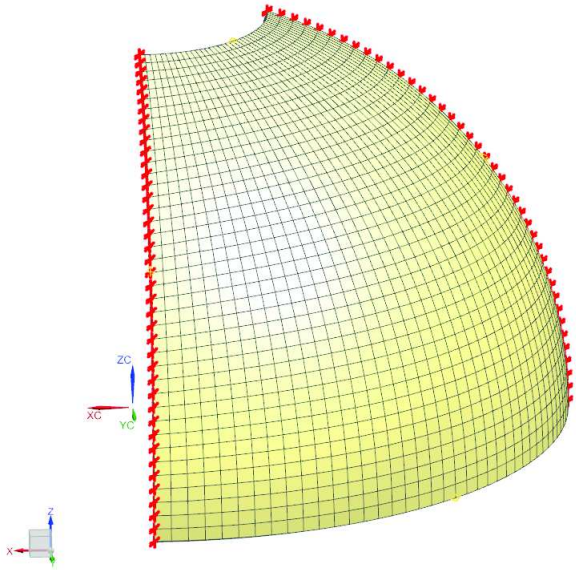

Fig. 4.13. Hemisphere mesh and boundary conditions

Curved panels' number of Elements and DoF			
	3D Model	**Mindlin Shell**	**RZT Shell**
No. Elements	4800	1600	1600
No. DoF	20172	9600	15129

Table 4.20. Plates' number of elements and DoF

Table 4.21 contains the eigenfrequencies of the hemisphere. The percentage error is calculated as in Eq.4.39.

Hemisphere panel				
3D Model	**Mindlin Shell**	$E_{\%}$	**RZT Shell**	$E_{\%}$
1, 175.83	1, 166.29	5.43	1, 173.84	1.13
2, 177.78	2, 166.70	6.23	2, 175.87	1.07
3, 295.98	3, 277.06	6.39	3, 294.35	0.55
4, 310.06	4, 283.29	8.63	4, 309.48	0.19
5, 411.55	5, 373.64	9.21	5, 413.44	-0.46
6, 446.40	6, 392.94	11.97	6, 450.20	-0.85
7, 488.72	7, 444.77	8.99	7, 484.58	0.85
8, 551.64	10, 495.96	10.09	9, 559.13	-1.94
9, 559.48	8, 473.09	15.44	8, 562.32	0.06
10, 566.20	9, 475.54	16.01	10, 563.93	0.40
11, 601.61	15, 615.72	-2.35	11, 597.27	0.72
12, 620.70	14, 614.52	1.00	12, 617.60	0.50
13, 622.79	11, 574.60	7.74	13, 618.93	0.62
14, 640.92	12, 578.26	9.78	14, 637.03	0.61
15, 647.60	13, 596.70	7.86	15, 645.20	0.37

Table 4.21. Hemisphere panel eigenfrequencies and percentage error

Fig. 4.14a-4.14b show the MAC matrices for the Mindlin and RZT shell models respectively. The percentage error and the MAC matrix show a generally improved behaviour of the RZT Shell compared to the Mindlin one. In particular, the RZT Shell converges better to the reference model, reducing the error by as much as 17% compared to the Mindlin model. In terms of mode shapes prediction, low correlation is observed for the

central modes when the RZT Shell is used. However, the corresponding modes for the Mindlin Shell appear to be missing as a zero MAC value is found. With this respect we can say that the RZT Shell has a better performance also in terms of stiffness and mass distributions' predictions.

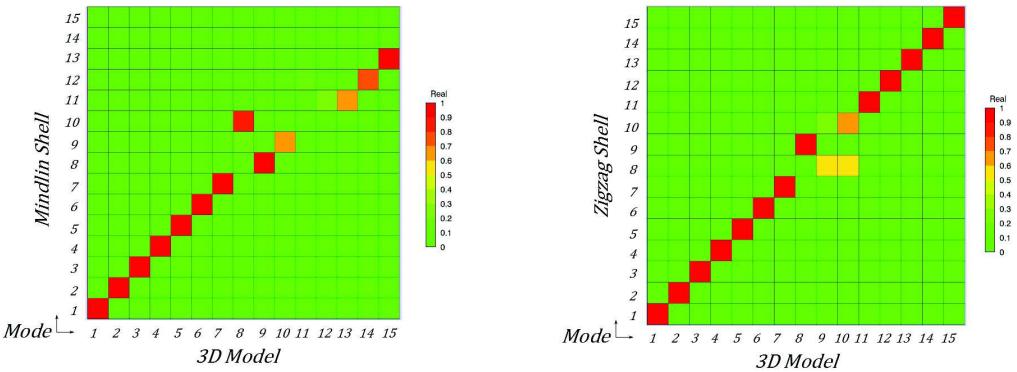

(a) Mindlin Shell vs. 3D Model **(b)** Zigzag Shell vs. 3D Model

Fig. 4.14. MAC matrices for the hemispheric panel

4.5.4 Conclusions

The above results confirm the trend observed in the previous paragraph. In the modal analysis of the sandwich plate the RZT shell performs better than the Mindlin shell, reducing the error by as much as 20%. Not only the stiffness prediction is better but also its distribution, as the MAC matrices show for both the layups chosen. In the case of the curved panels, the contribution of the zigzag function brings a slight improvement in terms of both frequencies and mode shapes for the cylindrical panel while for the hemispheric geometry we find the same trend as for the flat panels. The reason may be the geometry itself, which seems to compensate for the lower stiffness of the zigzag model. Another source of discrepancy might be the use of flat shell elements rather than curved elements. Nonetheless, the MAC matrices still show a better behaviour of the RZT shell compared to the Mindlin shell. If we look at the number of DoF used by the RZT models compared to the 3D model, the gain in computational efficiency is evident.

Chapter 5

Manufacturing processes of composite materials and simulation strategies

5.1 Overview of manufacturing technologies for composite materials

The manufacturing processes of composite materials are mainly driven by the nature of the polymer matrix [168] that is either thermoplastics or thermosets. This is due to the different behaviour they exhibit with respect to temperature and pressure.
Thermoplastics are generally *linear polymers* whose chains are held together by weak bonds such as the van der Waals'. The bonds are easily broken upon heating, the thermoplastics then behaving as viscous fluids; it is usually in this state that polymers are processed to be given the final shape [3]. Thermosets are usually obtained by mixing a resin and a hardener which react and harden either at room temperature or upon heating, forming strong covalent bonds (*curing*). The processing takes place when the material is in a liquid or soft solid state and viscosity is lower than that of thermoplastics. The resulting material contains a high number of cross-links and thermosets appear as 3D networks of molecules. The different bonds that hold together thermoplastics and thermosets are responsible for their mechanical properties: thermosets are generally stiffer than thermoplastics though the latter exhibit a higher fracture toughness. In the production of composites, thermosets are therefore preferred for structural applications where higher moduli are needed, while thermoplastics are employed in secondary applications or where energy absorption capabilities are required.

Beside the intrinsic strength of the polymeric chains, another important difference between thermosets and thermoplastics is their temperature-dependent behaviour. Both types of polymers show two distinctive temperature values at which either a phase or behaviour transition occurs: the *glass transition temperature*, T_g, and the *melting temperature*, T_m. Below T_g the polymer behaves as a rigid, glassy solid, while above it the polymer shows a rubbery behaviour. Both thermoplastics and thermosets have T_g that are higher than room temperature, unlike rubbers. The melting temperature is the temperature at which polymers melt; with this regard thermosets and thermoplastics differ significantly. Thermoplastics can be heated above the glass transition temperature and up to the melting point and then cooled again to return to the rigid glassy state. This makes the thermoplastics recyclable and therefore appealing for commercial applications. In thermosets, melting generally occurs at very high temperatures, above the *decomposition temperature* of the cured polymer: before a thermoset could melt its chemical structure is inevitably degraded and cannot be recovered any more. Characteristics temperatures for thermosets are usually higher than for thermoplastics and they do not undergo phase changes during thermal cycles; this makes them suitable for higher-temperature applications compared to thermoplastics.

The above mentioned differences directly impact on the type of manufacturing process needed to obtain the reinforced polymer. The most important parameter is the viscosity of the polymer because it controls the time necessary to proper fibres impregnation, which is essential to avoid air pockets or dry spots that compromise the final composite resistance. At typical processing temperatures, thermoplastics are highly viscous. The implications are twofold: on the one hand, higher pressures are necessary to establish the flow inside the moulding cavities, which is energetically demanding and also requires equipments with higher strength properties; on the other hand, the risk of bad fibres impregnation exists thus increasing the possibility of low quality process output. In order to overcome these issues, the processing temperature can be increased but at the same time this may lead to degradation of the polymer due to the persistent thermal load. Thermosets are less viscous at typical manufacturing temperatures which makes the process more stable and less prone to faults. In this case, however, attention has to be paid in order to keep the processing temperature below the curing temperature to prevent premature solidification.

Clearly, the type of reinforcement also plays a role in the manufacturing process setup. Reinforcements are currently available as continuous (long) fibres, fabrics, milled or chopped (short) fibres, prepregs, Bulk Moulding Compounds (BMC) and Sheet Moulding Compounds (SMC). Prepregs are made up of long fibres or fabrics bounded by a semi-cured thermoset resin; they are sold in spools or sheets and then cut in the right shape and size to create the plies. The use of prepregs is quite spread nowadays since they provide composite laminae with an already defined orientation and reinforcement

spacing, thus reducing the processing time. BMC and SMC are partially cured resins with short fibres reinforcements in the form of bulk and sheet semifinished products, respectively.
The forming processes, that is the combination of matrix and reinforcement to obtain the final shape, are usually grouped in two categories: open forming and closed forming. Many processes belong to these classes but not all of them are suitable for both thermosets and thermoplastics. Table 5.1 gives an overview of the available processes.

Manufacturing process classification		
	Open Forming	**Closed Forming**
Thermoplastics		
	Hand lay up	Injection moulding
	Robotic lay up	
	Filament winding	
Thermosets		
	Hand lay up	Compression moulding
	Spray lay up	Resin Transfer Moulding (RTM)
	Robotic lay up	Vacuum bag/Autoclave forming
	Filament winding	Cold press
	Roll-wrapping	Pultrusion

Table 5.1. Thermosets and thermoplastics processing classification

Generally speaking, open forming processes require one mould only, upon which reinforcements and matrix are applied. The mould itself can be made of wood, clay, composites or metals depending on the forming pressure, number of parts to be produced, parts' geometry. The surface in contact with the mould will generally show better finishing. In closed form two moulds are present so that both sides of the part will show good quality surface finishing. The moulds are prepared by applying a film of a releasing agent to allow the removal of the part at the end of the process. If high quality surface finishing is demanded, a gel coat is applied. Depending on the application, the gel coat can be enriched by colour pigments, fire-retardant, anti-UV agents and so on. On top of them the fibres and polymers, either separate or in semi-finished form, are placed in the mould.

In spray lay up, filament reinforcements are fed continuously to a gun and cut in pieces before being sprayed on the mould. Simultaneously, the matrix is sprayed (Fig. 5.1).

The fibres orientation will be random thus giving quasi-isotropic properties; the process continues until the desired laminate thickness is obtained. The process is low cost but so is the quality of the finished part. Moreover, the components tend to be rich in resin with an unnecessary increase in weight.

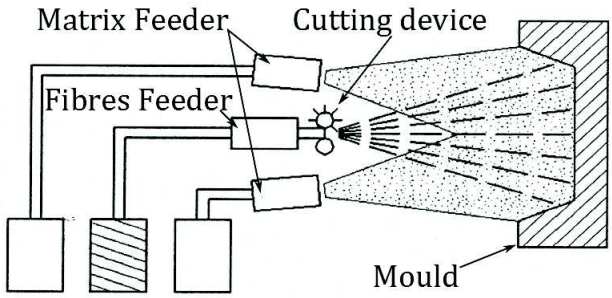

Fig. 5.1. Spray lay up scheme - *Source: Design with polymers and composites, Lecture Notes Unical*

The use of robotic arms and automated fibres/prepregs placement devices leads to a significant increase in processing speed, process repeatability, cost-efficiency. However, the process is suitable for big yet simple geometries. Deposition rates between 15 and 30 m/min can be obtained. The equipment needed is quite complex and comprises a robotic head which provides and cuts the prepregs for a system of mandrels that unroll the plies on the final geometry.

In filament winding, continuous filament reinforcements are first dip in a resin bath and then wound around an axisymmetric shape (mandrel) (Fig. 5.2). The reinforcement can be wound parallel to the axis, along the circumference or at predefined angles, which is usually preferred because it gives higher strength to the final part. The process is completely automated and the resulting components have high quality and strength thanks to the lack of joints. The only constraint is the removal of the mandrel which limits the geometries that can be processed.

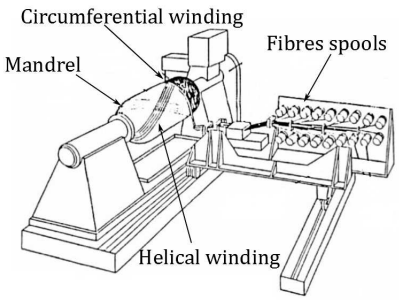

Fig. 5.2. Filament winding equipment - *Source: Design with polymers and composites, Lecture Notes Unical*

Roll-wrapping [4] is similar to filament winding as it is used to produce axisymmetric parts but in this case the mandrel is made to rotate over a prepreg which initially lays flat on a table.

Compression moulding (Fig. 5.3) is very simple and can be efficiently applied to high volume production. The process requires a mould and a punch. In between, the material is placed and forced to take the shape of the mould thanks to the pressure applied by the punch. The material is either a SMC or BMC. The low pressure version is called cold forming. Despite the conceptual simplicity of the process and its high production rate, it is usually expensive because both dies require high surface finishing and resistance to withstand the high pressures for as many cycles as possible.

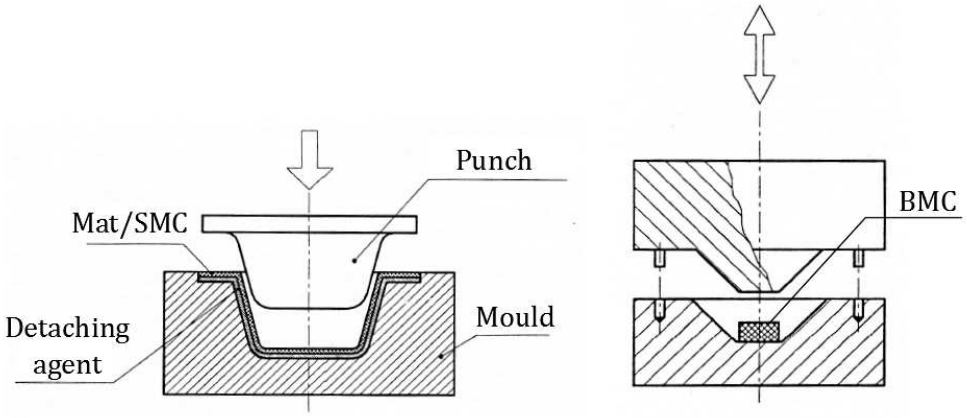

(a) Mat or SMC preform **(b)** BMC

Fig. 5.3. Compression moulding scheme - *Source: Design with polymers and composites, Lecture Notes Unical*

A variation of this process is the Resin Transfer Moulding (RTM) where the reinforcement only is placed between the dies and kept in place by appropriate clamps and application of a low pressure on the upper die. The resin is transferred into the mould at a later stage. The process can be enhanced by means of a vacuum pump which removes the air before the injection of the resin (Fig. 5.4). Hand lay up is among the first manufacturing processes for composite materials and it is still in use for the manufacturing of large components such as ship hulls. It involves extensive manual operations and therefore repeatability is not always ensured. In hand lay up pure fibres or fabrics are laid on the master form and only afterwards resin is added with the aid of rollers. The quality of the impregnation thus depends on the ability of the technician performing the task. The final curing is then favoured by the use of vacuum bags and for smaller components autoclave. Autoclave forming is the standard process for the manufacturing of high quality, high resistance components and it is therefore the preferred manufacturing process in the aerospace industry. It starts from prepregs tapes which are laid into a mould; once the lamination is complete, the mould and the laminate are inserted into a

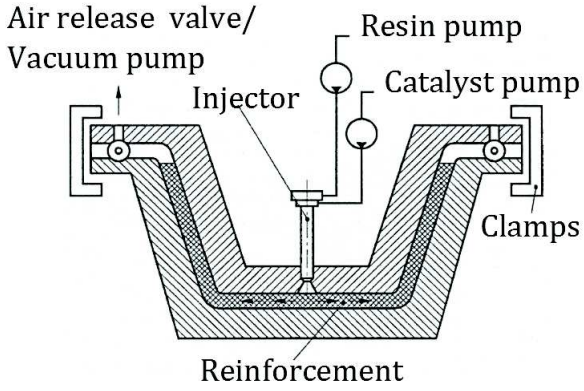

Fig. 5.4. RTM scheme - *Source: Design with polymers and composites, Lecture Notes Unical*

bag and connected to a vacuum pump. The pump is activated to remove both air and resin in excess. Curing can either take place at room temperature (Vacuum bag forming) or sped up by putting the bag into an autoclave and imposing a pressure-temperature cycle. The combined action of vacuum, pressure and temperature significantly reduces the risk of air pockets, resin excess or areas of bad adhesion between prepregs. It is however a costly process from time and energy viewpoints, and costs increase with the dimensions of the component. Pultrusion is the process employed to create open or closed profiles with constant cross-section. Only continuous filament reinforcements are used; the process starts with the unravelling of the filaments from the spools; in the dry version, the impregnation takes place in the matrix, in the wet version the fibres are dip in a resin bath before entering the dies. The dies have the twofold function of shaping the composite and curing it by means of an external go-through-oven or a heating system embedded in the dies. The cured profile is pulled by a puller and finally cut in the desired lengths. Injection moulding is the most common manufacturing process for the high-volume production of thermoplastic parts. The process is directly derived from neat polymers' injection moulding, the only difference being the dispersion of short fibres or particles in the polymer before injection. The polymer is fed to a hopper in solid state and then pushed into the mould by a rotating screw (Fig. 5.5).

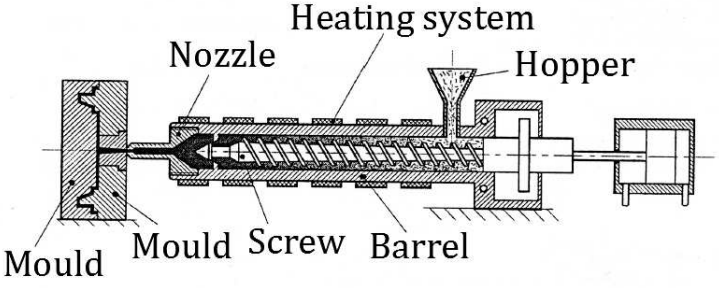

Fig. 5.5. Injection moulding equipment, Lecture Notes Unical

The shearing that develops in the barrel generates enough heat to melt the polymer which is then pushed through the injection channels and moulds by the screw. The barrel can also be equipped with a heating system to keep the reinforced polymer in a fluid state and possibly reduce viscosity. The curing will take place in the mould. The main drawbacks of this process are the long cycle time and the high cost of the equipment.

5.2 Deformation of reinforcements during hand lay up and draping operations

The manual positioning of the fibres and the often complex geometries contribute to introduce deviation from the nominal fibre orientation. A direct consequence is the variability of properties from one part to the other and the discrepancies between the nominal properties and the actual ones, which may lead to unexpected behaviours of the component during service. Hand lay up of fibres and matrix is still used for the manufacturing of big parts, but whenever possible the use of unidirectional or fabrics prepregs is preferred as it speeds up the process. Nonetheless, the lay up of semi-cured prepregs poses the same issues as the manual draping, that is variability from part to part and deviation of fibres from their nominal angle in order to follow the geometry to be draped. The latter have to do with the deformability of the prepregs which in turns depends on the possible deformation that the type of reinforcement can undergo. In unidirectional prepregs, deformations transverse to the fibres and shearing can equally occur; when two reinforcement directions are present, i.e. fabrics, only shearing is possible [169]. The shearing behaviour of fabrics is compared to that of a net of inextensible but flexible bars that can rotate where the two directions cross each other and it is referred to as *Pin-Jointed Net* (PJN) behaviour. The resistance of prepregs to compressive loading is almost null and when fibres are loaded along their principal axis they will almost instantaneously buckle. In order for the prepregs to lay on a 3D surface, out-of-plane bending, in-plane shear and/or bending occur, to which transverse deformation adds as to maintain the integrity of the tows forming the reinforcement. The result is that in case of bending, fibres on the inside, i.e. compressed, will be buckled and distorted from their nominal orientation. At macroscopic level the buckling on the inside of bending will appear as wrinkles in the lamina, while on the outside tearing may occur if the maximum allowable deformation is exceeded. The draping behaviour of prepregs is usually measured according to two main approaches. The first is simply draping 3D geometries at different difficulty levels, such as hemispheric parts. For each test a deformability limit is experimentally sought. The obvious risk is that the results are subjective and the prepregs behaviour may differ significantly on a different geometry.

The second is to perform tensile tests on the reinforcement to obtain load/displacement curves. From tensile tests of fabrics it emerged that the load in the fabric rises slowly, followed by an increase in stiffness with the increase of deformation up to a point where no more deformation is possible. The sample fabrics are loaded at ±45° to the principal fibres' direction, *bias extension test* (Fig. 5.6).

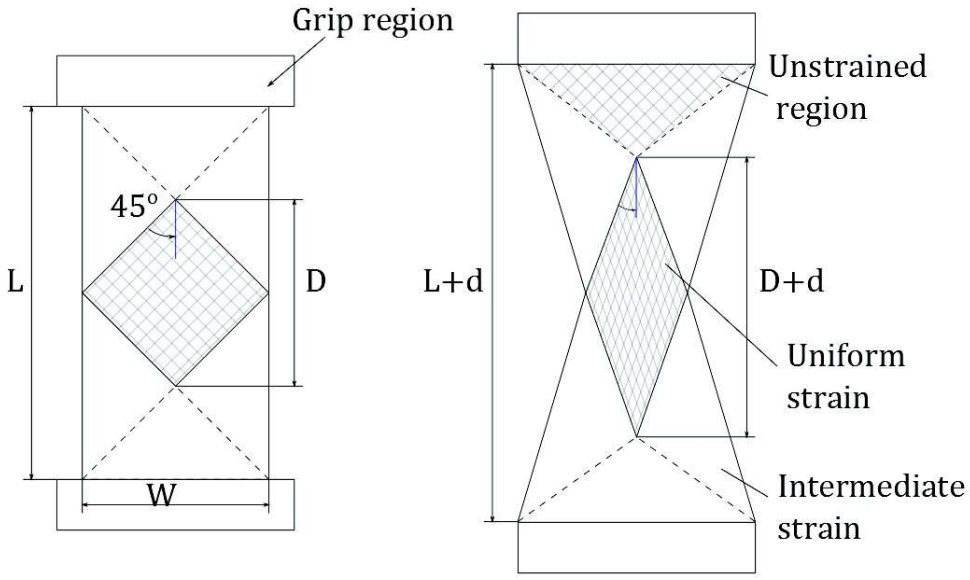

Fig. 5.6. Bias Extension Test scheme

This is why fabrics are preferred over unidirectional prepregs to drape complex geometry, even if less deformation modes are allowed. Fig. 5.6 compares fabrics and unidirectional prepregs load/displacement curve. When the prepreg is eventually applied onto the geometry, a lot of manual work is performed and laminators usually rely on self-made tools to accomplish the task. There are several ways to align the plies to each other. However, since each of the plies will have a different starting orientation and their deformations will vary accordingly to conform to the geometry, the resulting layup may vary from part to part and with respect to the ideal one. Such variability is usually not accounted for in the design process, so that the as-manufactured part will possibly differ from the designed one.

The use of CAE tools to simulate the draping process can therefore provide useful insight on how it will actually develop over the surface, allowing to define the optimal draping setup already in the design process of the part.

5.3 Homogenisation of Long Fibres Reinforced Materials: micromechanical approaches

Micromechanical approaches are a valuable tool to analytically predict unidirectional and woven reinforced materials' properties. In the framework of the draping analysis hereby performed to assess its impact on the dynamic behaviour of composite structures, micromechanical analysis constitutes the starting point. The plies' materials are built from matrix and reinforcement properties and homogenised laminae's properties are calculated using a micromechanical approach. Both stiffness and strength can be predicted starting from the RVE shown in Fig. 5.7.

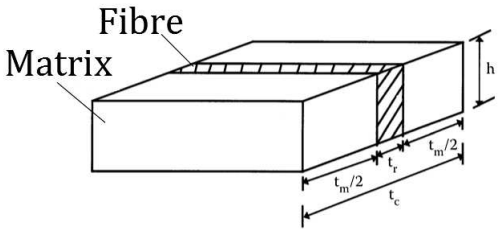

Fig. 5.7. Unidirectional fibres reinforced material RVE

Three approaches are possible [170]: strength of materials, semi-empirical and elasticity. Only the first will be discussed because it is the one that will be used in the foregoing analysis. Some assumptions and preliminary considerations are necessary. A concept that is crucial in micromechanics is that of volume fraction which defines the volumetric fraction of fibres and matrix with respect to the total volume of the composite. From volume fractions it is then possible to estimate the ply density as a function of matrix and fibres densities. The mass of the composite is defined as:

$$M_c = M_f + M_m \tag{5.1}$$

where the subscripts c, f and m stand for composite, fibres and matrix respectively. By definition, the mass of the matrix, fibres and composite is given by:

$$M_m = \rho_m v_c, \quad M_f = \rho_f v_f, \quad M_c = \rho_c v_c \tag{5.2}$$

where v are the volumes and ρ the densities. Substitution of Eqs. 5.2 in Eq. 5.1 yields:

$$\rho_c v_c = \rho_f v_f + \rho_m v_m \quad \rightarrow \quad \rho_c = \rho_f \frac{v_f}{v_c} + \rho_m \frac{v_m}{v_c} \tag{5.3}$$

The volume fractions are defined as:

$$V_f = \frac{v_f}{v_c}, \quad V_m = \frac{v_m}{v_c} \tag{5.4}$$

which substituted in 5.3 finally gives:

$$\rho_c = \rho_f V_f + \rho_m V_m. \tag{5.5}$$

In the above analysis the voids content resulting from manufacturing errors was disregarded even though it can significantly modify the proportions of matrix and fibres with impact on the stiffness and strength properties too.
To determine the four elastic constants, $E_1, E_2, G_{12}, \nu_{12}$ the RVE in Fig. 5.7 is considered. A single fibre is put between two blocks of matrix. The fibre is approximated by a rectangular block and no matrix is put on the top or bottom of the fibre. The height of fibre and matrix is the same while the respective thickness, t_f, t_m, are represented in Fig. 5.7. The area of the fibre, matrix and composite are given respectively by:

$$A_f = t_f h, \quad A_m = t_m h, \quad A_c = t_c h \tag{5.6}$$

The areas are proportional to their volume fractions so that the fibre and matrix volume fractions can also be written as:

$$V_f = \frac{A_f}{A_c} = \frac{t_f}{t_c} \quad V_m = \frac{A_m}{A_c} = \frac{t_m}{t_c} = 1 - V_f. \tag{5.7}$$

In the strength of materials approach further assumptions are made on the properties of the constituents and the composite:

- fibres and matrix are perfectly bonded;
- the fibres have equal elastic moduli, diameters and spacing among each other;
- fibres are continuous and parallel;
- matrix and fibres are isotropic and Hooke's law holds;
- the strength of the fibres is uniform;
- the composite is free of voids.

To calculate the longitudinal modulus a force F_c is applied to the RVE and it is shared by fibre and matrix according to:

$$F_c = F_m + F_f \tag{5.8}$$

It is possible to write the force components in terms of the stresses σ carried by the matrix and by the fibre:

$$F_c = \sigma_c A_c, \quad F_m = \sigma_m A_m, \quad F_c = \sigma_c A_c \tag{5.9}$$

Application of Hooke's Law allows us to write the stress-strain relationship for the fibre, the matrix and the composite:

$$\sigma_f = E_f \varepsilon_f, \quad \sigma_m - E_m \varepsilon_m, \quad \sigma_c = E_1 \varepsilon_c \tag{5.10}$$

By substituting of the last sets of equation in the force balance and recognising that the strains in the fibres, matrix and composites are all equal lead to:

$$E_1 \varepsilon_c A_c = E_f \varepsilon_f A_f + E_m \varepsilon_m A_m \quad \rightarrow \quad E_1 = E_f \frac{A_f}{A_c} + E_m \frac{A_m}{A_c}. \tag{5.11}$$

Equivalence between area and volume fractions finally gives:

$$E_1 = E_f V_f + E_m V_m \tag{5.12}$$

The same approach is followed for the transverse modulus. The load is applied transverse to the fibre so that the stress in the fibre, matrix and composite is the same, $\sigma_c = \sigma_f = \sigma_m$. The extension of the composite, however, is the sum of the elongation in the fibre and in the matrix

$$\Delta_c = \Delta_f + \Delta_m. \tag{5.13}$$

The following relations hold between strains and elongations:

$$\Delta_c = t_c \varepsilon_c, \quad \Delta_f = t_f \varepsilon_f, \quad \Delta_m = t_m \varepsilon_m, \tag{5.14}$$

Thanks to the Hooke's law we can write the strains in terms of the stress:

$$\varepsilon_c = \frac{\sigma_c}{E_2}, \quad \varepsilon_f = \frac{\sigma_f}{E_f}, \quad \varepsilon_m = \frac{\sigma_m}{E_m} \tag{5.15}$$

so that, combining and rearranging the above equations and remembering the equivalence between volume and thickness fractions, we can write the expression for the transverse modulus:

$$\frac{1}{E_2} = \frac{V_f}{E_f} + \frac{V_m}{E_m} \tag{5.16}$$

The Young modulus in the out-of-plane direction is assumed to be equal to the transverse

modulus E_2. To derive the major Poisson's ratio a load is applied along the fibre's direction and the deformation measured perpendicular to it. As shown previously, the length variation in the transverse direction is the sum of the variation in the fibre and in the matrix:

$$\delta_c = \delta_f + \delta_m \tag{5.17}$$

The equation can be rewritten as

$$t_c \varepsilon_c = t_f \varepsilon_f + t_m \varepsilon_m \tag{5.18}$$

thanks to the definition of normal strains. The Poisson's ratios for the fibres, the matrix and the composite are defined as

$$\nu_f = -\frac{\varepsilon_f^T}{\varepsilon_f^L}, \quad \nu_m = -\frac{\varepsilon_m^T}{\varepsilon_m^L}, \quad \nu_{12} = -\frac{\varepsilon_c^T}{\varepsilon_c^L}, \tag{5.19}$$

where L and T are the longitudinal and transverse direction respectively. Combination of the above equations with the volume fractions definition finally leads to

$$\nu_{12} = \nu_f V_f + \nu_m V_m \tag{5.20}$$

The in-plane shear modulus G_{12} is found starting from Eq. 5.17 where δ is now the shear strain. The shear strains read:

$$\gamma_c = \frac{\tau_c}{G_{12}}, \quad \gamma_f = \frac{\tau_f}{G_f}, \quad \gamma_m = \frac{\tau_m}{G_m} \tag{5.21}$$

Again, combining the volume fractions definition with the strains definition and their relationship within the RVE we find the sought relation:

$$\frac{1}{G_{12}} = \frac{V_f}{G_f} + \frac{V_m}{G_m}. \tag{5.22}$$

The following assumptions are made for the transverse shear moduli:

$$G_{13} = G_{12} \tag{5.23}$$

$$G_{23} = G_m. \tag{5.24}$$

The estimation of woven mechanical properties using micromechanics requires a more detailed study at the reinforcement scale because the interaction between warp and weft fibres also plays a role in the definition of their properties. Generally speaking, the points at which warp and weft cross each other constitute a location of stress concentration and

a source of friction; because of that their real behaviour will differ from the theoretical one, which usually disregards these interactions. A milestone study by Ishikawa and Chou [171, 172] considers plain weave, twill weave and harness satin reinforcements and their respective RVE. For each of them a geometric analysis at warp and weft crossing points is performed allowing a more accurate definition of the stress-strain relationship within the RVE and thus for the all lamina. Depending on the type of reinforcement different models are obtained. All of them however only provides bound for the mechanical properties. A more recent study by King et al. [173] tries to overcome the limitations of the aforementioned models accounting for some of the response mechanisms of woven reinforcements. These include:

- resistance to relative yarn rotation: it is the principal response mechanism to shear deformation;
- locking: it makes the fabric resist the deformation due to the yarns that jam against each other;
- crimp interchange: it is the mechanism by which upon loading of the fabric the yarn in one direction elongates with a reduction in the weave amplitude and an increase in wavelength while the other undergoes the opposite process.

In the present study a *laminate analogy* is used [174]. In particular, a laminate that has the same mechanical properties of a woven ply is built using as input the fibres properties in the warp and weft directions (Fig. 5.8), the matrix properties and the *balance coefficient*, k. The balance coefficient is the ratio between the amount of fibres running in the warp direction and the amount of fibres running in the weft direction.

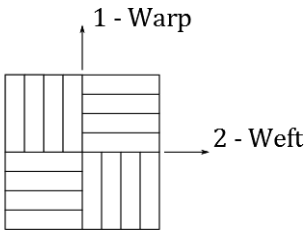

Fig. 5.8. Warp and weft directions in a woven reinforcement

To each woven ply corresponds a 3-layers laminate (Fig. 5.9). The outer plies replace the fibres in the warp direction; their thickness is equal to $k/2$ and fibres are oriented at 0°. The inner ply replaces the weft direction; it has a thickness of (1-k) and fibres oriented at 90°. Once the laminate is built, the micromechanics equations shown before are used to determine the properties of each ply.

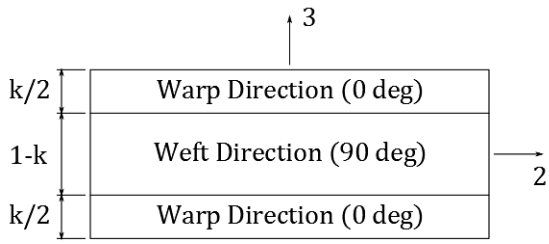

Fig. 5.9. Laminate analogy scheme

In addition to the equations shown above, the transverse Poisson's ratios are also calculated. By definition

$$\nu_{13} = -\frac{\varepsilon_3}{\varepsilon_1}. \tag{5.25}$$

If the load is applied along direction 1, than the strain along direction 3 is given by:

$$\varepsilon_3 = -\left(\nu_{12}^{wp} k + \nu_m (1-k)\right) \varepsilon_1 \tag{5.26}$$

where *wp* stands for warp ply. Application of the definition in Eq. 5.25 gives

$$\nu_{13} = k\nu_{12}^{wp} + (1-k)\nu_m \tag{5.27}$$

and using a similar approach for the 2-3 plane we eventually find

$$\nu_{23} = (1-k)\nu_{12}^{wp} + k\nu_m \tag{5.28}$$

5.4 Numerical methods for draping

Different numerical methods exist to simulate the draping of unidirectional or woven reinforcements. The draping simulations are performed in Siemens NX and we will therefore refer to the models herein available. In general, the draping simulation will depend on several factors [175]:

- the geometry to be draped;
- the presence of cutting lines, *darts*, to avoid wrinkling or tearing of the lamina;
- the start point and the draping direction;

All these factors are influencing parameters also in the real draping process. In particular the last two show dependence from the geometry. In draping, geometries are usually

referred to as *developable* or *undevelopable*. Developable surfaces can be flattened in a unique manner and without distortion. Undevelopable surfaces, on the other hand, do not have a unique flat pattern and undergo distortions during flattening. Examples of developable and non-developable surfaces are shown in Fig. 5.10 (Source: NX 10 User's Guide). It is important to mention that fibres' distortion is equally important in developable and undevlopable surface when it comes to the laminate mechanical properties.

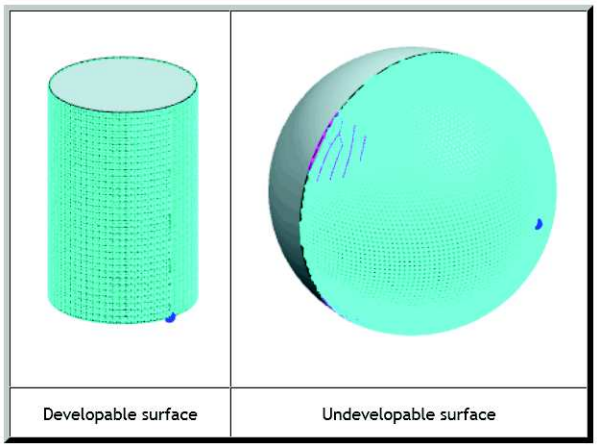

Fig. 5.10. Examples of devolapable and undevelopable surfaces

5.4.1 Draping of unidirectional reinforcements

Three draping solvers are available for unidirectional fibres, *unidirectional*, *projection* and *spine-based*. The unidirectional solver accounts for the sliding of fibres with respect to one another during draping but keeping the spacing unaltered. The user select a starting point, which identifies the point of first contact between the lamina and the tooling surface, and a direction along which the plies are draped and to which lamination angles are referred. The angle between the fibres in their undeformed state and their deformed state is the shear angle which measure the fibres slippage. The value of the shear angle is internally compared to the ply's *lock angle* which is an inherent property of the material and it indicates the maximum slippage that the lamina can withstand before tearing. The areas of the component for which the lock angle is exceeded are highlighted. This information can then be used to change the draping starting point or to introduce darts on the part in order to avoid tearing defects during manufacturing. As it will be shown later, however, changes in the draping starting point will change the final mechanical properties of the part and therefore a trade-off has to be found. The shear angle information is available for each element of the mesh. This information is then used to compute the laminate stiffness matrix on an element-by-element basis. In

practice, the part is divided in *zones* which share the same material properties. The subdivision in zones is handled by the structural solver NX Nastran by means of a composite specific entry, *PCOMP card* [176]. The PCOMP card is a handy way of defining laminates' properties (Fig. 5.11). It contains all the information regarding the plies' thickness, material, lamination angle and total number of plies in the stack up.

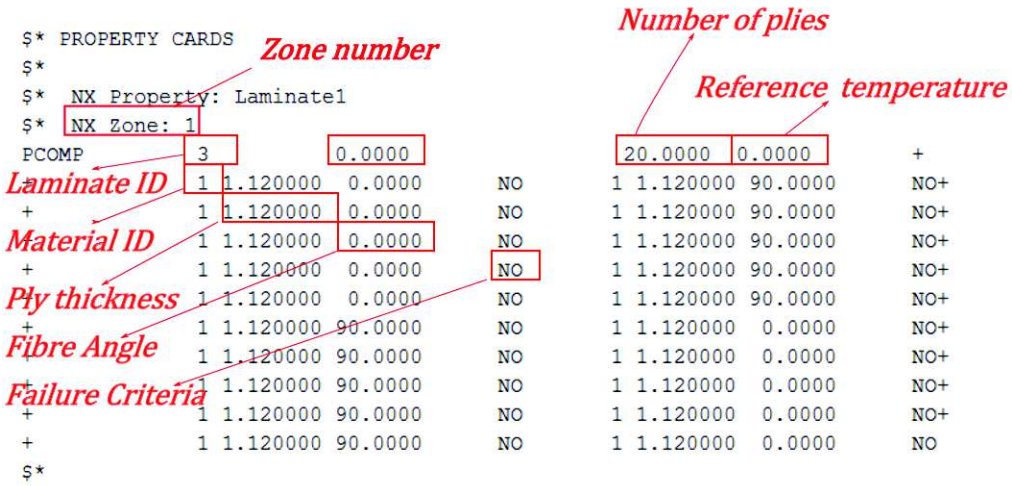

Fig. 5.11. Sample PCOMP card for a 20 layer, cross-ply laminate

When distortions occur during the draping, the angle in the PCOMP card will differ from the one specified during the laminate definition proportionally to the shear angle. It is this new orientation angle that is used in the framework of the CLT to determine the stiffness matrix of the laminate.

The projection method does not account for fibre distortions due to draping. It is the approach most commonly used in FE solvers with no draping capabilities. During projection the material orientation is merely projected onto each element of the mesh. The material orientation is used to orient orthotropic and anisotropic material's properties and it does not depend on the mesh. The material orientation itself becomes the reference 0° direction to which the lamination angles are referred; the element-by-element fibre orientation is obtained from rotating the material orientation vector around the normal of the elements by an angle equal to the ply angle.

The spine-based mapping method [1] uses a user-defines curve, *spine*, as guiding line during draping. Fig. 5.12 shows the working principle of the spine-based mapping. The frame to which plies' angle are referred moves along the spine so that the principal direction is always tangent to it and the secondary direction is at 90°. This method is meant to accurately reproduce the manual draping operation over curved surfaces, in which deformation of the plies occur in order to accommodate the plies to the geometry. The element-by-element ply angle will then be computed and transferred to the structural solver following the same procedure as the unidirectional solver.

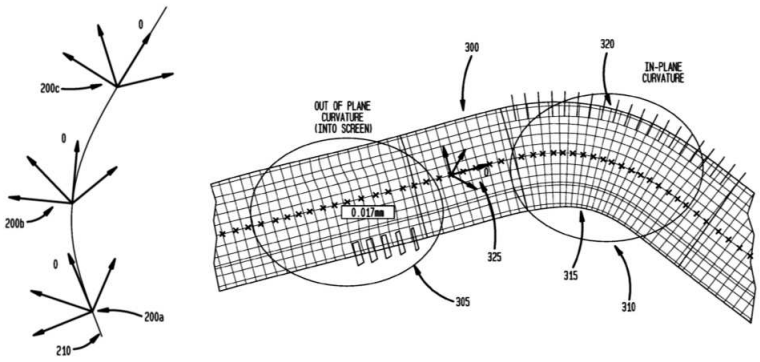

Fig. 5.12. Spine-based draping method [1]

5.4.2 Draping of woven reinforcements

The draping simulations of woven reinforcements can follow two different approaches, the *mechanical* and the *geometric* (or *kinematic*) approach [177, 178]. Fabrics' draping has ∞^2 solutions because it depends on two parameters, namely the starting point (or impact point) and the initial orientation of warp and weft. The mechanical draping is the most accurate of the two, taking into account the interaction of the lamina with the tooling surface, the interaction between warp and weft, the friction between the plies and the tooling surface and the friction among the plies. Cherouat [179] solves the problem using a finite difference method. Despite being highly refined and accurate, these models are usually computationally expensive and require the knowledge of several processing parameters. As a consequence, they are not appealing in the framework of an integrated process, in which manufacturing simulations and finite element analysis are coupled in the design stage to optimise the mechanical properties of the component. Less accurate, but far more easy to handle from the numerical point of view, is the geometric draping which only requires the geometry of the tool surface. The kinematic draping is based on the *fishnet* method, schematically reproduced in Fig. 5.13 [179]. Warp and weft are assumed inextensible and defined by the local coordinate system (ξ, η). The mesh of the tooling surface, T_Σ, is known and the fabric is divided in quadrilateral areas, fabric mesh T^F, delimited by the warp and the weft. The problem of draping is that of calculating the displacement of each warp-weft intersection point connecting with a point on the tool surface such that the edge of the corresponding mesh, T_F^Σ, on the surface is kept, that is the fibres are inextensible. In order to do so, the following algorithm is followed:

1. associate the starting point on the tooling surface;
2. compute the warp nodes T_F^Σ, $\alpha - nodes$, starting from the impact point and associated with the nodes (ξ, η_0);

3. compute the weft nodes of T_F^{Σ}, $\beta - nodes$, starting from the impact point and associated with the nodes (ξ_0, η);

4. compute cell-by-cell all the other mesh points of T_F^{Σ} associated with the nodes (ξ, η_0) and (ξ_0, η)

All the nodes of T_F^{Σ} associated with the $\alpha - nodes$ of T^F lay along the geodesic line emanating from the impact point. The $\beta - nodes$ are located using different algorithms.

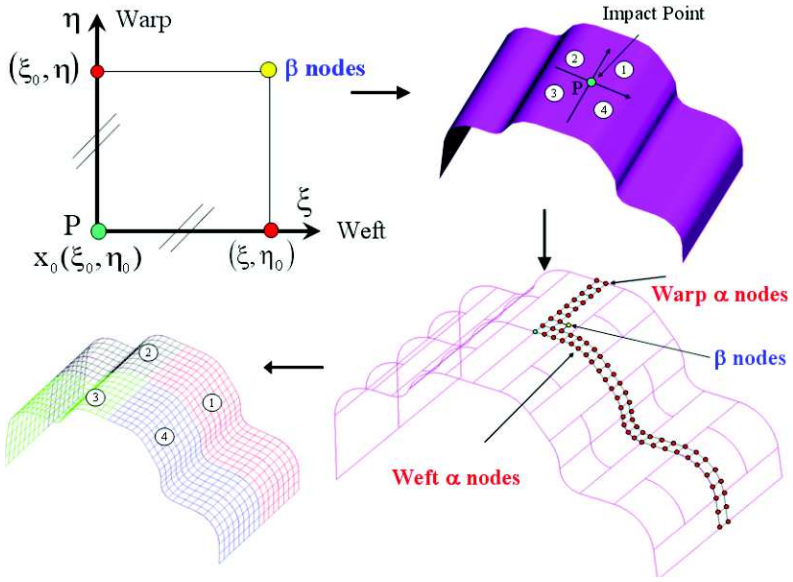

Fig. 5.13. Fishnet draping scheme

The main shortcoming of this approach is clearly that the draping results do not depend on the actual fabric configuration, that is the type of weave which ultimately affects the deformability of the fabric. On the other hand, it resembles quite well manual draping operations but not the automated one since static boundary conditions cannot be applied [180–183]. Despite some limitations, the kinematic draping is considered more robust than the mechanical one, especially when complex geometries are involved, offering a good compromise between accuracy and computational efforts [184].
In Siemens NX 10.0 a dedicated woven solver based on the aforementioned geometric approach is available. The initial angle between the warp and the weft is 90° and it is specified by selecting the warp and weft alignment. The deformations that take place during the draping are accounted for by changing the angle between the warp and the weft. The distortion is a shearing one to comply with the fibres' inextensibility assumptions.

5.5 Impact of local fibre orientation on eigenfrequencies and mode shapes: application cases

The rationale behind the use of draping simulations in combination with finite element analysis is to propose an integrated design method which accounts for the fibres' distortion during the manufacturing which causes a mismatch between the designed and the as-manufactured part. The ideal design loop would look like Fig. 5.14. In order to quantify the impact that the manufacturing has on the final components' properties, modal analysis simulations are run on a unidirectional fibres reinforced component; full application of the loop is proposed on an automotive component using a woven fabric reinforcement and finally the RZT Shell element proposed in the previous chapter is used in combination with draping simulations on a double curvature laminated sandwich.

5.5.1 Unidirectional reinforcement

The draping methods for long continuous reinforcement were tested on a double curvature reinforcement structures [185], namely a stringer, for aeronautic applications. In order to evaluate how draping, and therefore properties, change with a change in the starting point, two origins were selected, one on the short arm and one on the long arm of the stringer. Fig. 5.15 shows the origins location and the spine definition. The draping methods used in this case are the unidirectional and the spine based.

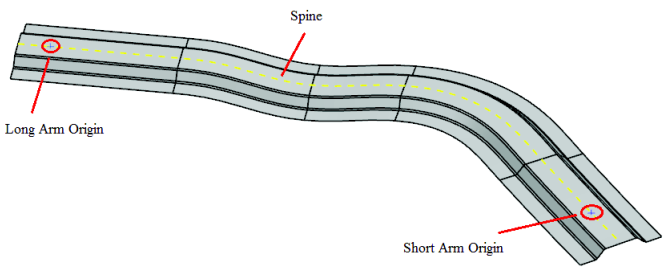

Fig. 5.15. Origins location and spine definition

The material properties are reported in Table 5.2 [186].

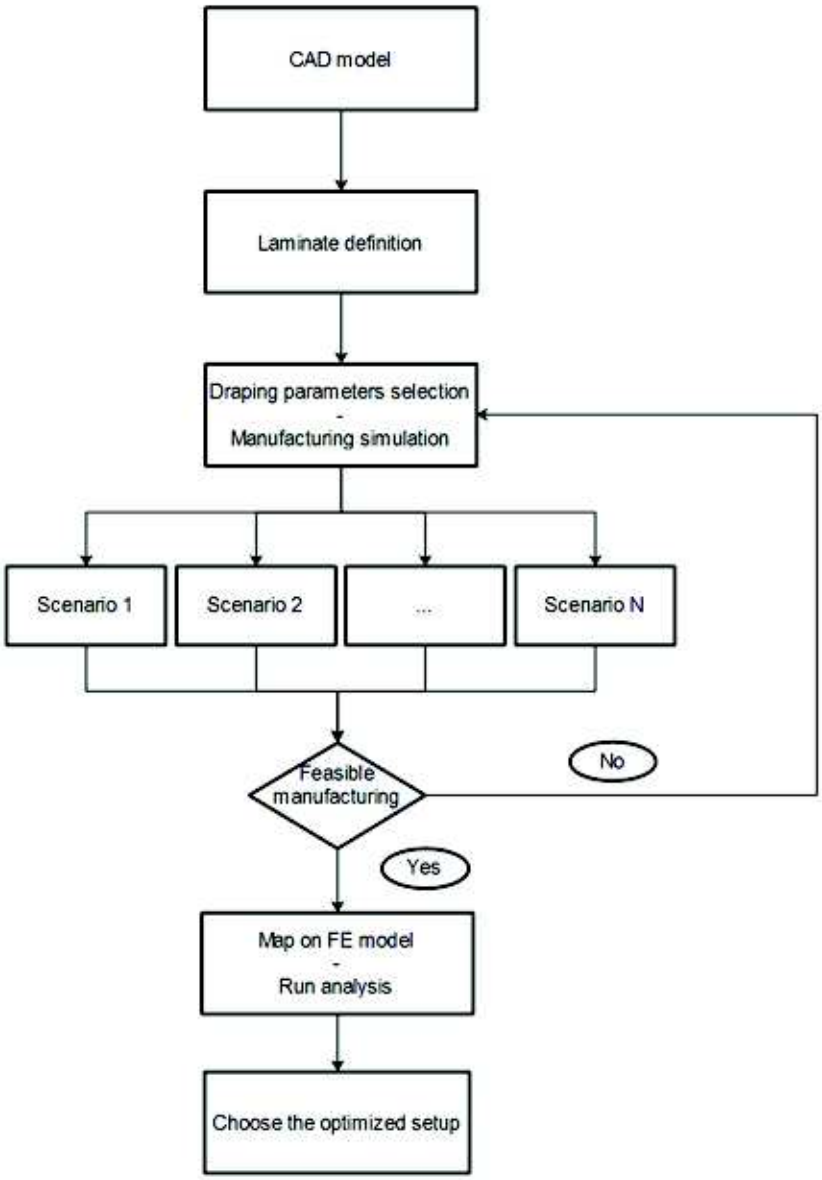

Fig. 5.14. Manufacturing simulation/FE integration loop

T700 GC - Carbon/Epoxy			
E_1 [GPa]	126.8	G_{12} [GPa]	4.2
E_2 [GPa]	8.4	ρ [kg/m^3]	1520
ν_{12}	0.309	V_f	50

Table 5.2. Stringer's material properties

The laminate contains 30 plies arranged according to the following layup:

$$[0/-45/45/-45/90/-45/0/45/90/-45/45/90/-45/0/45/90/-45/0]_s\,.$$

The results of the different draping methods can be observed in in Fig. 5.16.

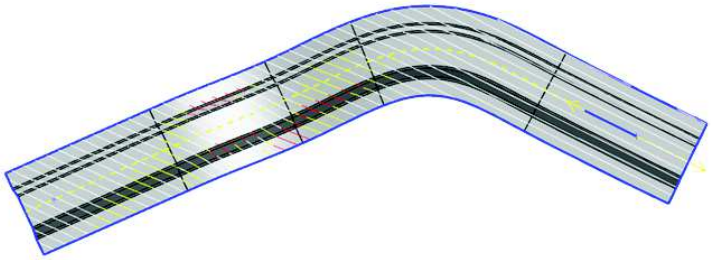

(a) Unidirectional draping - Short arm origin

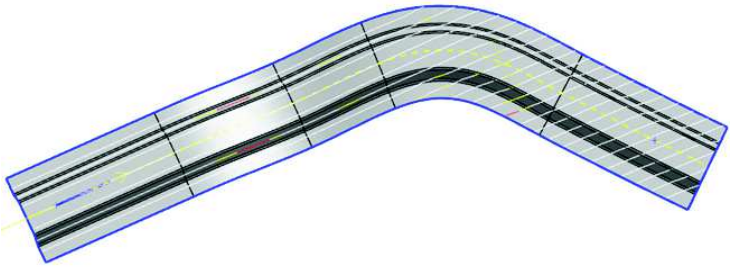

(b) Unidirectional draping - Long arm origin

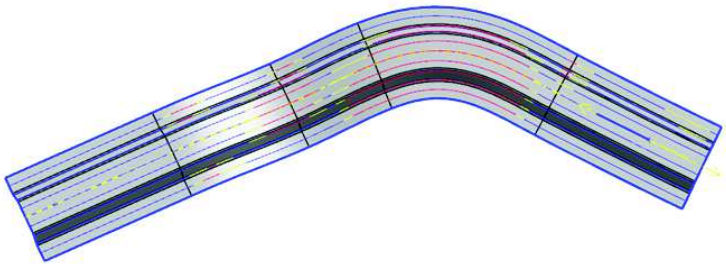

(c) Spine-based draping

Fig. 5.16. Draping results

Comparison of Fig. 5.16a and Fig. 5.16b shows how fibres alignment is affected by the change in starting point. From Fig. 5.16c it clearly appears that a change in origin using the spine-based method does not affect the final result; this is further confirmed by Fig. 5.17 which shows how the frame to which angles are referred moves along the spine. The three scenarios described above are now compared by means of modal analysis simulations. Free-free conditions are considered and modes calculated in the range 1-1000 Hz. The effect of the local fibre orientation can be appreciated through the difference in eigenfrequencies and MAC numbers. The comparison is done as follows:

- long arm origin vs short arm origin;

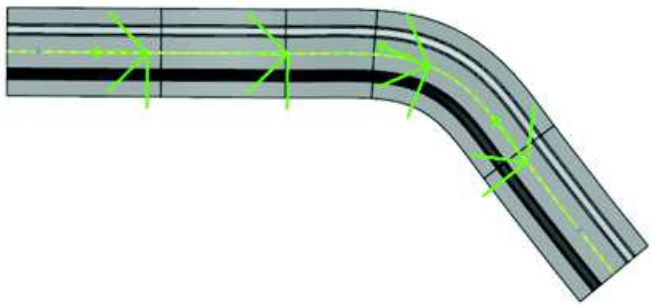

Fig. 5.17. Moving frame along the spine

- spine-based vs short arm origin.

Tables 5.3-5.4 report the eigenfrequencies for the two configurations and the relative percentage difference, calculated as:

$$\Delta_{\%} = \frac{\text{Long arm} - \text{Short arm}}{\text{Long arm}} \cdot 100; \quad \Delta_{\%} = \frac{\text{Spine} - \text{Short arm}}{\text{Long arm}} \cdot 100 \tag{5.29}$$

Long arm [Hz]	**Short arm [Hz]**	$\Delta_{\%}$
1, 93.2	1, 82.3	11.7
2, 109.1	2, 109.4	-0.3
3, 166.2	3, 162.3	2.3
4, 189.6	4, 180.1	5.0
5, 310.9	5, 300.0	3.5
6, 350.9	7, 381.7	-1.2
7, 405.1	7, 381.7	5.8
8, 454.2	8, 452.1	0.5
9, 585.6	9, 544.5	7.0
10, 665.3	11, 666.2	-1.8
11, 709.3	10, 677.3	6.1
12, 834.4	13, 795.8	-2.3
13, 863.0	12, 853.6	7.8
14, 956.7	14, 910.6	4.8
15, 997.7		

Table 5.3. Eigenfrequencies for the Long arm and the Short arm origin stringer

In the first case, only the first mode differs for more than 10%, even though the difference in absolute values is significant, especially at higher frequencies. In particular the 15^{th}

Spine [Hz]	**Short [Hz]**	$\Delta_{\%}$
1, 49.7	1, 82.3	-65.6
2, 81.3	2, 109.4	-34.6
3, 128.8	3, 162.3	-26.0
4, 162.0	4, 180.1	-11.2
5, 284.8	5, 300.0	-5.3
6, 327.1	7, 381.7	-16.7
7, 368.4	6, 355.2	3.6
8, 407.8	8, 452.1	-10.9
9, 514.1	9, 544.5	-5.9
10, 552.2		
11, 571.6		
12, 632.4	10, 666.2	-5.3
13, 652.1	11, 677.3	-3.9
14, 818.2	12, 795.8	2.7
15, 831.9	13, 853.6	-2.6
16, 896.7		
17, 952.3	14, 910.6	4.4

Table 5.4. Eigenfrequencies for the Spine-based and the Short arm origin stringer

mode for the Short arm origin stringer occurs above 1000 Hz, highlighting the different stiffness of the parts. On the other hand, the correlation matrix in Fig. 5.18 highlights the different stiffness distribution along the stringer due to the different draping origin. Poor correlation is already observed at low mode number and it worsens as frequency increases. A more detailed investigation on the mode shapes revealed that the modes showing lower MAC number were characterised by torsion-bending coupling. Despite the coupling being expected due to the non-symmetric geometry, it appears that the distortion of the fibres worsens this condition by acting on the mechanical properties distribution. The difference between the spine-based and the short arm origin stringer is even higher, the spine-based stringer being less stiff. Fig. 5.16c shows how a 0° ply looks like when draped along the spine. However, most of the plies will have a 45° angle. The main deformation mechanism is bending, with the bending axis orthogonal to the spine. The fibre orientation resulting from the spine-based method does not offer sufficient stiffness to this loading condition. On the other hand, when the plies are draped using the unidirectional method, starting from the short arm, the 45° plies turns to be orthogonal to the bending axis offering in this configuration maximum resistance to bending. Analysis of the MAC matrix (Fig. 5.19) confirms the non-negligible difference between the two parts which, in spite of sharing the same layup, appear to be almost completely non-correlated in their as-manufactured configurations.

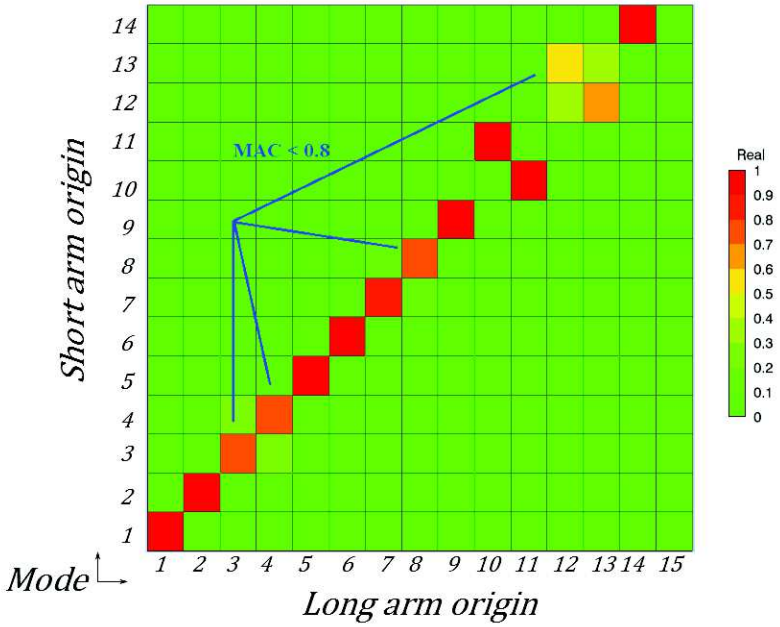

Fig. 5.18. Long arm origin vs. Short arm origin

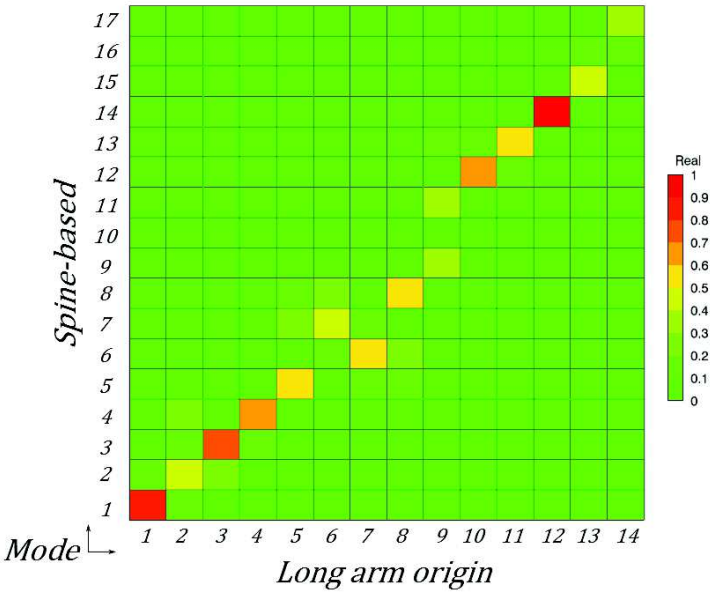

Fig. 5.19. Short arm origin vs. spine-based

5.5.2 Woven reinforcement

The woven reinforcement draping methods were tested on a full scale automotive component, namely a B-pillar reinforcement structure (Fig. 5.20), for which the use of fabrics rather than unidirectional fibres is justified by the need to withstand impact loads. The woven material properties are derived from the constituents' properties as explained in the previous section. The matrix is an epoxy resin and the fabric is made by carbon yarns. Their properties are reported in Table 5.5. Different values of balance coefficients

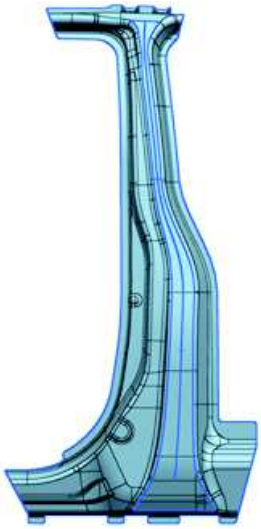

Fig. 5.20. B-pillar geometry

	Carbon yarns	**Epoxy resin**
E_1 [MPa]	238000	2400
$E_2 = E_3$ [MPa]	28000	–
$\nu_{12} = \nu_{13} = \nu_{23}$	0.348	0.3
G_{12} [MPa]	91538	990
$G_{13} = G_{23}$ [MPa]	10769	–
ρ [kg/m^3]	1810	1250

Table 5.5. Carbon yarns and epoxy matrix properties

are chosen giving birth to the following woven properties:

	Fabric k=1	**Fabric k=1/2**	**Fabric k=1/4**
E_1 [kPa]	$7.233 \cdot 10^7$	$4.992 \cdot 10^7$	$3.872 \cdot 10^7$
E_2 [kPa]	$7.233 \cdot 10^7$	$9.472 \cdot 10^7$	$1.059 \cdot 10^8$
E_3 [kPa]	$2.400 \cdot 10^6$	$2.400 \cdot 10^6$	$2.400 \cdot 10^6$
ν_{12} [kPa]	0.023240	0.017744	0.015868
ν_{13} [kPa]	0.313920	0.309280	0.306960
ν_{23} [kPa]	0313920	0.318560	0.320880
G_{12} [kPa]	$2.322 \cdot 10^6$	$2.322 \cdot 10^6$	$2.322 \cdot 10^6$
G_{13} [kPa]	$1.023 \cdot 10^6$	$9.767 \cdot 10^5$	$9.687 \cdot 10^5$
G_{23} [kPa]	$1.159 \cdot 10^6$	$1.361 \cdot 10^6$	$1.492 \cdot 10^6$
ρ [kg/m^3]	1.575	1.575	1.575

Table 5.6. Woven properties variation with balance coefficient k

The process shown in Fig. 5.14 is applied. The approach is still of the black metal type so mere replacement of steel is performed. The criterion used is mass reduction keeping the maximum deflection of the part equal to that of the same component made of steel. The part is fixed on the upper and lower surfaces (Fig. 5.21a) in order to simulate real constraining conditions and a uniform load of 10kN is applied in the area highlighted in Fig. 5.21b. Under these conditions the steel B-pillar shows a maximum deflection $\delta = 14.27mm$. The same deflection is obtained with the following lamination sequence:

$$[(0/90)_2/ \pm 45/0/90/0/ \mp 45/90/\bar{0}]_s$$

Five different draping origins/alignment combinations are identified on the part (Fig. 5.22). The impact of the draping origin choice is shown for the k=1 woven in Fig. 5.23. The above results show a close relation between the draping origin and the deflection. In particular, when draping origin is point A2, the part fails to comply with maximum deflection requirements while choice of point A1, B and C1 either bring a higher safety factor or room for further weight reduction.

The draped component is compared to the one in which fibres' distortion is not accounted for. Static analysis is again performed, this time for a fixed draping origin and at varying balance coefficient. Point A2 is chosen because it showed the highest deflection. It is in fact worth investigating the difference in stiffness between the as-manufactured part and the component obtained by simply projecting the fibres orientation on the geometry, as failure to do so can lead to over- or under-estimation of stiffness with dangerous consequences. Table 5.7 shows the results.

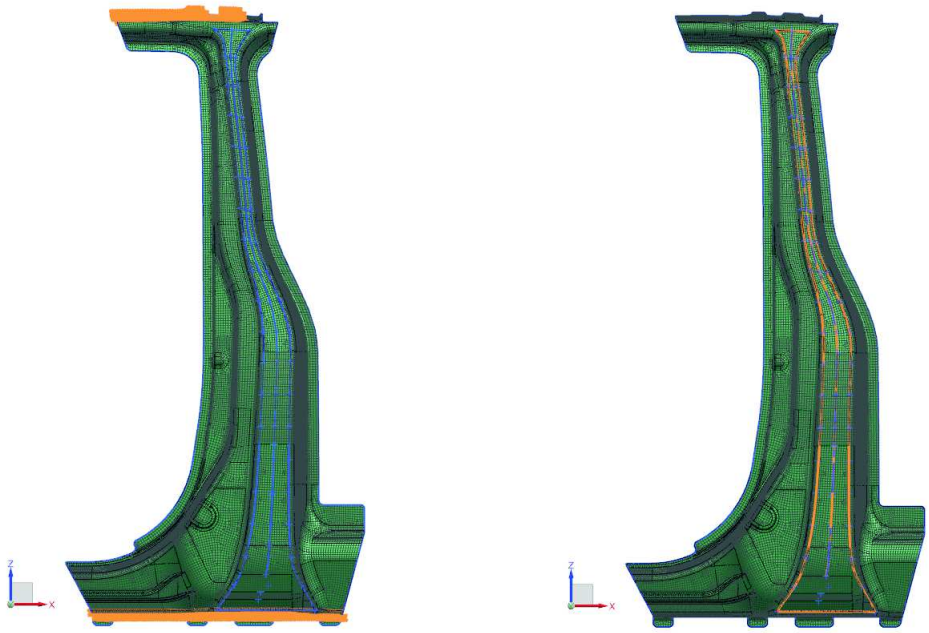

(a) Clamps location **(b)** Load application region

Fig. 5.21. Boundary conditions

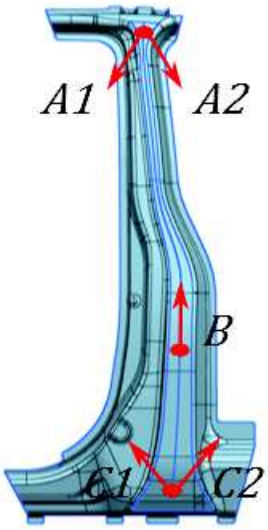

Fig. 5.22. Location of draping origins

	Kinematic draping	**Projection**
Woven k=1	16.48	10.83
Woven k=1/2	18.43	10.79
Woven k=1/4	19.75	10.76

Table 5.7. Kinematic draping vs. Projection - Origin= A2, varying balance coefficient k

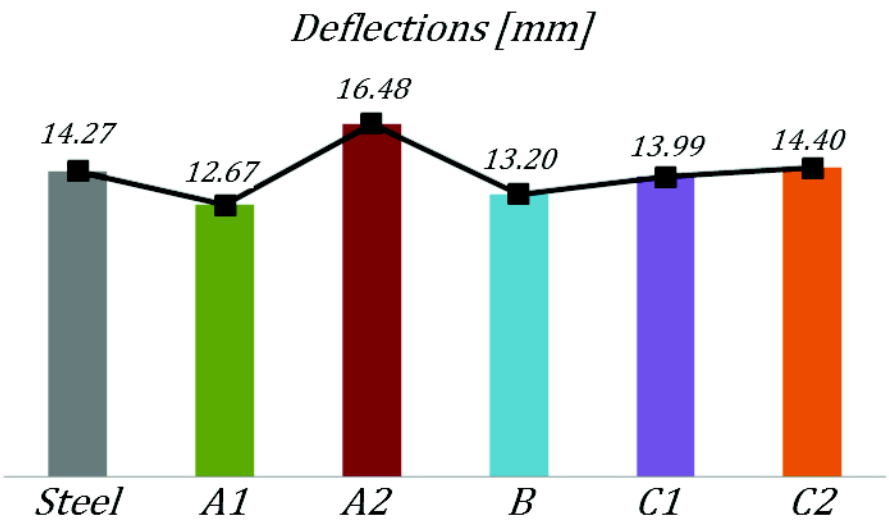

Fig. 5.23. Deflection values for k=1 and varying draping origin

It is apparent that the projection method significantly overestimates the stiffness of the component and it is not fully capable of taking into account imbalances in the woven structure.

Finally, a similar comparison is performed on a dynamic basis, comparing eigenfrequencies and mode shapes. Tables 5.8-5.10 report the eigenfrequency values for the three woven materials (k=1, k=1/2, k=1/4); Fig. 5.24 shows the MAC matrices correlating the draped component to the projected one for all the three woven structures; in the figure R stands for the reference model, in this case the projected component, and W stands for the working model which is the draped model. The relative percentage difference is calculated as

$$\Delta_{\%} = \frac{\text{Kinematic draping} - \text{Projection}}{\text{Kinematic draping}} \cdot 100 \tag{5.30}$$

Mode no	**Kinematic draping [Hz]**	**Projection**	$\Delta_{\%}$
1	112.5	141.2	20.2
2	120.8	157.5	23.6
3	184.2	225.7	18.7
4	209.9	248.9	15.2
5	276.0	343.3	20.0
6	283.4	351.2	19.8
7	314.6	400.9	21.8
8	374.9	468.3	20.4
9	400.6	532.8	25.1
10	460.3	571.2	19.6

Table 5.8. Woven k=1 eigenfrequencies

Mode no	**Kinematic draping [Hz]**	**Projection**	$\Delta_{\%}$
1	105.4	141.0.2	25.2
2	114.5	157.9	27.5
3	173.9	226.2	23.1
4	188.4	247.9	24.0
5	258.5	344.5	25.0
6	266.1	352.4	24.5
7	295.6	401.7	26.4
8	353.3	469.8	24.8
9	375.5	534.1	29.7
10	432.4	572.0	24.4

Table 5.9. Woven k=1/2 eigenfrequencies

Mode no	**Kinematic draping [Hz]**	**Projection**	$E_{\%}$
1	101.2	141.0	28.2
2	110.7	158.1	30.0
3	167.9	226.6	25.9
4	175.9	247.5	28.9
5	248.3	345.2	28.1
6	256.0	353.3	27.5
7	284.6	402.3	29.3
8	340.3	470.7	27.7
9	360.9	534.9	32.5
10	415.5	572.8	27.5

Table 5.10. Woven k=1/4 eigenfrequencies

Analysis of the MAC matrices shows that poor correlation is observed for the first two modes and for the central modes, quite consistently for all the woven structures with a slight worsening for the case *k=1/4*. It appears that the less balanced model is the most sensitive to draping conditions. The MAC results confirms the relevant discrepancy in material properties prediction between the two different approaches.

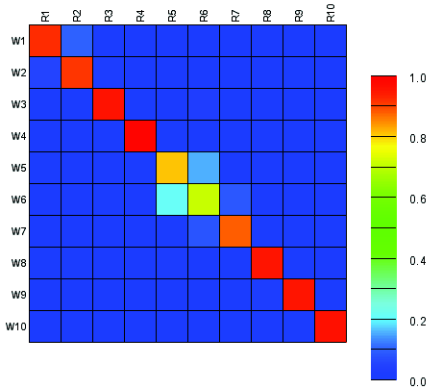

(a) Woven k=1 - Kinematic draping vs Projection

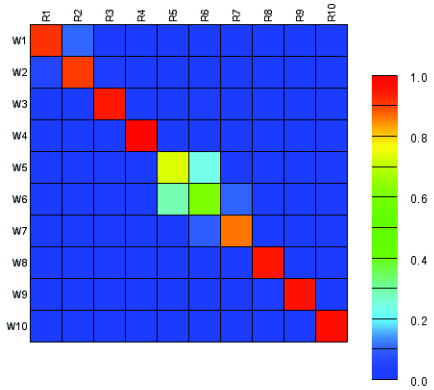

(b) Woven k=1/2 - Kinematic draping vs Projection

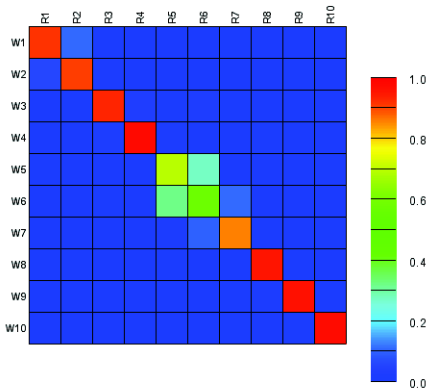

(c) Woven k=11/4 - Kinematic draping vs Projection

Fig. 5.24. MAC matrices

5.5.3 A Zigzag-Draping coupling case

The draping simulations were also coupled to the RZT Shell element to understand primarily whether the Zigzag theory can be coupled to the manufacturing simulations and if the coupling has beneficial effects. The geometry tested is the hemispherical panel tested in Chapter 4. The Aluminium face sheets were replaced by two Carbon/Epoxy laminates with the following lamination scheme:

$$0/90/0/90/0/PVCcore/0/90/0/90/0$$

and the core is made of PVC (for material properties refer to Table 4.10). Fig. 5.25 shows the mesh and the boundary conditions.

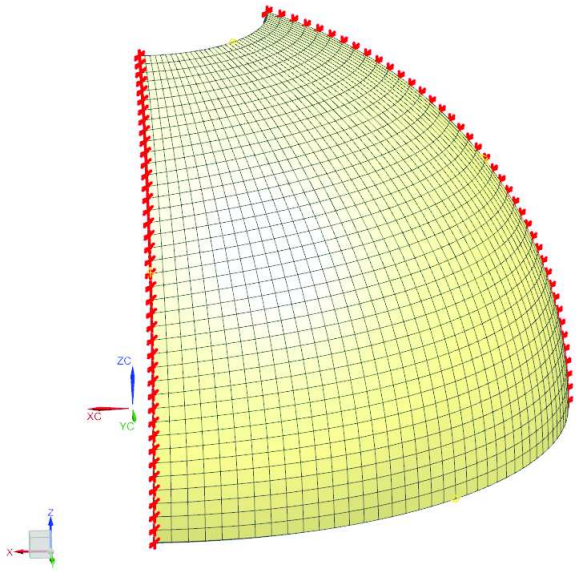

Fig. 5.25. Hemisphere mesh and boundary conditions

Modal analysis is performed and the RZT Shell results are compared to a refined 3D model and a Mindlin shell model. The RZT and the Mindlin models are created in Samcef which has inherent draping capabilities, developed on purpose for unidirectional reinforced materials. Consistency in orientation is ensured between the models by choosing the corresponding draping method for the 3D model, here assumed as the reference. Table 5.11 reports the first 15 natural frequencies and the MAC matrices for the Mindlin shell and the Zigzag shell vs the 3D model are reported in Fig. 5.26. As usual the relative percentage difference was calculated as:

$$E_{\%} = \frac{3DModel - 2DModel}{3DModel} \cdot 100 \tag{5.31}$$

being the 3D Model assumed as reference.

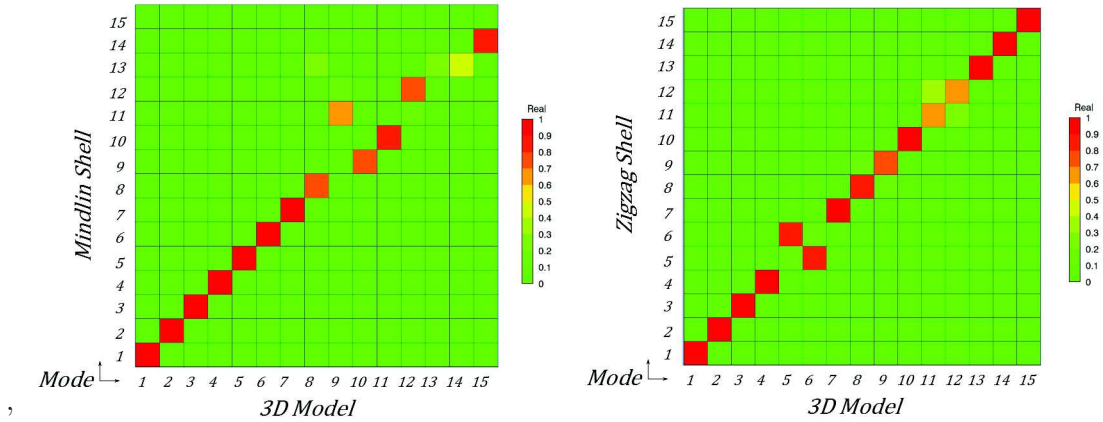

(a) 3D Model vs Minldin Shell **(b)** 3D Model vs Zigzag Shell

Fig. 5.26. MAC matrices

3D Model [Hz]	**Mindlin Shell**	$E_{\%}$	**RZT Shell**	$E_{\%}$
1, 160.32	1, 153.30	4.38	1, 158.72	1.00
2, 180.48	2, 169.12	6.29	2, 178.21	1.26
3, 284.11	3, 267.66	5.79	3, 282.91	0.42
4, 318.03	4, 290.98	8.51	4, 316.50	0.48
5, 422.99	5, 381.10	9.90	6, 425.29	-0.54
6, 423.11	6, 397.63	6.02	5, 422.16	0.22
7, 461.19	7, 430.30	6.70	7, 457.32	0.84
8, 496.04	8, 459.4	7.39	8, 492.97	0.62
9, 500.73	11, 495.96	0.95	9, 498.04	0.54
10, 508.95	9, 473.47	6.97	10, 506.42	0.50
11, 517.35	10, 482.89	6.66	11, 516.29	0.20
12, 522.20	12, 506.17	3.07	12, 525.04	-0.54
13, 537.49	15, 528.05	1.76	13, 535.13	0.44
14, 550.40	13, 507.27	7.84	14, 550.41	0.00
15, 573.93	14, 511.88	10.81	15, 574.14	-0.04

Table 5.11. Hemispheric panel eigenfrequencies

The MAC results show that the Mindlin shell, despite being coupled with the draping data, is delivering worse results than the RZT Shell, not only in terms of eigenfrequencies but also in terms of mode shapes. In fact, higher modes show a poor correlation compared to the corresponding modes predicted by the RZT Shell.

5.5.4 Conclusions

The test cases analysed show how the use of draping simulations in the design and validation process brings valuable information on the mechanical properties and behaviour of the as-manufactured part. Different draping solvers resemble different draping operations and they should be chosen accordingly in order to obtain reliable results. The information obtained can be effectively used to tailor the manufacturing process to the desired component's behaviour, optimal material choice and processing parameters. In spite of still requiring some iterations, the process is effective and the manufacturing-FE analysis integration could be further enhanced. The coupling between the RZT Shell and the draping simulations is also encouraging and it provides additional accuracy to the analysis.

Conclusions

The main objective of the research hereby presented was to propose a numerical technique for the linear dynamic analysis of composites and sandwich structures. The analysis focused on finite element methods and the problem was tackled on two fronts: on the modelling side, by extending the zigzag theory approach to the dynamic domain with inclusion of damping; on the procedural side by proposing a design method which accounts for possible deviations from nominal lamination scheme due to the manufacturing processes to tailor dynamic properties of laminated components.

In the first chapters, it has been proved that the use of a zigzag function, namely the Refined Zigzag Theory proposed by Tessler, brings significant improvements with respect to the Timoshenko theory for beams and the Mindlin theory for plates and shells. Not only is the accuracy of the RZT comparable to that of a full 3D model but also the computational effort required for the solution of the equation of motion is significantly reduced. Free vibration analysis was performed to compare different modelling approaches, i.e. Timoshenko and Mindlin theories, the RZT and 3D modelling, as eigenfrequencies provide direct information on the mass and stiffness of the system and the mode shapes on their distribution. The analysis of mode shapes proved particularly useful to assess the contribution of the zigzag degrees of freedom to the response of the structure. Its addition has a beneficial effect on the MAC values over the entire frequency range considered. The increase of degrees of freedom by one in the case of beams, two in the case of plates and three in the case of shells seems therefore justified by the improved accuracy obtained. Moreover, despite the higher number of unknowns, the RZT models remain less expensive than 3D models. The gain in cost is twofold: on the one hand, multilayer structures are condensed in one layer only, thanks to the equivalent single layer approach on which the RZT is based; this allows a faster modelling in the very first place, since only one physical layer has to be modelled while the stack up is defined by means of a list, which specifies layers' thickness, orientation and position in the stack up. The other gain is obviously related to the lower number of equations to solve, as discussed above.

To the author knowledge the use of RZT-based finite elements for the calculation of the forced and damped response of sandwiches and laminates has been done for the first time. The tests, only performed for beam structures, gave encouraging results, once again proving the better performance of the RZT over standard theories. In the attempt to keep the computational cost of the simulations low, the complex modulus approach was employed for the damped response calculation of beams. Remarkable improvements were obtained with respect to the Timoshenko theory and the same results as the reference 3D model are almost perfectly achieved.

The conclusions that can be drawn based on the extensive analyses performed is that the RZT is able to reproduce the physical behaviour of the laminated structures and it confirms that the main dissipation mechanism in viscoelastic materials, such as the cores of sandwiches, is indeed shearing. The RZT itself bases its zigzag function on the shear stiffness of the layers and their thickness. Other studies in the past proved that the amount of damping that can be achieved depends on the shear properties of the viscoelastic materials and their relative thickness in the layup [140]. The additional flexibility added to the model by the zigzag degree of freedom and the correspondent account of the shear properties and relative layers' thickness gives in the end an accurate representation of the physical phenomena taking place within the laminate. Nonetheless, the theory presents some limitations for a particular class of structures with viscoelastic treatments, that is when the viscoelastic layer is applied on a free surface and it is not constrained. In these cases the RZT still predicts a variation in the slope of the axial displacement distribution due to the properties mismatch with respect to the preceding or successive stiffer layer. As a matter of fact, such variation in slope does not occur, as predicted by the elasticity solution because the deformation of an unconstrained soft layer will be driven by the deformation of the adjacent stiff layer. In these cases the RZT not always showed a consistent behaviour. In the extreme case of a stiff core with two soft face sheets, the RZT did not predict any slope variation as one would expect from the elasticity solution. In the simpler case of a beam with only one soft layer on the top free surface, it predicted the variation in slope and logical conditions were added to the finite element formulation to reproduce correctly the 3D and elasticity results. These discrepancies represent a limit for the RZT in reproducing these particular cases. This limitation may come from the formulation of the theory itself. It is worth to remember that the RZT is based on the assumption that the mismatch of material properties at layers' interface induces transverse shear deformations within the structure. Therefore, only shear properties are accounted for in the formulation of the zigzag function. This means that, whenever two layers have the same shear modulus, the zigzag function will show no slope variation even though all the other material properties differ. Other studies [97], however, formulated the through-the-thickness function as depending on

the longitudinal, transverse and shear moduli such that the variation in material properties was thoroughly considered. However, the formulations so obtained are far more complicated and require higher numerical efforts. The above considerations reopen the discussion on the zigzag formulation itself, which was put aside in the recent years after the proposition of the RZT. It would be worth investigating which is the contribution of each material modulus to the zigzag effect whenever one of these changes from one layer to the other.

In the last chapter of the dissertation the current design with composite material approach has been reviewed and integrated with the manufacturing process simulations for continuous fibres reinforced materials. The rationale behind it is that often the manufactured part differs from the designed one due to the defects and modifications intervened during the manufacturing. The analyses on a numerical model based on the nominal designs not only lose their usefulness but may also be misleading. The main interest was on the dynamic behaviour of composite components to understand how the deviation from nominal fibre angle affect the natural frequencies and the mode shapes of the structures. The results show that it actually plays a role. Continuous reinforcements leave extensive processing freedom to the operator executing the task. This is due to the inherent deformability of prepregs that are deformed during the draping process to adapt to the geometry. However, the amount of manual work involved in the process makes it prone to a high degree of variability from one part to the other and, most important, with respect to nominal designs. Fortunately, the manufacturing simulation tools enable the designer to simulate different draping methods at an early stage. The impact they have on the dynamic properties of laminated components is significant as the MAC values for the stringer show. Same behaviour is found for the woven reinforced B-pillar. In the latter case, the newly proposed design method which integrates the manufacturing simulations is applied, from static to dynamic analyses. The results for different draping origin-orientation combination and different types of material highlight that a manufacturing-wise design approach allows for further improvements not only on the mechanical properties side but also on the mass and weight one, which is one of the main drivers in composite design.
The results, despite being encouraging, posed other questions on the process, its results and their use and interpretation. As in every engineering field, the design process requires several iterations before getting to the final, or desired results. A possible way to improve the process is to create a proper multi-objective optimisation loop that takes into account the parameters most relevant to the application. As far as it concerns the interpretation of results, it is worth to remember that the entire analysis was only performed numerically. Their validation, despite possible, would involve an extensive

experimental campaign and statistical analysis due to the variability of the real manufacturing process. If on the one hand this constituted an hindrance, on the other hand it represented an additional application field. The process outlined in the last chapter of the thesis could in fact be used in the framework of uncertainty analysis.
Finally, an application linking the two aspects of the research work was shown. Even though at a preliminary stage, it proved the suitability of the zigzag function in combination with the manufacturing simulation. Again, experimental validation would pose the same issues as before but nonetheless the numerical results confirmed the validity of the theory and its applicability, though the aforementioned limitations still hold.

The general conclusion that can be drawn from the current research work is that theories and methods meant for isotropic materials cannot be used with the same level of confidence for composites and sandwiches. The analysis of multilayer structures requires more refined theories and tools in order to face the increased complexity of the materials' structure. Two effects in particular were studied and eventually combined in an efficient way, showing that it is possible to increase the accuracy of the modelling and simulations at a reasonable computational cost. The investigation performed is self-contained but it opens interesting scenarios. First of all, the use of the Zigzag function could be extended to the analysis of damping of sandwich with frequency-dependent properties. The expected outcome is an increased accuracy in the representation of shearing phenomena causing energy dissipation as already shown in the forced response of the beam with constant loss factors. The use of manufacturing simulations in the design and analysis of laminated components naturally extends to the study of structural uncertainties and optimisation processes. All of the above research fields could finally found a meeting point in the detailed analysis of damping as a function of local fibre orientation in order to optimise composites and laminated sandwich structures for dynamic applications.

Bibliography

[1] S. Luby, J.A. Grape, E.K. Hoff, and R.S. Flory. Spine-based rosette and simulation in fiber-composite materials, 2013. US Patent App. 13/782,031.

[2] L.A. Carlsson and G.A. Kardomateas. *Structural and Failure Mechanics of Sandwich Composites*. Springer, 2011.

[3] M.F. Ashby and D.R.H. Jones. *Engineering Materials 2 - An Introduction to Microstructures, Processing and Design*. Butterworth-Heinemann, 3rd edition, 2006.

[4] R.F. Gibson. *Principle of Composite Material Mechanics*. CRC Press, 3rd edition, 2012.

[5] Z. Hashin. Analysis of Composite Materials. *Journal of Applied Mechanics*, 50(3):481–505, 1983.

[6] C.C. Chamis and G.P. Sendeckyj. Critique on theories predicting thermoelastic properties of fibrous composites. *Journal of Composite Materials*, 2(3):332–358, 1968.

[7] R.M. Christensen. *Mechanics of Composite Materials*. John Wiley & Sons, New York, 1979.

[8] J.C. Halpin. *Primer on Composite Materials–Analysis (rev.)*. Technomic Publishing Co., Lancaster, 1984.

[9] Department of Defense United States of America. *Composite Materials Handbook Volume 2. Polymer Matrix Composites Materials Properties*. 2002.

[10] D.A. Hopkins and C.C. Chamis. A unique set of micromechanics equations for high temperature metal matrix composites. Technical report, NASA, 1985.

[11] J.J. Caruso and C.C. Chamis. Assessment of simplified composite micromechanics using three-dimensional finite-element analysis. *Journal of Composite Technology and Research*, 8, 1986.

[12] A. Spencer. The Transverse ModuH of Fibre-Composite Material. *Composites Science and Technology*, 27:93–109, 1986.

[13] E. Mitsoulis. Fountain flow of pseudoplastic and viscoplastic fluids. *Journal of Non-Newtonian Fluid Mechanics*, 165:45–55, 2010.

[14] K. Sivakumar, N.G.R. Iyengar, and D. Kalyanmoy. Optimum design of laminated composite plates undergoing large amplitude oscillations. *Applied Composite Materials*, 6:87–98, 1999.

[15] S. Kalpakjian and S. Schmid. *Manufacturing Processes for Engineering Materials*. Prentice Hall, 5th edition, 2008.

[16] E.W. Kuenzi. Mechanical Properties of Aluminum Honeycomb Cores. Technical report, United States Department of Agriculture - Forest Service, 1962.

[17] C.C. Foo, G.B. Chai, and L.K. Seah. Mechanical properties of Nomex material and Nomex honeycomb structure. *Composite Structures*, 80:588–594, 2007.

[18] Hexcel Composites. Honeycomb Attributes and Properties. pages 1–40, 2000.

[19] J.C. Gerdeen and R.A.L Rorrer. *Engineering design with Polymers and Composites*. CRC Press, 2nd edition, 2011.

[20] J.N. Reddy. *Mechanics of Laminated Composite Plates and Shells: Theory and Analysis*. Springer, 2nd edition, 2003.

[21] M. Hyer. *Stress Analysis of Fiber-Reinforced Composite Materials*. McGraw-Hill, 1998.

[22] Y Stavsky. On the general theory of heterogeneous aeolotropic plates(deflection theory established for bending and stretching of elastic anisotropic plates with material heterogeneity). *Aeronautical Quarterly*, 15:29–38, 1964.

[23] S.G. Lekhnitskii. *Anisotropic plates*. Air Force Systems Command - Foreign Technology Division, 1969.

[24] S. Timoshenko and S. Woinowsky-Kreiger. *Theory of Plates and Shells*. McGraw-Hill, 2nd edition, 1959.

[25] O.O. Ochoa and J.N. Reddy. *Finite Element Analysis of Composite Laminates*. Kluwer Academic Publishers, 1992.

[26] SP Tlmoshenko. On the correction factor for shear of the differential equation for transverse vibrations of prismatic bar. *Philosophical Magazine*, 6(41):295, 1921.

[27] R.D. Mindlin. Influence of rotatory inertia and shear on flexural motions of isotropic, elastic plates. *Journal of Applied Mechanics*, 18:31–38, 1951.

[28] E. Reissner. The effect of transverse shear deformation on the bending of elastic plates. *Journal of Applied Mechanics*, 12:A69–A76, 1945.

[29] J.L. Mantari, A.S. Oktem, and C. Guedes Soares. Static and dynamic analysis of laminated composite and sandwich plates and shells by using a new higher-order shear deformation theory. *Composite Structures*, 94:37–49, 2011.

[30] H. Matsunaga. Assessment of a global higher-order deformation theory for laminated composite and sandwich plates. *Composite Structures*, 56:279–291, 2002.

[31] A.G. Radu and A. Chattopadhyay. Dynamic stability analysis of composite plates including delaminations using a higher order theory and transformation matrix approach. *International Journal of Solids and Structures*, 39:1949–1965, 2002.

[32] P. Subramanian. Dynamic analysis of laminated composite beams using higher order theories and finite elements. *Composite Structures*, 73:342–353, 2006.

[33] N. Grover, B.N. Singh, and D.K. Maiti. Analytical and finite element modeling of laminated composite and sandwich plates: An assessment of a new shear deformation theory for free vibration response. *International Journal of Mechanical Sciences*, 67:89–99, 2013.

[34] H. Nguyen-Xuan, C.H. Thai, and T. Nguyen-Thoi. Isogeometric finite element analysis of composite sandwich plates using a higher order shear deformation theory. *Composites Part B: Engineering*, 55:558–574, 2013.

[35] M. Levinson. A new rectangular beam theory. *Journal of Sound and Vibration*, 74(1):81–87, 1981.

[36] J.N. Reddy. A generalization of two dimensional theories of laminated composite plates. *Communications in Applied Numerical Methods*, 3:173–180, 1987.

[37] K.N. Cho, C.W. Bert, and A.G. Striz. Free vibrations of laminated rectangular plates analyzed by higher order individual-layer theory. *Journal of Sound and Vibration*, 145(3):429–442, 1991.

[38] C.M. Mota Soares, C.A. Mota Soares, and V.M. Franco Correia. Multiple eigenvalue optimization of composite structures using discrete third order displacement models. *Composite Structures*, 38(1-4):99–110, May 1997.

[39] T. Kant and B.S. Manjunatha. Higher-order theories for symmetric and unsymmetric fiber reinforced composite beams with C 0 finite elements. *Finite Elements in Analysis and Design*, 6:303–320, 1990.

[40] K. Swaminathan, S.S. Patil, M.S. Nataraja, and K.S. Mahabaleswara. Bending of sandwich plates with anti-symmetric angle-ply face sheets – Analytical evaluation of higher order refined computational models. *Composite Structures*, 75:114–120, 2006.

[41] A. Chakrabarti, A.H. Sheikh, M. Griffith, and D.J. Oehlers. Analysis of composite beams with partial shear interactions using a higher order beam theory. *Engineering Structures*, 36:283–291, 2012.

[42] J.N. Reddy. A Refined Shear Deformation Theory for the Analysis of Laminated Plates. Technical report, Virginia Polytechnic Institute and State University, 1986.

[43] T. Kant and B.S. Manjunatha. Refined theories for composite and sandwich beams with C 0 finite elements. *Computers & structures*, 33(3):755–764, 1989.

[44] N.J. Pagano. Exact Solutions for Composite Laminates in Cylindrical Bending. *Journal of Composite Materials*, 3(3):398–411, 1969.

[45] N.J. Pagano and S.J. Hatfield. Elastic behavior of multilayered bidirectional composites. *AIAA Journal*, 10(7):931–933, 1972.

[46] N.J. Pagano. Stress fields in composite laminates. *International Journal of Solids and Structures*, 14:385–400, 1978.

[47] N.J. Pagano. Free edge stress fields in composite laminates. *International Journal of Solids and Structures*, 14:401–406, 1978.

[48] E. Carrera. Cz0 Requirements - models for the two dimensional analysis of multilayered structures. *Composite Structures*, 37(3/4):373–383, 1997.

[49] E. Carrera. Theories and finite elements for multilayered, anisotropic, composite plates and shells. *Archives of Computational Methods in Engineering*, 9(2):87–140, 2002.

[50] A.K. Noor and W.S. Burton. Stress and free vibration analyses of multilayered composite plates. *Composite Structures*, 11:183–204, 1989.

[51] P. Gaudenzi, R. Barboni, and A. Mannini. A finite element evaluation of single-layer and multi-layer theories for the analysis of laminated plates. *Composite Structures*, 30:427–440, 1995.

[52] E. Carrera. Mixed layer-wise models for multilayered plates analysis. *Composite Structures*, 43:57–70, 1998.

[53] E. Carrera and H. Krause. An investigation of non-linear dynamics of multilayered plates accounting for C_z^0 requirements. *Computers & Structures*, 69(4):473–486, 1998.

[54] B. Brank and E. Carrera. Multilayered shell finite element with interlaminar continuous shear stresses: a refinement of the Reissner–Mindlin formulation. *International Journal for Numerical Methods in Engineering*, 48:843–874, 2000.

[55] M. Ćetković and D. Vuksanović. Bending, free vibrations and buckling of laminated composite and sandwich plates using a layerwise displacement model. *Composite Structures*, 88:219–227, 2009.

[56] L. Demasi. Partially Layer Wise advanced Zig Zag and HSDT models based on the Generalized Unified Formulation. *Engineering Structures*, 53:63–91, 2013.

[57] J.N. Reddy. On refined computational models of composite laminates. *International Journal for Numerical Methods in Engineering*, 27:361–382, 1989.

[58] J.N. Reddy. An evaluation of equivalent-single-layer and layerwise theories of composite laminates. *Composite Structures*, 25:21–35, 1993.

[59] E. Carrera. Layer-wise mixed models for accurate vibrations analysis of multilayered plates. *Journal of Applied Mechanics*, 65:820–828, 1998.

[60] S. Kapuria and N. Alam. Efficient layerwise finite element model for dynamic analysis of laminated piezoelectric beams. *Computer Methods in Applied Mechanics and Engineering*, 195:2742–2760, 2006.

[61] H. Murakami. Laminated composite plate theory with improved in-plane responses. *Journal of Applied Mechanics*, 53:661–666, 1986.

[62] K.M. Rao and H.-R. Meyer-Piening. Analysis of thick laminated anisotropic composite plates by the Finite Element Method. *Composite Structures*, 15:185–213, 1990.

[63] D.P. Makhecha, M. Ganapathi, and B.P. Patel. Vibration and damping analysis of laminated/sandwich composite plates using higher-order theory. *Journal of Reinforced Plastics and Composites*, 21(6):559–575, 2002.

[64] L. Demasi. Refined multilayered plate elements based on Murakami zig–zag functions. *Composite Structures*, 70:308–316, 2005.

[65] F. Auricchio and E. Sacco. Refined First-Order Shear Deformation Theory Models for Composite Laminates. *Journal of Applied Mechanics*, 70(3):381–390, 2003.

[66] E. Carrera. On the use of the Murakami's zig-zag function in the modeling of layered plates and shells. *Computers & Structures*, 82:541–554, 2004.

[67] A. Pagani, E. Carrera, M. Boscolo, and J.R. Banerjee. Refined dynamic stiffness elements applied to free vibration analysis of generally laminated composite beams with arbitrary boundary conditions. *Composite Structures*, 110:305–316, 2014.

[68] J.G. Ren. A new theory of laminated plate. *Composites Science and Technology*, 26:225–239, 1986.

[69] J.G. Ren. Bending theory of laminated plate. *Composites Science and Technology*, 27:225–248, 1986.

[70] M. Di Sciuva. A refined transverse shear deformation theory for multilayered anisotropic plates. *Atti Accademia delle Scienze di Torino*, 118:279–295, 1984.

[71] R.C. Averill. Static and dynamic response of moderately thick laminated beams with damage. *Composites Engineering*, 4(4):381–395, 1994.

[72] A. Tessler, M. Di Sciuva, and M. Gherlone. Refinement of Timoshenko Beam Theory for Composite and Sandwich Beams using Zigzag Kinematics. Technical report, NASA, Langley Research Center, 2007.

[73] A. Tessler, M. Di Sciuva, and M. Gherlone. A consistent refinement of first-order shear deformation theory for laminated composite and sandwich plates using improved zigzag kinematics. *Journal of Mechanics of Materials and Structures*, 5(2):341–367, 2010.

[74] R.D. Cook. *Finite Element Modeling For Stress Analysis*. John Wiley & Sons, 1995.

[75] E. Oñate. *Structural Analysis With the Finite Element Method - Linear Statics Vol.1*. Springer, 2009.

[76] *MSC Nastran 2014 – Linear Static Analysis User's Guide*.

[77] Variational Formulation of Bar Element – Lecture Notes. Technical report, Colorado College of Engineering and Applied Science.

[78] R.D. Cook, D.S. Malkus, M.E. Plesha, and R.J. Witt. *Concept and Applications of Finite Element Analysis*. John Wiley & Sons, 4th edition, 2002.

[79] S.K. Nandi and B. Sudeep. Effect of Mass Matrix Formulation Schemes on Dynamics of Structures. Technical report, Tata Consultancy Service.

[80] Mass Matrix Construction Overview – Lecture Notes. Technical report, Colorado College of Engineering and Applied Science.

[81] Standard Mass Matrices for Plane Beam Elements– Lecture Notes. Technical report, Colorado College of Engineering and Applied Science.

[82] Mass Matrix Diagonalization – Lecture Notes. Technical report, Colorado College of Engineering and Applied Science.

[83] K. Kim. A review of mass matrices for eigenproblems. *Computers & structures*, 46(6):1040–1048, 1993.

[84] Mass Templates for Plane Beam Elements– Lecture Notes. Technical report, Colorado College of Engineering and Applied Science.

[85] V.R. Aitharaju and R.C. Averill. C^0 zig-zag finite element for analysis of laminated composite beams. *Journal of Engineering Mechanics*, 125(3):323–330, 1999.

[86] R.C. Averill and Y.C. Yip. Development of simple, robust finite elements based on refined theories for thick laminated beams. *Computers & structures*, 59(3):529–546, 1996.

[87] M.N. Alam, N.K. Upadhyay, P.K. Talla, A. Fomethe, M. Fogue, A. Foudjet, G.N. Bawe, R. Ravichandaran, G. Thanigaiyarasu, S.R. Reddy, et al. Finite element analysis of laminated composite beams for zigzag theory using matlab. *International Journal of Mechanics and Solids (IJM&S)*, 5(1), 2010.

[88] P. Vidal and O. Polit. A sine finite element using a zig-zag function for the analysis of laminated composite beams. *Composites Part B: Engineering*, 42:1671–1682, 2011.

[89] M. Gherlone, A. Tessler, and M. Di Sciuva. C^0 beam elements based on the Refined Zigzag Theory for multilayered composite and sandwich laminates. *Composite Structures*, 93:2882–2894, 2011.

[90] A. Tessler, M. Di Sciuva, and M. Gherlone. A Refined Zigzag Beam Theory for Composite and Sandwich Beams. *Journal of Composite Materials*, 43(9):1051–1081, 2009.

[91] E. Oñate, A. Eijo, and S. Oller. Two-noded beam element for composite and sandwich beams using timoshenko theory and refined zigzag kinematics. *Publication CIMNE No-346*, 2010.

[92] E. Oñate, A. Eijo, and S. Oller. Simple and accurate two-noded beam element for composite laminated beams using a refined zigzag theory. *Computer Methods in Applied Mechanics and Engineering*, 213:362–382, 2012.

[93] A.J.M. Ferreira. *MATLAB Codes for Finite Element Analysis*. Springer, 2009.

[94] E. Oñate. *Structural Analysis with the Finite Element Method - Linear Statics Vol. 2*. Springer, 2013.

[95] G. Dhatt, G. Touzot, and E. Lefrançois. *Méthode des éléments finis*. Lavoisier, 2005.

[96] A.A. Khdeir and J.N. Reddy. An exact solution for the bending of thin and thick cross-ply laminated beams. *Composite Structures*, 37:195–203, 1997.

[97] Y.M. Ghugal and S.B. Shinde. Flexural analysis of cross-ply laminated beams using layerwise trigonometric shear deformation theory. *Latin American Journal of Solids and Structures*, 10:675–705, 2013.

[98] M. Gherlone. On the use of zigzag functions in equivalent single layer theories for laminated composite and sandwich beams: a comparative study and some observations on external weak layers. *Journal of Applied Mechanics*, 80:061004, 2013.

[99] J.H. Ginsberg. *Mechanical and structural vibrations - Theory and applications*. John Wiley & sons, 2001.

[100] M. Petyt. *Introduction to finite element vibration analysis*. Cambridge University Press, 1990.

[101] W. Heylen, S. Lammens, and P. Sas. *Modal Analysis Theory and testing*. Heverlee: KUL. Faculty of engineering. Department of mechanical engineering. Division of production engineering, machine design and automation, 1997.

[102] S. Adhikari. *Damping Models for Structural Vibration*. Phd dissertation, Cambridge University, Trinity College, 2000.

[103] J. Woodhouse. Linear damping models for structural vibration. *Journal of Sound and Vibration*, 215(3):547–569, 1998.

[104] B. Benchekchou, M. Coni, H.V.C. Howarth, and R.G. White. Some aspects of vibration damping improvement in composite materials. *Composites Part B: Engineering*, 29B:809–817, 1998.

[105] R. Chandra, S.P. Singh, and K. Gupta. Damping studies in fiber-reinforced composites – a review. *Composite Structures*, 46:41–51, 1999.

[106] I.C. Finegan and R.F. Gibson. Recent research on enhancement of damping in polymer composites. *Composite Structures*, 44:89–98, 1999.

[107] A. Treviso, B Van Genechten, D. Mundo, and M. Tournour. Damping in Composite Materials: Properties and Models. *Composites Part B: Engineering*, 78:144–152, 2015.

[108] D.D.L. Chung. Structural composite materials tailored for damping. *Journal of Alloys and Compounds*, 355:216–223, 2003.

[109] R.G. Ni and R.D. Adams. A rational method for obtaining the dynamic mechanical properties of laminae for predicting the stiffness and damping of laminated plates and beams. *Composites*, 15(3):193–199, 1984.

[110] D.X. Lin, R.G. Ni, and R.D. Adams. Prediction and measurement of the vibrational damping parameters of carbon and glass fibre-reinforced plastics plates. *Journal of Composite Materials*, 18:132–152, 1984.

[111] A.S. Hadi and J.N. Ashton. Measurement and theoretical modelling of the damping properties of a uni-directional glass/epoxy composite. *Composite Structures*, 34:381–385, 1996.

[112] G.C. Wright. The dynamic properties of glass and carbon fibre reinforced plastic beams. *Journal of Sound and Vibration*, 21(2):205–212, 1972.

[113] R.M. Crane and J.W. Gillespie. Characterization of the vibration damping loss factor of glass and graphite fiber composites. *Composites Science and Technology*, 40:355–375, January 1991.

[114] J.-M. Berthelot and Y. Sefrani. Damping analysis of unidirectional glass and Kevlar fibre composites. *Composites Science and Technology*, 64(9):1261–1278, 2004.

[115] J. Vantomme. A parametric study of material damping in fibre-reinforced plastics. *Composites*, 26:147–153, 1995.

[116] M.R. Maheri and R.D. Adams. Modal Vibration Damping of Anisotropic FRP Laminates Using the Rayleigh–Ritz Energy Minimization Scheme. *Journal of Sound and Vibration*, 259(1):17–29, 2003.

[117] D.J. Nelson and J.W. Hancock. Interfacial slip and damping in fibre reinforced composites. *Journal of Materials Science*, 13:2429–2440, 1978.

[118] A. Vazquez, M. Ambrustolo, S.M. Moschiar, M.M. Reboredo, and J.F. Gerard. Interphase modification in unidirectional glass-fiber epoxy composites. *Composites Science and Technology*, 58:549–558, 1998.

[119] S.K. Chaturvedi and G.Y. Tzeng. Micromechanical modeling of material damping in discontinuous fiber three-phase polymer composites. *Composites Engineering*, 1(1):49–60, 1991.

[120] C. Remillat. Damping mechanism of polymers filled with elastic particles. *Mechanics of Materials*, 39:525–537, 2007.

[121] S.J. Hwang and R.F. Gibson. Prediction of fiber-matrix interphase effects on damping of composites using a micromechanical strain energy/finite element approach. *Composites Engineering*, 3(10):975–984, 1993.

[122] J.H. Yim and J.W. Gillespie. Damping characteristics of 0 and 90 AS4/3501-6 unidirectional laminates including the transverse shear effect. *Composite Structures*, 50:217–225, 2000.

[123] J.-L. Tsai and Y.-K. Chi. Effect of fiber array on damping behaviors of fiber composites. *Composites Part B: Engineering*, 39:1196–1204, 2008.

[124] X. Lei, W. Rui, Z. Shujie, and L. Yong. Vibration characteristics of glass fabric/epoxy composites with different woven structures. *Journal of Composite Materials*, 45(10):1069–1076, 2010.

[125] I. Mishra and S.K. Sahu. An Experimental Approach to Free Vibration Response of Woven Fiber Composite Plates under Free-Free Boundary Condition. *International Journal of Advanced Technology in Civil Engineering*, 1(2):67–72, 2012.

[126] R.D. Adams and D.G.C. Bacon. Effect of fibre orientation and laminate geometry on the dynamic properties of CFRP. *Journal of Composite Materials*, 7(4):402–428, 1973.

[127] R.D. Adams and M.R. Maheri. Dynamic flexural properties of anisotropic fibrous composite beams. *Composites Science and Technology*, 50(4):497–514, January 1994.

[128] R.D. Adams and M.R. Maheri. Damping in advanced polymer–matrix composites. *Journal of Alloys and Compounds*, 355:126–130, 2003.

[129] S.J. Hwang and R.F. Gibson. The effects of three-dimensional states of stress on damping of laminated composites. *Composites Science and Technology*, 41:379–393, 1991.

[130] S.J. Hwang and R.F. Gibson. Contribution of interlaminar stresses to damping in thick laminated composites under uniaxial extension. *Composite Structures*, 20:29–35, 1992.

[131] M.R. Maheri. The effect of layup and boundary conditions on the modal damping of FRP composite panels. *Journal of Composite Materials*, 45(13):1411–1422, 2011.

[132] Y. Sefrani and J.-M. Berthelot. Temperature effect on the damping properties of unidirectional glass fibre composites. *Composites Part B: Engineering*, 37:346–355, 2006.

[133] S.M. Beane, M.M. Marchi, and D.S. Snyder. Utilizing optimized panel damping treatments to improve powertrain induced NVH and sound quality. *Applied Acoustics*, 45:181–187, 1995.

[134] D. Ray, N.R. Bose, A.K. Mohanty, and M. Misra. Modification of the dynamic damping behaviour of jute/vinylester composites with latex interlayer. *Composites Part B: Engineering*, 38:380–385, 2007.

[135] A.L. Araújo, P. Martins, C.M. Mota Soares, C.A. Mota Soares, and J. Herskovits. Damping optimization of viscoelastic laminated sandwich composite structures. *Structural and Multidisciplinary Optimization*, 39(6):569–579, 2009.

[136] E.E. Ungar. Loss factors of viscoelastically damped beam structures. *The Journal of the Acoustical Society of America*, 34(8):1082–1089, 1962.

[137] E.M.Jr. Kerwin. Damping of flexural waves by a constrained viscoelastic layer. *The Journal of the Acoustical society of America*, 31(7):952–962, 1959.

[138] D.J. Mead and S. Markus. Loss factors and resonant frequencies of encastre damped sandwich structures. *Journal of Sound and Vibration*, 12(1):99–112, 1970.

[139] D.J. Mead and S. Markus. The forced vibration of a three-layer, damped sandwich beam with arbitrary boundary conditions. *Journal of Sound and Vibration*, 10(2):163–175, 1969.

[140] J.-M. Berthelot. Damping Analysis of Orthotropic Composites with Interleaved Viscoelastic Layers: Modeling. *Journal of Composite Materials*, 40(21):1889–1909, 2006.

[141] J.-M. Berthelot and Y. Sefrani. Damping Analysis of Unidirectional Glass Fiber Composites with Interleaved Viscoelastic Layers: Experimental Investigation and Discussion. *Journal of Composite Materials*, 40(21):1911–1932, 2006.

[142] E.R. Fotsing, M. Sola, A. Ross, and E. Ruiz. Lightweight damping of composite sandwich beams: Experimental analysis. *Journal of Composite Materials*, 47(12):1501–1511, 2012.

[143] Damping in composites: it's there but is it understood? Technical report, Colorado College of Engineering and Applied Science.

[144] M.D. Rao. Recent applications of viscoelastic damping for noise control in automobiles and commercial airplanes. *Journal of Sound and Vibration*, 262:457–474, 2003.

[145] Z. Li and X. Liang. Vibro-acoustic analysis and optimization of damping structure with Response Surface Method. *Materials & Design*, 28:1999–2007, 2007.

[146] E.J. Barbero. *Finite Element Analysis of Composite Materials*. CRC Press, 2008.

[147] T. Pritz. Five-parameter fractional derivative model for polymeric damping materials. *Journal of Sound and Vibration*, 265:935–952, 2003.

[148] S.H. Crandall. The role of damping in vibration theory. *Journal of Sound and Vibration*, 11(1):3–18, 1970.

[149] S.H. Crandall. The hysteretic damping model in vibration theory. *Proceedings of the Institution of Mechanical Engineers, Part C: Journal of Mechanical Engineering Science*, 205:22–28, 1991.

[150] E.E. Ungar and E.M.Jr. Kerwin. Loss factors of viscoelastic systems in terms of energy concepts. *The Journal of the Acoustical Society of America*, 34(7):954–957, 1962.

[151] D.A. Saravanos and C.C. Chamis. Unified Micromechanics of Damping for Unidirectional Fiber Reinforced Composites. *NASA Technical Memorandum*, pages 1–26, 1989.

[152] C.D. Johnson, D.A. Kienholz, and L.C. Rogers. Finite element prediction of damping in structures with constrained viscoelastic layers. *AIAA Journal*, 20(9):71–81, 1982.

[153] M. Enelund and P. Olsson. Damping described by fading memory—analysis and application to fractional derivative models. *International Journal of Solids and Structures*, 36:939–970, 1999.

[154] Y. Wang and D.J. Inman. Finite element analysis and experimental study on dynamic properties of a composite beam with viscoelastic damping. *Journal of Sound and Vibration*, 332:6177–6191, 2013.

[155] G.A. Lesieutre. Finite elements for dynamic modeling of uniaxial rods with frequency-dependent material properties. *International Journal of Solids and Structures*, 29(12):1567–1579, 1992.

[156] E. Carrera, M. Filippi, and E. Zappino. Free vibration analysis of laminated beam by polynomial, trigonometric, exponential and zigz-zag theories. *Journal of Composite Materials*, 48:2299–2316, 2014.

[157] A. Treviso, D. Mundo, and M. Tournour. A C^0-continuous RZT beam element for the damped response of laminated structures. *Composite Structures*, 131:987–994, 2015.

[158] J.-M. Berthelot and Y. Sefrani. Longitudinal and transverse damping of unidirectional fibre composites. *Composite Structures*, 79(3):423–431, 2007.

[159] R. Pirk, L. Rouleau, V. D'Ortona, W. Desmet, and B. Pluymers. Modeling viscoelastic damping insertion in lightweigth structures with generalised maxwell and fractional derivative models. *26th International Conference on Noise and Vibration Engineering, Leuven*, 2014.

[160] *Samcef User manual*.

[161] D. Versino, M. Gherlone, M. Mattone, M. Di Sciuva, and A. Tessler. C^0 triangular elements based on the Refined Zigzag Theory for multilayer composite and sandwich plates. *Composites Part B: Engineering*, 44:218–230, 2013.

[162] A. Barut, E. Madenci, and A. Tessler. C^0-continuous triangular plate element for laminated composite and sandwich plates using the {2,2} – Refined Zigzag Theory. *Composite Structures*, 106:835–853, 2013.

[163] L. Iurlaro, M. Gherlone, M. Di Sciuva, and A. Tessler. Assessment of the Refined Zigzag Theory for bending, vibration, and buckling of sandwich plates: a comparative study of different theories. *Composite Structures*, 106:777–792, 2013.

[164] A. Eijo, E. Oñate, and S. Oller. A four-noded quadrilateral element for composite laminated plates/shells using the refined zigzag theory. *International Journal for Numerical Methods in Engineering*, 95:631–660, 2013.

[165] A. Kumar, A. Chakrabarti, and P. Bhargava. Accurate dynamic response of laminated composites and sandwich shells using higher order zigzag theory. *Thin-Walled Structures*, 77:174–186, 2014.

[166] G.S.T. Armer. *Monitoring and Assessment of Structures*. CRC Press, 2001.

[167] D.J. Ewins. Model validation: Correlation for updating. *Sadhana*, 25:221–234, 2000.

[168] Advanced Composites Materials and Their Manufacture – Technology Assessment. Technical report, US Energy Department.

[169] P. Boisse, editor. *Advances in Composites Manufacturing and Process Design*. Elsevier Science, 2015.

[170] A.K. Kaw. *Mechanics of Composite Materials, Second Edition*. CRC Press, 2005.

[171] T. Ishikawa and T.W. Chou. Stiffness and strength behaviour of woven fabric composites. *Journal of Materials Science*, pages 3211–3220, 1982.

[172] T. Ishikawa and T.W. Chou. One-dimensional micromechanical analysis of woven fabric composites. *AIAA Journal*, 21(12):1714–1721, 1983.

[173] M.J. King, P. Jearanaisilawong, and S. Socrate. A continuum constitutive model for the mechanical behavior of woven fabrics. *International Journal of Solids and Structures*, 42:3867–3896, June 2005.

[174] J.M. Berthelot. *Matériaux composites: comportement mécanique et analyse des structures*. Tec & Doc, 1999.

[175] *NX 10.0 – Advanced Simulation User's Guide*.

[176] *NX Nastran 10.0 – User's Guide*.

[177] A. Cherouat and H. Borouchaki. Present State of the Art of Composite Fabric Forming: Geometrical and Mechanical Approaches. *Materials*, 2:1835–1857, 2009.

[178] A. Cherouat and H. Bourouchaki. Numerical Tools for Composite Woven Fabric Preforming. *Advances in Materials Science and Engineering*, 2013:1–18, 2013.

[179] A. Cherouat, H. Borouchaki, and L. Giraud-Moreau. Mechanical and geometrical approaches applied to composite fabric forming. *International Journal of Material Forming*, 3:1189–1204, 2010.

[180] P. Boisse, N. Hamila, F. Helenon, B. Hagege, and J. Cao. Different approaches for woven composite reinforcement forming simulation. *International Journal of Material Forming*, 1:21–29, 2008.

[181] N. Hamila and P. Boisse. A Meso–Macro Three Node Finite Element for Draping of Textile Composite Preforms. *Applied Composite Materials*, 14:235–250, 2007.

[182] N. Hamila, F. Hélénon, P. Boisse, and S. Chatel. Simulation of mono-ply and multi-ply woven composite reinforcements forming. *European Journal of Computational Mechanics/Revue Européenne de Mécanique Numérique*, 17(5-7):919–931, 2008.

[183] K. Vanclooster, S.V. Lomov, and I. Verpoest. Simulating and validating the draping of woven fiber reinforced polymers. *International Journal of Material Forming*, 1:961–964, 2008.

[184] H. Borouchaki and A. Cherouat. Drapage géométrique des composites. *Comptes Rendus Mecanique*, 331:437–442, 2003.

[185] A. Treviso, B Van Genechten, D Mundo, and M Tournour. NVH assessment of polymer-based composite structures. In *26th International Conference on Noise and Vibration Engineering (ISMA)*, Leuven.

[186] Composite materials handbook - Volume 2. Polymer Matrix Composites Materials Properties. SAE International, 2012.

Publications

Conference papers

A. Treviso, B. Van Genechten, D. Mundo. *CAE-based assessment of manufacturing process impact on NVH performance of composite structures.* 22nd International Conference on Composite and Nano-Engineering, Malta July 2014.

A. Treviso, B. Van Genechten, D. Mundo. *NVH assessment of polymer-based composite structures.* 26th International Conference on Noise and Vibration Engineering, Leuven September 2014.

A. Treviso, D. Mundo, M. Tournour. *A C^0-continuous RZT beam element for the damped response of laminated structures.* 18th International Conference on Composite Structures, Lisbon June 2015.

A. Treviso, D. Mundo, M. Tournour. *Dynamic response of laminated structures using a Refined Zigzag Theory (RZT) shell element.* International Conference on Engineering Vibration, Ljubljana September 2015.

Journal papers

A. Treviso. B. Van Genechten, D. Mundo, M. Tournour. *Damping in composite materials: Properties and models.* Composites Part B: Engineering, Vol. 78 (2015), pp: 144-152.

A. Treviso, D. Mundo, M. Tournour. *A C^0-continuous RZT beam element for the damped response of laminated structures.* Composite Structures, Vol. 131 (2015), pp: 987-994.

Those who travel with the current
will always feel they are good swimmers;
those who swim against the current may never realize
they are better swimmers than they imagine.
Shankar Vedantam.